The manufacture and investigation of abrasion resistant Fe–V–C alloys

By Anthony Henri Fleischmann

Dissertation submitted to the faculty of Engineering, University if the Witwatersrand, Johannesburg, in fulfilment of the requirements for the degree of Master of Science in Engineering.

Johannesburg, 1995

Declaration

I declare that this dissertation is my own unaided work. It is being submitted for the degree of Master of Science in Engineering in the University of the Witwatersrand, Johannesburg. It has not been submitted before for any degree or examination at any other university.

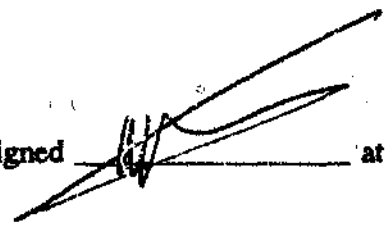

Signed _____ at Johannesburg on the 27th day of January 1995

Anthony Henri Fleischmann

Abstract

This dissertation deals with alloys containing between 0.2 and 9.5wt% carbon and between 3.2 and 64.3wt% vanadium with the balance iron. Alloys were produced by induction melting and followed by remelting in vacuum tungsten arc furnaces. No heat–treatment was performed, as the aim was to identify useful alloys that may be applied by hardfacing techniques in the field. The requirement of post weld heat–treatment would greatly limit the use of hardfacing alloys. The experimental techniques aimed at characterising the alloys included X–ray diffraction analyses, Mössbauer Spectroscopy, optical, scanning and transmission electron microscopy and chemical analyses while density measurements, hardness tests and 2 and 3–body abrasion tests gave the material properties.

During experimentation, problems with existing 3–body abrasive wear testing apparatus, were identified. The testing apparatus used in these experiments was redesigned to reduce the uncertainty in determining wear rates. Caution regarding similar wear testing apparatus is highlighted.

Under the experimental conditions used, alloys containing large primary, spheroidal VC particles in a matrix of ferrite and cementite gave maximum abrasion resistance. The abrasion resistance of the alloys compared well with commercially available hardfacings based on WC, Cr_2C_3 and mixed carbides with one alloy outperforming all these. This superior performance occurred despite a cracked, heterogeneous microstructure. Future alloys with small additions to strengthen the matrix should yield highly competitive materials.

Acknowledgements

All my thanks to my two supervisors Professor S.B. Luyckx and Professor A. Koursaris for giving me the opportunity to explore. Their encouragement and dedicated support have allowed this project to be completed and my knowledge to expand.

My thanks also to :

1) Mintek for financial support, use of equipment and technical help. Special thanks to Dr P T Wedepohl, Mr Maurice Winch and Mr John Maskrey.
2) CSIR for using their wear testing equipment. Special thanks to Mr Oliver Damm and staff.
3) WASA for supplying commercial hardfacing alloys for comparative wear testing. Special thanks to Mr Richard Gibbs.
4) Highveld Steel and Vanadium for additional donations of ferro vanadium. Special thanks to Mr Andrew Dickman.
5) FRD for financial support.
6) Dr H. Pollak of the Physics department at the University of the Witwatersrand for help and collaboration on Mössbauer Spectroscopy.
7) Dr Mike Witcomb, Mr Stan Terras and staff of the Electron Microscope Unit for their time and effort in helping me on the SEM and TEM.
8) Dorbyl Group for the time allowed from my bursary commitments to continue this work.
9) Mr John Morfitt for his endless patience on new designs and the use of his workshop and equipment.

Index

1. INTRODUCTION

Including the former USSR and China, South Africa had 47% (5400000ton of vanadium metal) of the estimated world reserves in 1985. Exports of vanadium in 1983 amounted to 13162 tons[1,2] or 49.0% of the world supply. There is potential to increase exports or substitute current imports to South Africa by finding new uses for vanadium.

This work investigated the potential of the iron–vanadium–carbon (Fe–V–C) alloys for hardfacing applications. The Fe–V–C alloy system has potential for hardfacings for the following reasons:

1) Most alloys used to resist highly abrasive environments contain hard carbides (mainly Cr_2C_3 and WC).

2) Hardfacings containing VC have already entered the market. These are combinations of VC and WC with other additions such as copper, manganese and cobalt[3–6].

3) The Japanese have investigated some properties of VC containing alloys in abrasion resistant applications and reported promising results[7,8].

In spite of the potential of these alloys, a survey of the literature showed that the Fe–V–C alloy system had not been investigated in detail. Therefore, the present work aimed at filling some of the gaps by producing Fe–V–C alloys covering all the phases appearing on the Fe–V–C equilibrium diagram[9]. The focus was kept on abrasion resistance because of the applications of hardfacings.

2. LITERATURE SURVEY

This concise literature survey outlines the background to hardfacings, the reasons for their use, the properties of VC and the work done previously on the Fe–V–C system.

2.1. Hardfacings and the reasons for their effectiveness

It was reported that abrasion accounts for about 50% of wear encountered in industry[10]. The National Research Council of Canada reported in 1984 that abrasive wear absorbed between 0.5 – 1.0% of the gross national product of industrialised nations[11]. This gives some idea of the magnitude of the problem and the reason for the need to devise ways to increase the life of components.

Why hardfacings are successful requires an understanding of the mechanisms of abrasive wear. The following is a brief overview to highlight the areas of abrasive wear under investigation. For greater detail the reader is referred to more thorough works on wear mechanisms[11-14].

Abrasive wear occurs when a rough hard surface slides on a softer surface and ploughs a series of grooves. There are two general situations for this type of wear. In 2–body abrasion one surface is the harder of the two. In 3–body abrasion the hard surface belongs to a third body, generally a small particle of grit or abrasive, caught between the two moving surfaces[15]. The latter are more prevalent in the applications in which hardfacing alloys are employed.

The hard surface asperities or particles press into the softer surface causing plastic flow. With a tangential motion superimposed, the harder surface removes the softer material by combined effects of 'micro–ploughing', 'micro–cutting' and 'micro–cracking'[12]. For a marked improvement in wear resistance, the ratio of the hardness of the surface to the hardness of the abrasive must exceed 0.5[13]. It is unnecessary to increase the hardness of the material beyond 1.3 times the abrasive hardness as no further significant improvement will be obtained. By increasing the hardness of the wear resistant surface the first phase of abrasion ie the

penetration of the hard surface asperities or particles into the surface, can be reduced or eliminated. With the asperities or abrasive particles unable to penetrate into the surface, the removal process is halted or greatly slowed down.

Common abrasives such as quartz (hardness of 900 – 1280Hv[13]) would require alloys with bulk hardness in the region of 1660Hv (using the 1.3 ratio mentioned above). Alloys of this hardness would be both costly and difficult to manufacture in any single phase alloy system. The resultant alloys would be highly susceptible to fracture[11] as alloy hardness is generally inversely related to toughness[16]. Often abrasive conditions occur simultaneously with impact conditions.

Multiphase alloy are a combination of a hard phase in a tough matrix and attain both abrasive wear resistance, impact resistance are easy to manufacture. Many alloys of this type have been developed[1,7,14,17-22]. The major groups rely on a carbide hard phase in a cementing matrix. The carbides most often present are those of Cr and W with V and Ti increasingly being reported as alloy additions[23].

The effectiveness of hard phases depends on their size, hardness, volume fraction and uniformity of distribution. The precipitation of primary stoichiometric carbides is beneficial. The effectiveness of the hard phase is also dependent on the hardness of the metal matrix. The hardness of the hard phase depends on the alloying elements. Its distribution depends on precipitation temperature, solidification sequence[21] and physical properties compared to the matrix[6]. Abrasive wear resistance in Fe based alloys is reported to increase with a change in the matrix from ferrite and cementite to ferrite and pearlite to martensite[21]

Abrasion resistant alloys are applied to working surfaces to prevent high wear rates and repair components that have undergone material loss. These are applied to components by one of several techniques, including plasma spraying, electrolytic plating and electric and gas welding[16]. The welding technique is often called hardfacing.

According to Farmer[24] many thousands of different hardfacing alloys have been developed over the past 50 years. These may be divided into five categories depending on service

conditions. Two of these categories include, highly alloyed materials for high abrasive conditions and W–C alloys for extreme abrasion resistance. The former group consists of high–carbon, high–chromium alloys, Stoodites® and high chromium cast irons etc. based largely on Cr–C alloys while the latter are made up of the group of alloys identified as Borium®, Tungrod®, Tungsmooth® etc. and are based on W–C alloys. The (W,V)C containing alloys Ucar® and Vancar®, mentioned later [4,25] fall into the latter category. The principle difference between these two categories is the hardness of the hard phase, namely the carbide.

The welding technique is a major application route for the two groups of alloys mentioned above and the technique can be simulated in a laboratory using a tungsten arc furnace. Tungsten arc furnaces simulate the high heating and cooling rates experienced during welding[7]. In the furnace an electric discharge between the tungsten electrode melts the material, which is cooled from below by the water cooled base.

2.2. VC – containing hardfacing materials

Several hardfacing materials have been developed commercially in which VC has been added to WC. The VC is added to overcome the problems experienced with pure WC hardfacing alloys. Pure WC is heterogeneously distributed in the molten metal substrate and results in heterogeneous hardness and wear rates. This results from inherent differences in physical properties (especially the densities of the carbide and substrate) of the base metal and the WC[6]. VC has a density closer to that of liquid iron and therefore results in the mixed (W,V),C being homogeneously distributed in the alloys.

The formation of mixed (Fe,W)C which are either more brittle or softer than pure WC depending on composition, reduces the effectiveness of WC for abrasive wear protection[6]. It results in the addition of excessive amounts of WC to hardfacing alloys. The relatively high density of WC also means that relatively large amounts of WC are required for hardfacing applications[6] which increases the alloy costs further.

The above limitations are not experienced in the Fe–V–C system. The 500°C isotherm of the Fe–V–C alloy phase diagram (see **Section 3.1.**) shows that regions exist in which pure VC

will form. There are only small density differences between VC and liquid Fe resulting in evenly distributed VC in the Fe matrix. The lower density reduced the amount of VC required to obtain the same volume percentage as WC, resulting in a cheaper alloy. (Properties of the VC and WC are given in the next section)

The available alloys were based on WC technology to which VC was added as an alloying addition[3,4,5,6,25]. The alloys had other alloy additions such as free carbon, nickel and cobalt[3,4]. Alloys containing 44wt% (V,W)C are reported to have a wear resistance equivalent to alloys with 60wt% WC[25]. I.N. Slabodinskii et al[25] made a successful alloy using a combination of VC and Cr–C that was reported to work extremely well.

The Japanese studied the Fe–V–C alloy system in the region between 8 and 55% VC. The emphasis was however on the effects of heat treatment and cooling rate on the alloys and the effect this had on the 2–body abrasion resistance and fracture toughness of the alloys. Alloy additions to the system such as nickel, molybdenum, manganese and silicon, which alloyed the matrix, modified the results obtained[7,8].

This dissertation explored the Fe–V–C alloy system and its potential for 2 and 3–body abrasive wear resistance. The interrelationship between the various phases present was explored to see the effect on 2 and 3–body abrasive wear resistance.

2.3. Properties of VC

The densities of the various carbides are compared to liquid Fe in **Table 2.1.** This shows that the density of VC approaches that of liquid Fe. This results in the VC being evenly distributed in the liquid Fe and therefore evenly distributed in the final alloy.

The microhardness values reported in literature vary. The reason for this variation is most likely due to stoichiometric and crystallographic differences. Values given in **Table 2.2** are from several sources (Vickers and Knoop hardness) and give an idea of the ranking of some abrasives and phases. It should be noted that Silica (quartz) is more abrasive than its hardness would suggest as it breaks under load into extremely sharp particles that are more easily able

to penetrate alloy surfaces.

Table 2.1 Densities of various carbides and liquid Fe[25,26].

Material	Density (g/cm^3)
TiC	4.94–4.57
VC	5.65–5.61
NbC	7.79–7.72
TaC	15.22
Ucar® (V,W)C	7.0
WC	15.6
liquid Fe	7.0

Table 2.2. Various microhardness values reported[9,18,27]

Material or Phase	Microhardness
Pearlite	240 to 425 (Hv)
Cementite	840 to 1100 (Hv)
Quartz (Silica)	800 to 1000 (Hv)
Chromium Carbide	1300 to 1700 (Hv)
Corundum (Al_2O_3)	2000 (Knoop)
Tungsten Carbide	2350 to 2700 (Knoop)
Vanadium Carbide	2800 to 2810 (Knoop)

The anisotropy of the carbides is explained in work done by Rowcliffe et al[28] in which the hardness of $TiC_{0.80}$ and $VC_{0.84}$ was measured using Knoop hardness tests. A 100g load was used and the hardness measured at different angles from the [100] crystal plane (see Figure 2.1).

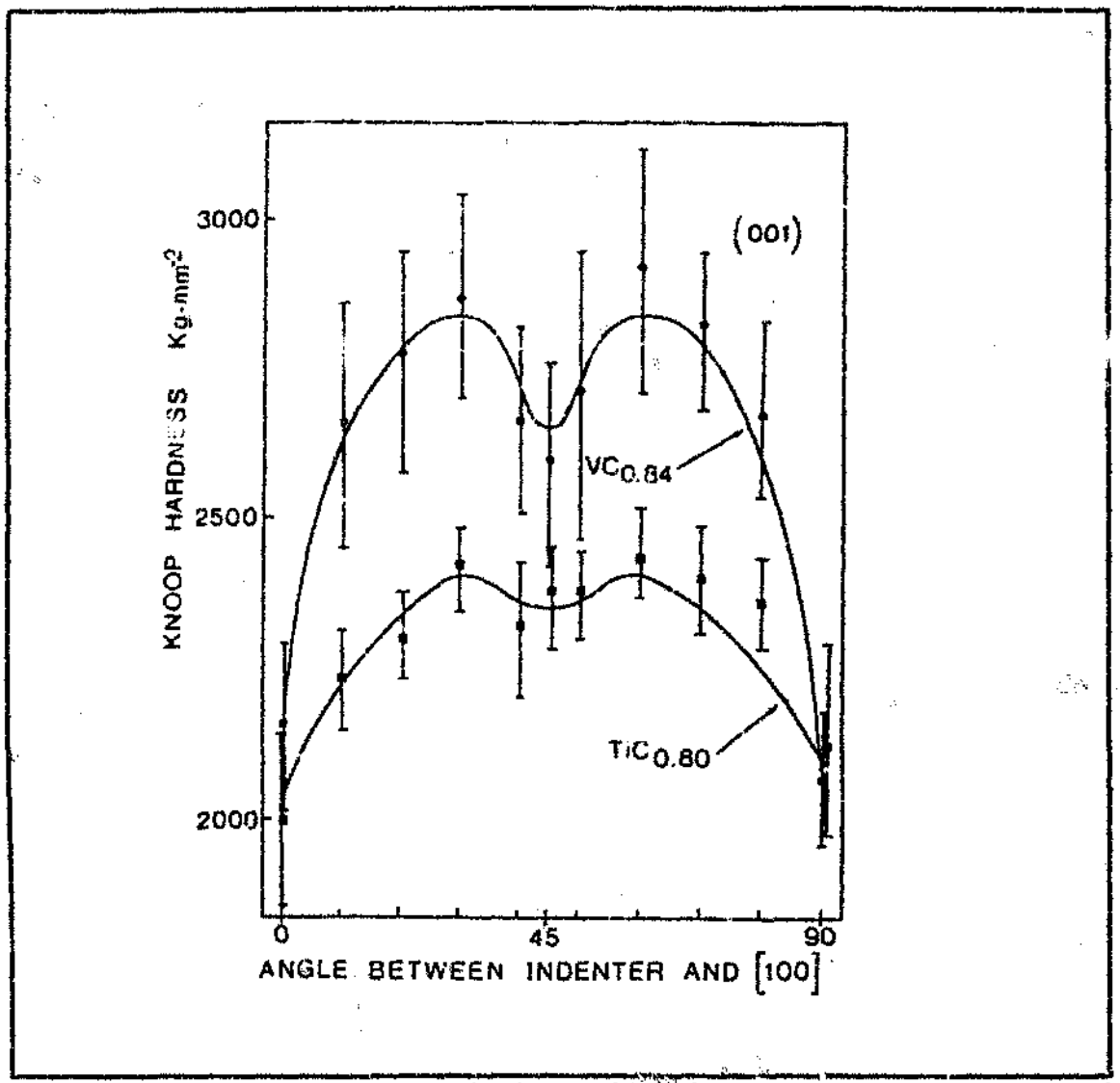

Figure 2.1. – Variation of Knoop hardness with indentor orientation for $TiC_{0.84}$ and $VC_{0.84}$[28].

The lattice parameters of various carbides are given in Table 2.5[28]. The solid solubility of Fe in the VC lattice is reported as 0.8 atom %[29] while elsewhere the maximum is reported as 1.9%[26].

The liquidus, 500°C and 1100°C equilibrium phase diagrams of the Fe–V–C alloys system were reported by Raghavan[9]. These are presented later in Sections 3 and 4.

Table 2.3. – Lattice parameters of some carbides[28].

Carbide	Lattice Parameter (Å)
TiC	4.332
ZrC	4.70
HfC	4.64
VC	4.16
NbC	4.47
TaC	4.45

2.4. The Fe–V–C system

Two Japanese papers detail work done on VC in Fe matrices. Cast and welded deposition techniques were used to control the VC particle size. Heat–treatment and alloy additions were used to control the matrix[7,8]. The alloys reported on in these two papers included additions of manganese, silicon, molybdenum and nickel to V, C and Fe. Abrasion tests were conducted using a 2–body abrasion test rig. When large abrasive particles were used for testing, the alloys with larger VC particles gave better results. Smaller VC particles resulted in lower wear rates for smaller abrasive size particles. The effect of the VC content was more notable in those alloys that had undergone annealing than those that had undergone quenching and tempering. Changes in wear rate were affected more by heat treatment in low hardness alloys than in high hardness alloys[7].

The two techniques of obtaining the alloys resulted in primary VC particles of differing size. Slower cooled cast alloys resulted in large VC particles (up to 100μm)[7]. These large particles were reported to reduce the fracture toughness of the alloys. The VC particle size exerted a greater influence on the fracture toughness than the amount of VC present. The fracture properties of the alloys containing smaller VC particles were thought to be governed by the hardness of the matrix rather than the VC particles size. It is reported that the VC particles

act as stress concentrators, the mechanism being crack initiation in VC particles (due to dislocation pileups etc.). A Stroh relationship, ie that the stress is proportional to the square root of the carbide particle size, is reported to hold[8].

Work done in China proved that higher toughness white cast iron, with MC type carbides, can be obtained with spheroidised carbide structures. The occurrence of impact loading in many abrasive wear applications requires any new abrasive wear resistant alloy to have high toughness. The Chinese alloys contained up to 10% VC. Spheroidal type VC particles were obtained by the addition of rare earth and nitrogen to melts. The mechanism reported by Chang et al[30] suggests that sulphur and phosphorus segregate on the cubic corners of the solidifying VC particles and promote dendritic growth. The addition of cesium, titanium and nitrogen acts to scavenge the sulphur and form heterogeneous nucleation sites. The Chinese paper also demonstrated that high cooling rates do not favour the growth of spheroidal VC particles[30].

3. EXPERIMENTAL PROCEDURES

3.1. Alloy charge make-up

The alloys described in this dissertation were prepared in 3 phases. Phase 1 alloys (VC2, VC3, VC4, VC5, VC6, VC7 and VC8) together with Phase 2 Alloy VF576 were prepared from VC powder, C and Fe. Imported or local VC powder, containing 17.6±0.12 wt% (nominally $VC_{0.91}$) or 12.8±0.25 wt% (nominally $VC_{0.62}$) C respectively, was added to Fe powder in amounts ranging from 10 to 20 wt% (**Table 3.1**). Additional C in the form of graphite was added when necessary. The imported VC powder was between 1 and 2μm in size. The local powder was coarser. The materials used to prepare the alloys and their nominal chemical compositions are summarised in **Table 3.1.** Their actual chemical compositions are given later.

VC powder particles dissolved in the molten Fe and then precipitated on cooling according to the phases seen on the 500°C isotherm of the Fe–V–C phase diagram shown in **Figure 3.1.** Further work in Phase 2 Alloys (VF577, VF578, VF579, VF607, VF608 AND VF609) and Phase 3 Alloys (681C, 681A, AF583C, AF583A, AF584C, AF584A, AF585C, AF585A, AF586A, AF587C, AF588C, AF588A, AF589C and AF589A) made use of FeV and commercial recarburising material, which were less expensive than imported VC powders. The only local producer of VC powder had ceased production. The larger sized FeV chunks were easier to melt due to fewer problems with bridging during melting. The recarburising material resulted in the C being taken into the liquid melt faster than the graphite which tended to float rather than dissolve. The use of these charge materials improved the recovery rate from the charge make up.

Chemical analysis detailed later showed that C was lost during melting. The amount lost in each case varied, making control of the final chemical composition difficult. After melting the inside of the furnace was covered with a layer of fine black powder.

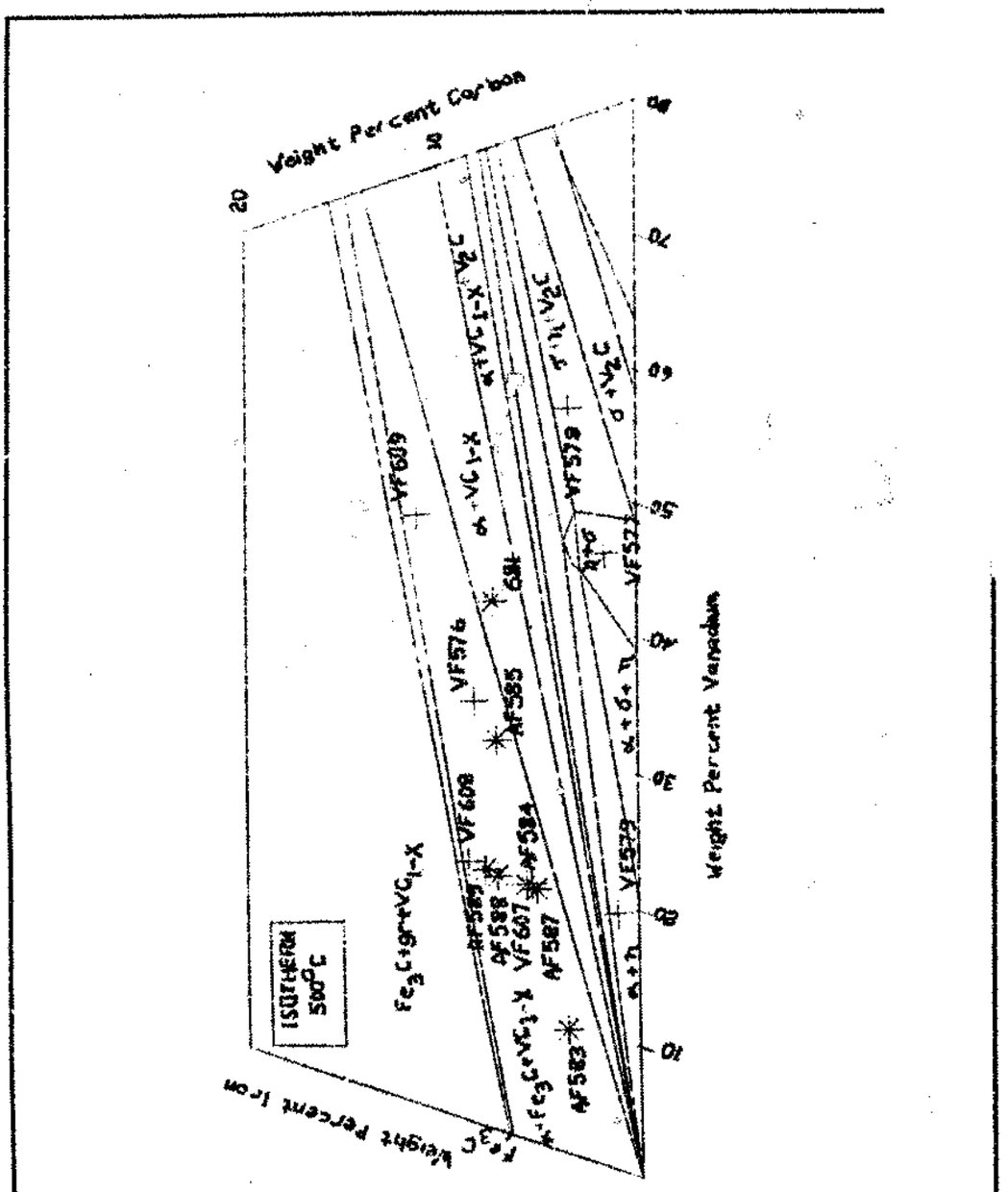

+ – Phase 2 alloys
*** – Phase 3 alloys**
Figure 3.1. – Nominal positions of Phase 2 and 3 alloys on the 500°C isotherm of the Fe–V–C phase diagram[9].

Table 3.1 – Phase of production, alloy name, nominal chemical composition and materials used.

Phase	Alloy	wt% C*	wt% V*	Materials used
1[ii]	VC2	1.8	8.2	Imported VC + Fe
1[ii]	VC5	1.9	8.2	Imported VC + Fe + C
1[ii]	VC3 VC4 VC7	1.3 1.3 2.6	8.7 8.7 17.4	Local VC + Fe
1[ii]	VC6	1.4	8.7	Local VC + Fe + C
1[ii]	VC8	3.8	17.4	Local VC + Fe + C
2[ii]	VF576	8.1	32.2	Local VC + Fe + C
2[ii]	VF577 VF578 VF579 VF607 VF608 VF609	1.3 3.0 0.6 5.0 8.4 10.9	46.7 57.2 20.1 20.0 20.0 45.0	FeV + Fe + C
3	681C AF583C AF584C AF585C AF587C AF588C AF589C	7.0 3.4 5.3 6.8 5.0 6.8 7.4	40.0 10.0 20.0 30.0 20.0 20.0 20.0	FeV + Fe + C
3	681A AF583A AF584A AF585A AF586A AF588A AF589A	7.0 3.4 5.3 6.8 3.2 6.8 7.4	40.0 10.0 20.0 30.0 42.5 20.0 20.0	FeV + Fe + C

C = as cast material A = button arc remelted material

(i) Balance is Fe. (ii) Button arc remelted material

The nominal composition of Phase 2 alloys ranged from 20.0 to 57.2 wt% V (**Table 3.1**) and from 0.6 to 10.9 wt% C with the balance Fe. These alloys were meant to contain all the Fe–V–C phases (ferrite, cementite, η_1, θ, VC_{1-X} and V_2C) found on the 500°C isotherm of the Fe–V–C phase diagram in this range of chemical compositions as indicated in **Figure 3.1.** Results obtained with Phase 2 alloys pointed to the area containing Fe_3C, VC_{1-X} and α as being the most promising for further investigation.

Phase 3 alloys looked at the region containing α, Fe_3C and VC_{1-X} in greater detail. Phase 3 alloys were used to investigate the effect on abrasive wear of varying amounts of primary VC in a pearlite matrix (see AF583A, AF583C, AF584A, AF584C, AF585A and AF585C) and the effect of changing the matrix while keeping the amount of VC constant (see AF584A, AF584C, AF588A, AF588C, AF589A and AF589C). Alloys 681C and 681A looked at primary VC in a α matrix for comparison with Alloy VF609. Alloys AF583A, AF583C, AF584A, AF584C, AF585A and AF585C had γ matrices at 1100°C. It was anticipated that future work would investigate alloy additions to increase the hardenability of the matrices. Jominy tests confirmed that the alloys were hardenable (see Alloy AF587C, **Section 4.9**) but that further alloy additions would be required to obtain martensitic matrices.

The Phase 3 alloys had a nominal chemical composition between 10 and 40 wt% V and 3.1 to 7.4 wt% C with the balance Fe. AF586A which contained 47.9 wt% V and 3.4 wt% C was made to test whether a tough matrix would improve the properties of the η phase alloys, and was made outside this chemical range. Tramp elements were present in the raw materials as expected. The sulphur, phosphor, aluminium and silicon content of the alloys were determined in subsequent chemical analysis.

3.2. Alloy manufacture

Phase 1 and 2 alloys where melted in a vacuum induction furnace which was evacuated to about 10^{-4} atm and then flushed with argon. The evacuation and flushing were repeated leaving the chamber filled with argon and a low partial pressure of oxygen. Melting took place in a magnesia crucible. A sooty deposit formed on the inside of the furnace and blocked the view through the furnace windows. This deposit made it difficult to control melting. It

gave rise to problems with temperature measurement using an optical pyrometer. On-line chemical analysis was not possible due to the vacuum chamber and no trimming additions could therefore be made. As previously mentioned this resulted in differences between the nominal and final chemical compositions.

Phase 1 and 2 alloys were produced in ingots of ±250g and were completely remelted in a vacuum button arc furnace. The furnace was evacuated to $\sim 10^{-4}$ atm and flushed with argon. This process was repeated leaving argon with a low partial pressure of oxygen in the chamber. Melting occurred in the plasma formed during the discharge between a hand manipulated tungsten electrode and a water cooled copper base. The copper base had a slot of 35x130x15mm which contained the molten material. The ingot experienced high heating and cooling rates with directional solidification, simulating welding conditions. The microstructure of some alloys showed columnar grains of ferrite in a eutectic matrix (**Figure 3.2**).

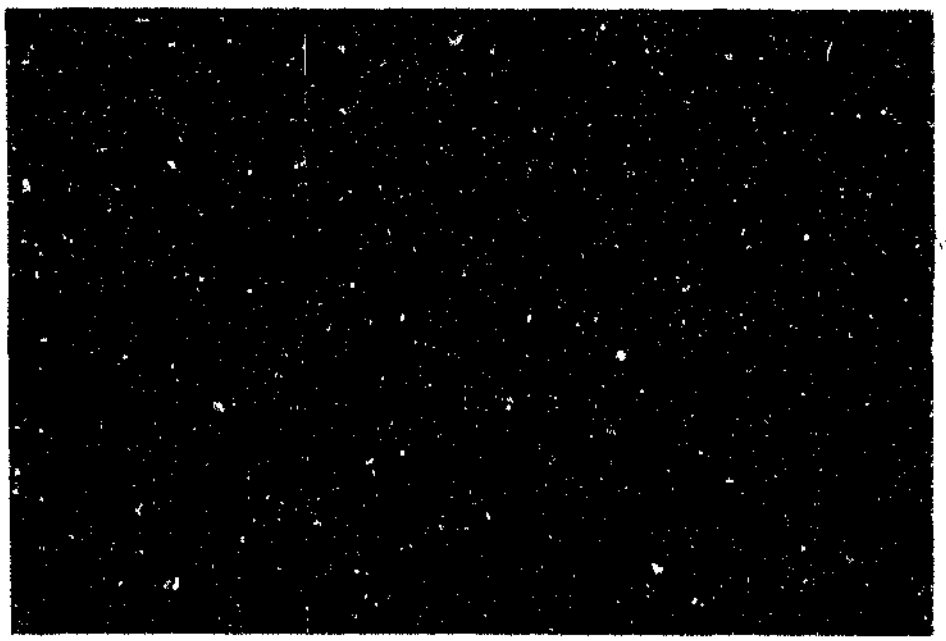

Figure 3.2. – Dendrites of ferrite in a eutectic matrix in Alloy VC7.
Etched, 2% Nital, followed by lead acetate (30seconds, 1.5V) 100x.

Phase 3 alloys were produced in an air induction furnace and poured into graphite moulds.

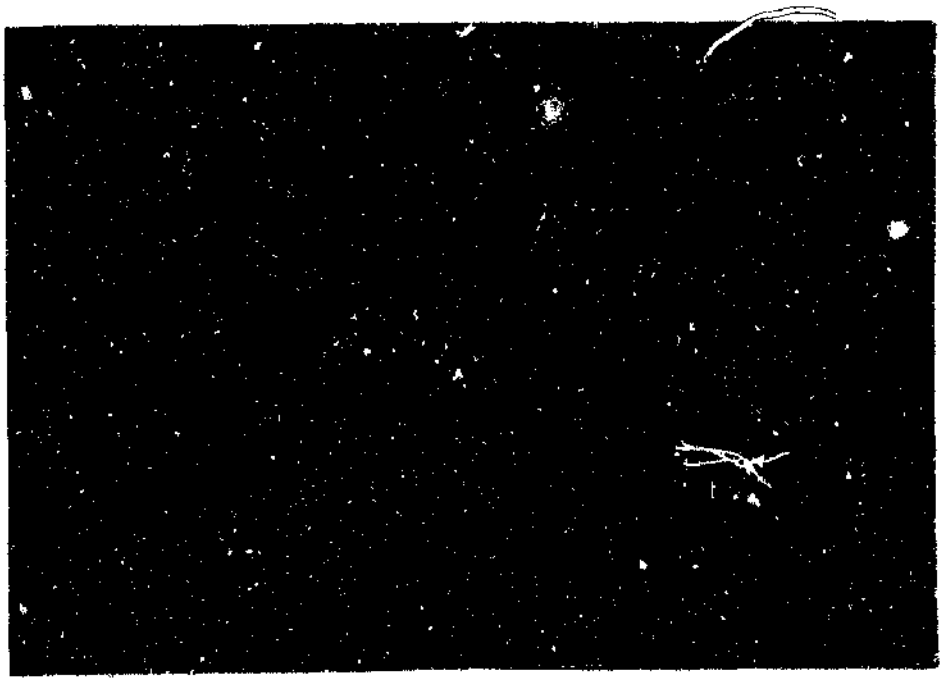

Figure 3.3 – Alloy VF609 shows heterogeneous microstructure.
Etched, lead acetate at 1.5V for 30 Seconds, 100x.

This allowed larger ingots of about 7kg to be manufactured. Magnesia crucible were again used to melt the alloys. The larger ingots were easier to melt by the induction melting technique and exhibited greater homogeneity due to longer holding times above the liquidus temperature. It was found that the 250g Phase 1 and 2 alloy ingots were extremely difficult to heat above the liquidus temperature. They tended either to boil or freeze unless conditions were controlled extremely carefully. Heterogeneous materials resulted as shown in **Figure 3.3.** In **Figure 3.3** an area having a high volume percentage of dendritic VC particles can be seen. The adjacent area contains much less dendritic VC but has eutectic VC particles and greater amounts of α. Also evident in the microstructure is a crack lying on the border between the two areas.

The larger ingots were held above liquidus temperatures for extended periods while on-line C analysis was done, allowing induction stirring to produce more homogeneous alloys. Material was cut from these 7kg ingots and melted in the button arc furnace as described for Phase 1 and 2 alloys.

3.3. Specimen preparation for X-ray diffraction, metallography, hardness tests, wear tests, density measurements, chemical analysis, Mössbauer spectroscopy, TEM analysis and Jominy tests.

Phase 2 alloys were tested in both the induction melted and arc melted conditions. Samples tested after induction melting are referred to as "as cast" alloys and are designated by a postscript "C". Those having undergone button arc melting are called "arc melted" alloys and are designated by a postscript "A".

Sections about 15x100x100mm were cut from the 7kg induction melted Phase 3 alloy as cast ingots, using a high speed silicon carbide cutoff wheel and copious amounts of coolant. Difficulty was experienced during the sectioning of some alloys due to their high hardness. These sections and the arc melted ingots from certain Phase 1, 2 and all Phase 3 alloys were surface ground to obtain flat surfaces on opposite sides of the samples. Where possible cubic specimens of about 15mm a side, were cut from these samples. These were mounted and polished with diamond to a 1μm finish (alumina was found to be an inadequate polishing medium which left the VC particles standing proud of the surface or spalled). The polished surfaces were used for metallography, X-ray diffraction analysis and hardness measurements.

From the same surface ground as cast sections and arc melted ingots, cylinders 10mm in diameter were cut by spark erosion using a copper tube as the electrode. These cylinders were used for 2 and 3 body abrasion tests and density measurements.

Pieces of about 50g were removed from Alloys VF576, VF577, VF578, VF609, and all Phase 3 alloys in both the as cast and arc melted conditions. These were crushed in a 150tonne press until all the particles were below 1mm in size. Alloys VF576, VF577, VF609, 681C, AF583C, AF584C, AF585C, AF588C and AF589C were sieved and the fines used for Mössbauer spectroscopy. The coarser particles were analysed chemically. The balance of the alloys were more ductile allowing shavings to be obtained using a drill press for chemical analysis.

Thin sections of Alloy VF576 were prepared by spark erosion of 300–500 μm thin slices. These slices were glued with cyanate acrylate glue to glass slides and polished on 15μm diamond powder down to a thickness of about 100μm. Discs 3mm in diameter were punched out of the 100μm thin slices and ion–milled until electron transparent, i.e. down to about 0.2μm. Electrolytic thinning techniques using various electrolytes were attempted but were found to be unacceptable due to the preferential removal of certain phases. The thinned discs were examined in a 100kV Phillips 100C TEM.

Alloy AF587C was made to test the hardenability of an alloy with a fully γ matrix at elevated temperatures. The hardenability was tested using modified Jominy tests. AF587C was melted and poured into a graphite mould in order to obtain a 25mm diameter rod, about 300mm long. From this rod 3, 50mm length pieces were cut. Two small mild steel rods of 15mm length and 3mm diameter were tack welded onto the circumference on the end of the test specimens to hold them in place during Jominy tests.

3.4. Stoichiometric and density calculations

Stoichiometric calculations were performed using the chemical analysis of the alloys. Two sets of these calculations were performed assuming the formation of $VC_{0.88}$ and $VC_{0.75}$. The calculations were based on the following assumptions and material properties:

i) V reacts preferentially with C to form either $VC_{0.75}$ or $VC_{0.88}$.

ii) Any excess C forms Fe_3C.

iii) Any excess V forms a solid solution in the α.

iv) The densities of the phases are :

$VC_{0.88} = 5.57\ g/cm^3$

$VC_{0.75} = 5.4\ g/cm^3$

$Fe_3C = 7.7\ g/cm^3$

$Fe = 7.87\ g/cm^3$.[36]

The amount and volume percentages of each phase were calculated based on these assumptions. The ratio of Fe to V in α was also calculated.

Using these assumptions, the expected density of the alloys was calculated for comparison with the measured results.

From the results of the chemical analysis, the expected volume fractions of the different phases in the alloys were determined using the 500°C isotherm of the Fe–V–C phase diagram. The volume percentage of primary phase predicted by the liquidus surface of the Fe–V–C phase diagram, together with the approximate liquidus temperature were also determined.

The ratio of Fe_3C to α and the amount of V in α were calculated and these results compared with those obtained from Mössbauer spectroscopy.

3.5. X–ray diffraction analysis

X–ray diffraction analysis were carried out on freshly polished, scratch free samples of each alloy prepared as described in Section 3.3. This was mounted into an aluminium holder by means of plasticine. Care was taken to get the surface of the sample and the holder exactly on the same plane to ensure optimum experimental conditions. The sample holder was positioned in the diffractometer so that only the sample was exposed to X–rays.

The X–ray diffraction was performed using a computer controlled Philips PW 1820 diffractometer. A copper source was used with a graphite monochromator and was operated at 40kV, 30mA. A 1° divergent slit and 0.2° receiving slit were used. The scans were carried out from 25 to 140° in steps of 0.02° over 112 minutes. This period allowed the counts to exceed 4000 per channel on the 100 I/I_o peak for every sample.

Prior to every scan a standard silicon specimen was run to check the position of the 56,12° peak. A warm up period of about 1/2 hour was required to ensure stability of the peak of 56,12° to ±0.01°. This variation in 2θ angle resulted in d–spacings ranging from 1.6372 to 1.6377, a difference of 0.0005Å, and gave an indication of the expected machine error.

Many attempts were made to identify the phases in the alloys. One technique tried relied on the calculation of the lattice parameter using the four most intense peaks. These were then plotted against the Nelson–Raleigh function. The resultant intercept of the straight line was taken as the lattice parameter. The result was compared to values from the literature.

3.6. Mössbauer Spectroscopy

Mössbauer Spectroscopy was carried out to gain detailed information on the composition and constitution of the Fe–containing phases. Alloys VF576, VF607, VF609, 681C, AF583C, AF584C, AF585C, AF588C and AF589C were analysed by this technique. The powder samples were prepared as described in Section 3.3.

The Mössbauer technique relies on measuring the influence of surrounding atoms on the electron orbitals of paramagnetic atoms. The results give a measure of the effect of adjacent atoms on the paramagnetic atoms. In the experimental set–up the paramagnetic atoms are Fe surrounded by either V or C. The number of Fe atoms having only Fe neighbours, those having one V and the rest Fe neighbours etc, were measured by this technique. Thus the Fe containing phases could be accurately described.

In the Fe–V–C system only Fe exhibits magnetic properties. Based on the chemical analysis of the alloys, each powder sample contained 10mg of Fe. Tests were run for 2 – 5 days in either liquid nitrogen and/or at ambient temperature (ie. 80K or 293K). The γ–ray source used was ^{57}Co operated at ~20mCi. A gas counter detector was used and operated at 1 atm and 2700V. It counted continuously over 1000 channels on a linear velocity scale in the range –10 to +10 mm/s.

The resulting data was analysed using computer techniques to calculate:

1) the proportion of α to Fe_3C present and,
2) the stoichiometry of α, ie the ratio of V to Fe in α.

As the technique relies on the magnetic interference of the Fe on the γ photons, the VC_{1-x} phase which contained almost no Fe and has no magnetic field was "invisible". The calculations were all done using atomic or molar percentages and based on the fact that the VC_{1-x} phase is invisible.

3.7. Density measurements

The density of the alloys was obtained using the Archimedes principle. The wear specimens described in **Section 3.3** were cleaned and weighed (MAir) before abrasion testing. A thin copper wire was hung from the hook on a Metler balance. One end of the wire was submerged in a beaker of distilled water, containing 1 drop of Tepol dish washing liquid and the mass recorded (MWire). The Tepol allowed the extremely thin wire to overcome the surface tension of the water and sink below the surface. One end of the wire was then tied around the sample. This combination was then suspended from the hook into the beaker of water and the mass recorded (MWater). The density of the sample was then calculated using the formula

$$\text{density} = \frac{(\text{density of water}^{i}) \times (\text{MAir})}{\text{MAir} - (\text{MWater} - \text{MWire})}$$

Note i) Density of water assumed to be 1,000g/cm^3.

3.8. Metallography

Metallography was performed to determine the phases present, their morphology, size and volume percentage. The phases were determined by selective etching.

It was found that a pre-etch in 2% nital for between 5 to 30 seconds revealed the pearlite. Following this with a 30second electrolytic etch at 1.5V in lead acetate revealed the VC_{1-x} phase. The combination gave the best overall results. The lead acetate deposited an interference layer on the VC particles, the rate of deposition being dependent on the orientation of the carbide particles. The different thickness interference layers showed as

different colours in light microscopy and revealed differences in the orientation of the carbide particles.

Nital revealed the pearlite colonies, α and Fe_3C. The Fe_3C was distinguished from the α by means of microhardness measurements. For optimum results from the etching process the following precautions were taken :

- All equipment used in mixing and etching was well rinsed with distilled water to avoid contamination of the etchant. Contamination resulted in the erratic results.
- The specimens were partially submerged in the etchant. The electrode made contact with the dry part of the specimen above the electrolyte without coming into contact with the solution. If contact with the solution occurred, the results became erratic. Using this technique a less expensive copper anode could be used instead of a platinum one.
- The electrode, all connections and the stainless steel cathode were cleaned prior to etching. 1000 grit water paper was found to be most effective for this cleaning process.
- After etching the sample was rinsed by running alcohol across the surface. The alcohol jet was not allowed to impinge directly onto the etched surface, lest the deposited interference layer be removed.
- Care was taken to avoid inhaling the fumes from the reaction as these could contain lead.

Image analysis was done in two stages. In the first stage the volume percentage of pearlite was measured using a point counting technique on a Neophot optical microscope. The samples were etched in 2% nital. 42 fields or more were measured using a 16 point grid, according to ASTM standard specification E562, 1985. This same technique was used to determine the volume percentage of graphite which occurred in Alloys AF589A and AF589C.

In the second stage the VC and graphite phases were analysed using a Kontron system on an IBAS I and II machine. Samples were repolished and etched in lead acetate. 10 fields were analysed on each sample using a field resolution of 0.75μm. A linear intercept method was

used. The technique relied on lines which were superimposed horizontally onto the field of view. These lines were evenly spaced and the size of the VC particle determined by the number of pixels on a line which intersected a VC particle. In this manner the size, volume percentage, perimeter of the carbide particles, and the mean free path between carbide particles were determined. The total volume percentage of the other phases was determined by difference.

3.9. Scanning electron microscopy (SEM)

SEM was conducted using secondary electron imaging of both metallographic and wear specimens. Improved resolution was obtained on metallography samples by slight over etching. A thin carbon coating removed fluorescence caused by the charging of the VC particles. Back scattered images revealed the position of VC particles on metallography and wear samples. The distribution of elements in the phases was determined using both spot energy–dispersive spectroscopy (EDS) and dot–mapping. Both used accelerating voltages of 20kV. Higher resolution images were obtained by reducing the accelerating voltages to between 8 to 15kV and raising the stage.

The phases and their morphologies were characterised and the effect of these on the wear pattern investigated. The effect of hardness indentations on VC particles was also examined.

3.10. Transmission electron microscopy (TEM)

The specimens were prepared as described in Section 3.3. TEM work was performed on a Phillips 100C microscope. The microstructure was studied in general and the phases analysed by electron diffraction using the selected area diffraction technique (SAD). From these the VC_{1-x} lattice parameter was calculated assuming a cubic structure. Only alloy VF576 was examined by TEM. An aluminium foil was used to determine the effective camera length for the calculations from the diffraction patterns obtained.

3.11. Jominy tests

These tests were carried out to investigate the hardenability of an alloy which was known to have a purely γ matrix at elevated temperature. 3 rods were cut from the as cast Alloy AF587C. As hardfacing layers are not usually thick, (normally not much thicker than 10mm) the length of the rods was reduced from the standard 100mm to 50mm. Only the ends were ground flat and perpendicular to the sides. The remaining cylindrical side was left in the as cast condition. They were heated to 950°C and then end quenched with water according to the conditions laid down in ASTM 255. Vickers hardness traverses were made on surfaces

ground 180^{o} apart using a load of 30kg.

3.12. Macrohardness measurements

8 to 10 indentations were made on every sample using a Leco V-100-A2 Vickers macrohardness testing machine. A load of 30kg was used for the tests. The indentations were spread over the entire surface area of each polished sample. This spread took into account the heterogeneous nature of the alloys. Standard deviation of the hardness was calculated for each alloy and gave an indication of the degree of heterogeneity.

3.13. Abrasion tests

3.13.1. 3-body abrasion tests

Figure 3.4 shows a schematic view of the test rig used for the 3-body abrasion tests and **Figure 3.5** shows a schematic of the specimen holder system. The 10mm diameter spark eroded cylindrical specimens (see **Section 3.3**) were hand mounted into two of the four holders permanently attached to the wear rig load arm. They were mounted in holders 2 and 4 while holders 1 and 3 held calibration specimens of mild steel. These were cut from mild steel rod 10mm in diameter. Thus 4 specimens, of which 2 were experimental alloys, were tested simultaneously in each run. The 4 specimens were independently loaded and allowed to run against a 130mm diameter rubber coated drum under a load of 810g (0.101MPa). The drum was rotated at 100RPM forcing slurry between the specimen and the drum. The slurry consisted of 3kg of AFS 50-70 (sand size details in **Table 3.2**) silica sand in 4 l of water for each test. The slurry was recirculated by a pump and allowed to flow evenly onto the upper side of the drum. Thus the abrasive was always supplied to the contact region. New slurry was used at the start of every new batch of alloys tested.

Table 3.2 – AFS 50 – 70 sand particle size distribution according to ASTM G65–84.

U.S. sieve size	Sieve opening (μm)	% retained on sieve
40	425	none
50	300	5 max
70	212	95 min
100	150	none passing

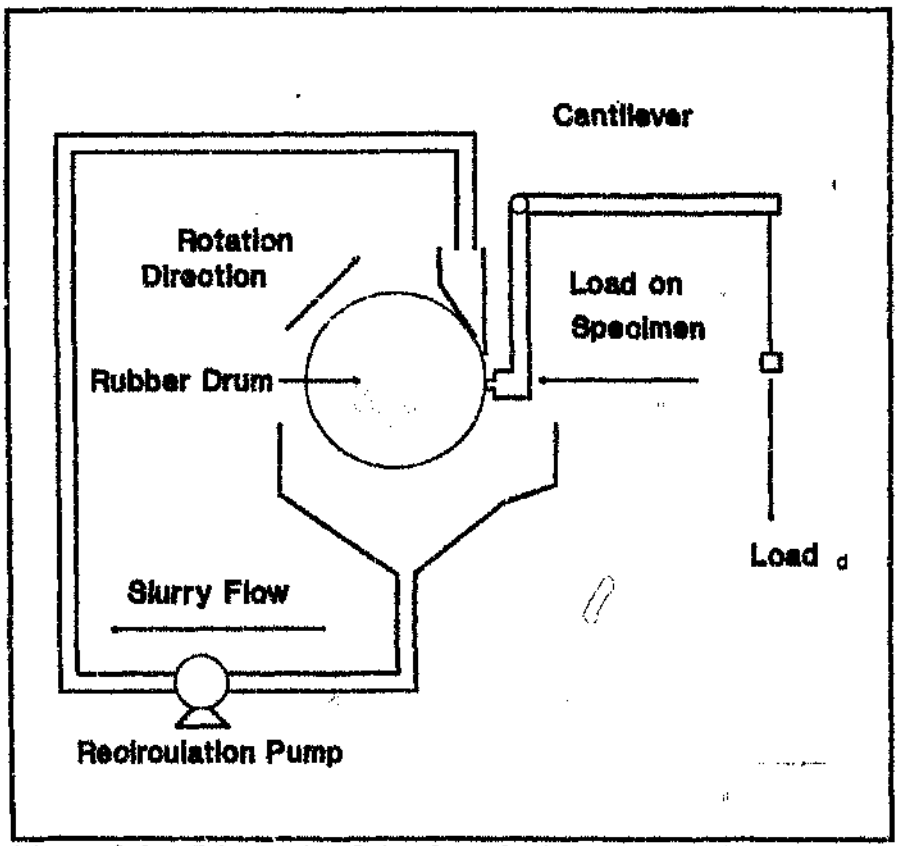

Figure 3.4 – Schematic of the three body wear test rig

A test consisted of washing, drying, weighing and mounting the specimens, followed by abrading them for 15 minutes. A run consisted of repeating these steps 5 times on the same samples. After the run, the specimens were cleaned, carbon coated and stored for SEM examination. The weight loss experienced by a test specimen fluctuated as discussed later.

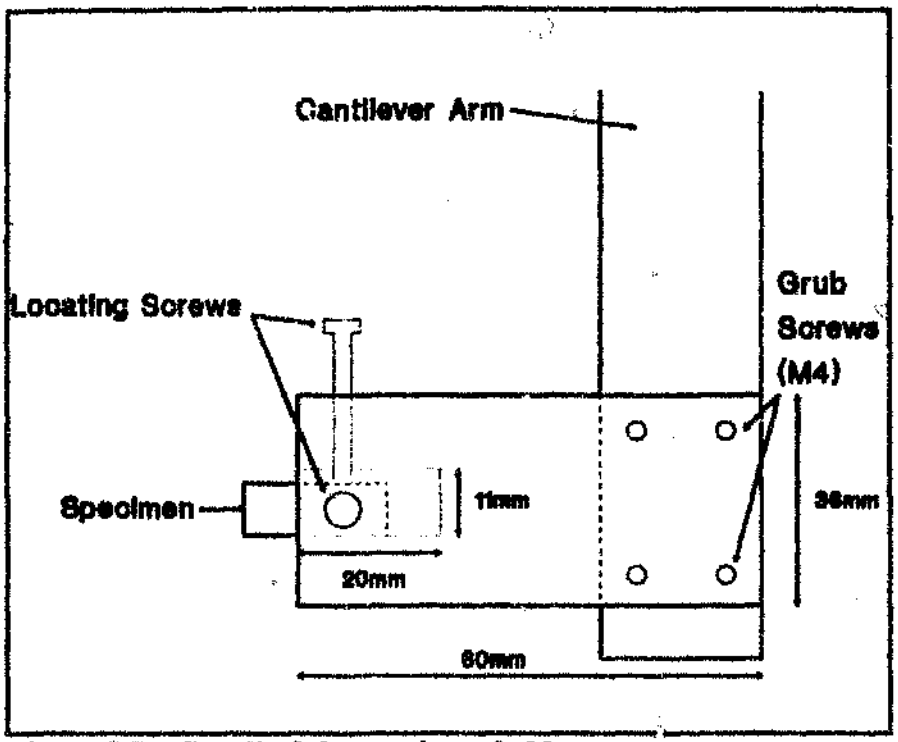

Figure 3.5 – Detail of the specimen holder system

Analysis of the weight loss fluctuations revealed that:

a) accurate control of the angle between the specimen surface and the drum could not be maintained. This resulted in variations in the stress on the wearing surface during a run. In some cases only one corner of a specimen was in contact with the rubber drum causing an increase in the stress and increases in the wear rate.

b) due to the manual reloading of the specimens, a specimen could never be reloaded in exactly the same position or orientation twice. Rotation of the specimens about their axis caused the wear ridges formed during previous wear periods to be preferentially removed, accelerating the wear rate.

3.13.2. Modified 3–body abrasion tests

On account of the weight loss fluctuations experienced in the "original" 3–body abrasion tests the causes of the fluctuations (see **Section 3.13.1**) were removed by designing a new specimen holder system in which the specimen was permanently mounted in an accurately machined holder (referred to as holder 1, see **Figure 3.6**). This fitted accurately into a second

holder (referred to as holder 2, see Figure 3.6). Holder 1 was located in holder 2 and then secured by a dowel pin which forced the specimens into the same position and orientation throughout a test run. Holder 2 was permanently attached to the wear rig load arm. The specimen was secured into holder 1 with two grub screws. The gap left between the specimen and holder 1 was filled with plasticine. This was then sealed with lacquer to prevent slurry penetration and subsequent errors in weight loss measurements. Details of this holder system are shown in Figures 3.6 and 3.7. After mounting and sealing the specimen in holder 1, holder 1 was placed flat onto the base of a surface grinder, with the specimen facing upward and held in a V–block. 30μm of material were removed per pass until the surface of the specimen was parallel to the base of holder 1. To produce the same surface finish on every specimen, a further 5 passes, in which 10μm was removed per pass, were carried out. Grinding was carried out with copious amounts of cooling fluid.

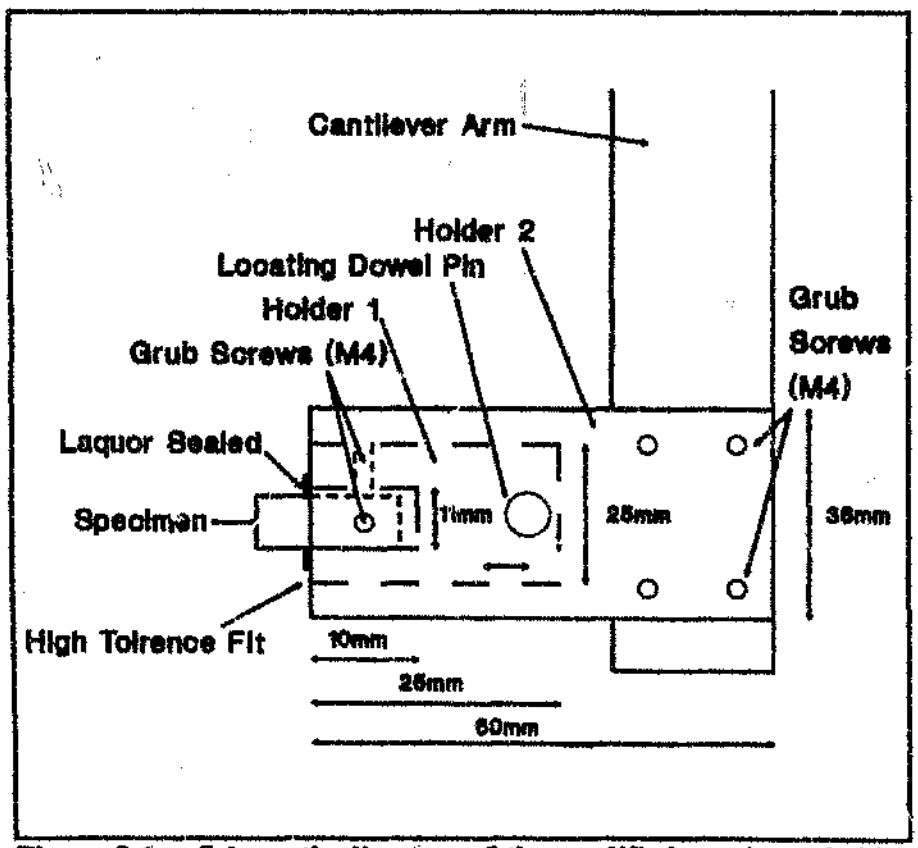

Figure 3.6 – Schematic diagram of the modified specimen holder system

Figure 3.7 - The modified holder system

The specimen mounted in holder 1 was washed, dried, weighed and placed into holder 2. This procedure was repeated for the remaining 3 specimens which were tested simultaneously in the modified test rig. The specimens were tested 5 times under the same conditions described in **Section 3.13.1** except that a period of 30 minutes was used for each test. The worn specimens were cleaned, dried, carbon coated and stored for SEM analysis.

3.14. Two-body abrasion tests

These were performed on a shaping machine. A plate was mounted on the table of the shaper and machined flat. 220 grit corundum paper was mounted on this plate. An arm designed to hold the same 2 part holder system described in **Section 3.13.2** was attached to the tool post. The arm consisted of a steel rod with a double flat at the bottom onto which holder 2 was fastened. The rod was covered by a teflon insert which ran in two teflon supports attached directly to the tool post. The teflon surfaces reduced friction to a minimum leaving the arm and specimen holders to move freely under their weight. A teflon screw located on the upper support ran through to a slot cut into the teflon insert on the specimen holder rod. This

prevented the rod from rotating about its axis during experimental runs. The design is shown in **Figure 3.8**. Care was taken to remove any dust from the teflon surfaces, prior to running tests to ensure the unhindered movement of the specimen holder up and down.

The specimens were prepared and mounted as described in **Section 3.13.2** and were tested under a 753g load (0.090MPa). A test consisted of 260 strokes each of 240mm length. The specimen moved laterally , exposing the sample to fresh abrasive paper, a distance of 195mm during the 260 strokes. A schematic of the specimen movement is shown in **Figure 3.9**. After every test the specimen and specimen holder 1, were cleaned and weighed. New corundum sandpaper was used for every test. Every sample was subjected to a run of 5 tests. **Figure 3.10.** shows the testing machine used for the two body abrasion work. After testing, the specimens were cleaned, carbon coated and stored for SEM analysis.

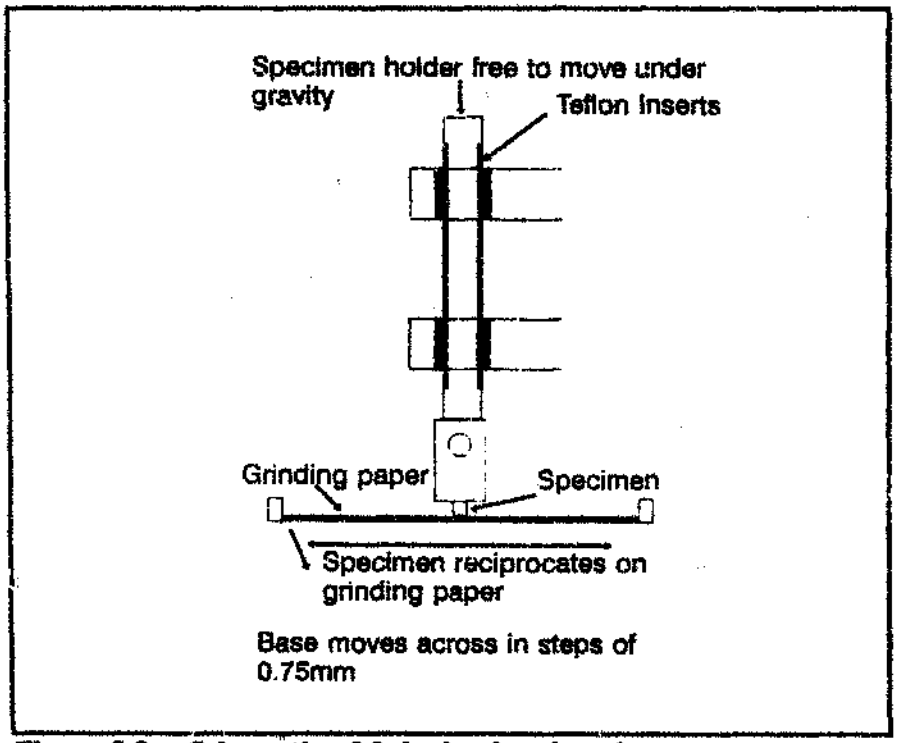

Figure 3.8 – Schematic of 2–body abrasion rig

3.15. Microhardness measurements

Hardness represents the resistance of a material to indentation[1]. Several factors influence the results obtained when measuring hardness. Vickers microhardness tests were done on a Leco M-400A microhardness testing machine to determine the effect of the carbide particle size on the measured hardness of VC particles. A 10g load was used to obtain the indentations. Circular or oval carbide particles were tested. The influence of long dendrites breaking up under load was therefore ignored. The microhardness together with the maximum and

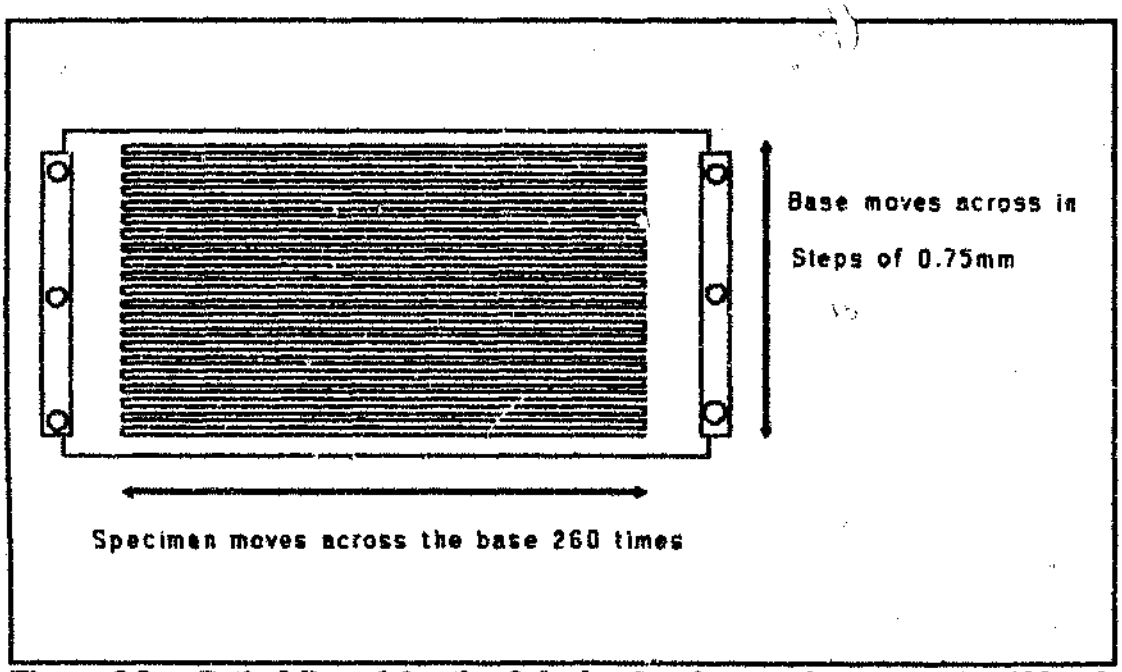

Figure 3.9 – Path followed by the 2-body abrasion specimens on the 220 grit corundum paper.

minimum dimensions of the carbide particles were measured. The carbide particle size was

calculated using the average of the maximum and minimum sizes measured. The position of the indentations in relation to the carbide particle perimeter were recorded. These tests were carried out on 2 alloys namely VF609 and 681C. These alloys had similar microstructures (α with different Fe/V ratios and differing amounts of VC). Ten indentations were made in the matrices of these alloy.

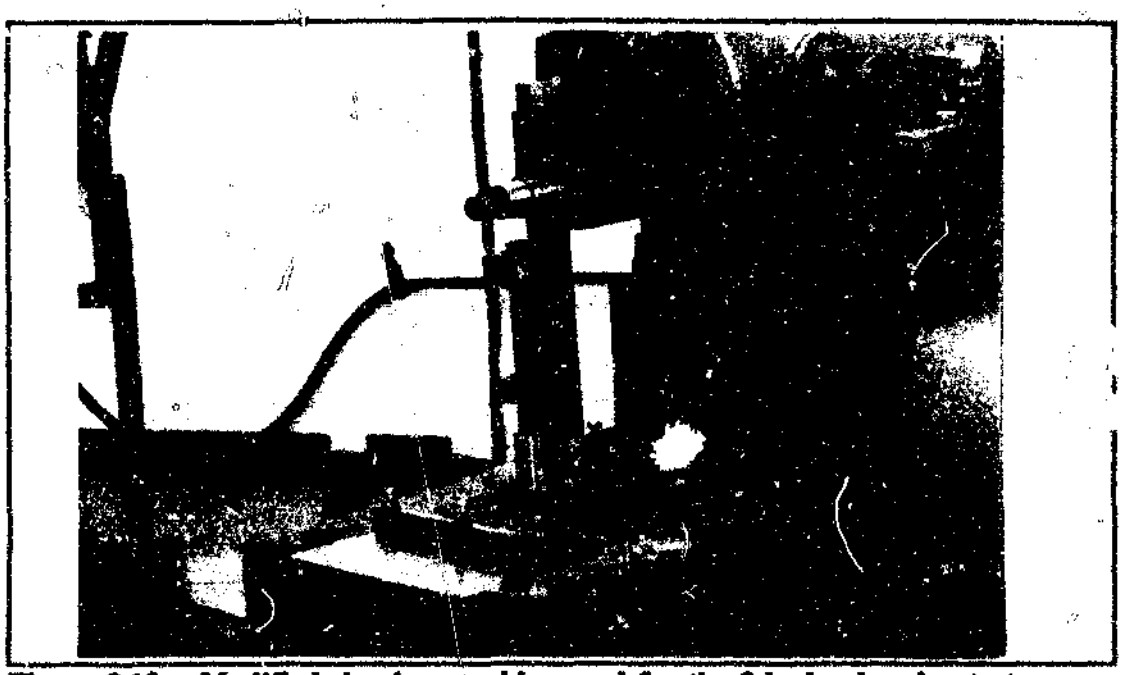

Figure 3.10 – Modified shaping machine used for the 2 body abrasion test

3.16. Commercial hardfacing materials

Comparative wear results were obtained by testing commercially available hardfacing materials. These alloys were supplied welded onto 10mm thick plate. The material had been deposited in a 35mm wide weave pattern for a distance of 300mm. The deposit had an average thickness of between 5 to 10mm.

Three alloys were tested covering the principle range of hardfacing alloys available. These included chromium carbide, mixed carbide and tungsten carbide containing alloys. All had iron matrices. The compositions are shown in **Table 3.2.** The chromium carbide and tungsten carbide types are usually used for highly abrasive applications. The mixed carbide type is used for abrasive applications in high temperatures environments.

Table 3.2 – Commercially available hardfacing alloys used for comparative wear tests[97].

Trade name	Material type	Hardness Hv[0]	Standard deviation	Total alloy additions (wt%)	Composition (wt%) [98]
HC-O	Chromium carbide	668.1	23.5	35%	5% carbon; 3% manganese; 0.8% silicon; 27% chromium
CVN-O	Mixed carbide	753.6	12.2	37%	5% carbon; 2% manganese; 0.5% silicon; 22% chromium; 7.2% niobium; 0.5% vanadium
60-3-D-O	Tungsten carbide	908.0	48.6	60%	60% tungsten-carbide

Note : i) 10 hardness measurements taken.

ii) The balance of the alloys is iron.

4. RESULTS

4.1 Alloy preparation and chemistry

Table 4.1 gives the chemical analyses of the alloys made. Due to experimental error and different chemical analysis techniques, the results do not always add up to 100% (refer to Section 5.1). Differences occurred between nominal and actual compositions. Phase 1 alloys showed a loss of both carbon and vanadium except for Alloy VC2 which "gained" some vanadium. Alloy VC4 lost significantly more vanadium and carbon than Alloy VC3. Alloy VC4 was prepared using VC particles of about 45μm while for Alloy VC3 the VC particles used were significantly smaller.

Phase 2 alloys also showed varying gains and losses of carbon and vanadium. The FeV used to make Alloys VF577, VF578, VF579, VF607, VF608 and VF609 was supplied with a test certificate stating it contained between 50 to 60% vanadium but due to mix-up in supply, actually contained between 80 to 90%. This resulted in the alloys having a higher than expected vanadium content. The carbon content also fluctuated. This error only affected the proportions of the phases and not the types of phases present. For this reason the alloys were not remade and investigated further.

Alloy VF609 was different from the rest of the materials in that it never appeared to be completely liquid during melting. When poured from the crucible into the mould it was extremely viscous. This was probably due to its high liquidus temperature.

The chemistry of Phase 3 alloys deviated less from nominal than Phase 1 and 2 alloys.

Table 4.1. - Chemical analyses of the samples.

Alloy	C wt%	CL[i] wt%	V wt%	VL[ii] wt%	Fe wt%	Al wt%	Si wt%	P wt%	S wt%
VC 2	1.7	0.1	8.7	(0.5)	90.0	0.16	<0.02	<0.01	<0.01
VC 3	1.0	0.3	8.2	0.5	90.9	0.15	<0.02	<0.01	0.02
VC 4	0.2	1.1	3.2	5.5	96.6	0.05	<0.02	<0.01	0.02
VC 5	1.4	0.5	5.9	2.3	92.3	0.10	<0.02	<0.01	<0.01
VC 6	0.8	0.6	5.9	2.8	93.6	0.09	<0.02	<0.01	0.02
VC 7	1.2	1.4	9.1	8.3	89.6	0.17	<0.02	<0.01	0.02
VC 8	1.7	2.1	9.4	8.0	89.1	0.17	<0.02	<0.01	0.025
VF576	5.8	2.3	20.9	11.3	72.6	0.35	0.07	<0.01	0.05
VF577	1.8	(0.5)	55.4	(8.7)	40.8	0.95	0.67	<0.01	0.03
VF578	2.7	0.3	64.3	(7.1)	30.9	1.10	0.78	0.02	0.045
VF579	0.8	(0.2)	26.9	(6.8)	71.5	0.46	0.27	<0.01	0.02
VF607	4.3	0.7	25.6	(5.6)	69.5	0.56	0.43	<0.01	0.02
VF609	9.5	1.4	64.3	(19.3)	28.7	1.09	0.96	0.03	0.02
681A	7.4	(0.4)	40.8	(0.8)	48.8	0.88	1.29	0.01	0.04
681C	7.2	(0.2)	41.3	(1.3)	51.2	0.85	1.41	0.01	0.05
AF583C	3.1	0.3	10.4	(0.4)	86.6	0.19	0.24	<0.01	<0.01
AF584C	5.2	0.1	19.3	0.7	76.2	0.39	0.58	<0.01	<0.01
AF585C	6.2	0.6	28.7	1.3	65.1	0.64	0.78	<0.01	<0.01
AF586A	3.4	(0.2)	47.9	(5.4)	47.7	0.84	0.80	0.01	<0.01
AF587C	4.8	0.2	20.4	(0.4)	75.1	0.62	0.37	<0.01	<0.01
AF588C	6.4	0.4	20.1	(0.1)	73.9	0.63	0.44	<0.01	<0.01
AF589C	7.5	(0.1)	17.9	2.1	74.0	0.53	0.43	<0.01	<0.01
AF583A	3.1	0.3	10.8	(0.3)	86.0	0.19	0.24	<0.01	<0.01
AF584A	5.4	(0.1)	19.1	0.7	74.5	0.34	0.48	<0.01	<0.01
AF585A	7.2	(0.4)	33.6	(3.6)	58.9	0.65	0.76	<0.01	<0.01
AF588A	6.1	0.7	17.9	2.1	75.0	0.66	0.43	<0.01	<0.01
AF589A	7.4	0	18.0	2.0	75.1	0.54	0.46	<0.01	<0.01

(i) CL – carbon lost during manufacture. Gains are indicated with bold in brackets.

(ii) VL – vanadium lost during alloy manufacture. Gains are indicated with bold in brackets.

N.B. An insufficient amount of Alloy VF608 remained after experimentation for chemical analysis to be performed.

4.2. Stoichiometric and density calculations

The chemical analyses and assumptions made in **Section 3.4** were used to calculate the expected volume and weight percentages of phases in each alloy. The VC particles were assumed to be either $VC_{0.75}$ or $VC_{0.875}$ based on literature and the X-ray diffraction data presented later. The V/Fe ratio was determined using the same assumptions. The results of these calculations are shown in **Tables 4.2** and **4.3** respectively. Based on the assumed VC_{1-x} phase formed and the densities given in **Section 3.4**, the theoretical densities were determined. These results are shown in **Table 4.4** together with the measured densities of the alloys.

The chemical analysis was used to determine the phases present on the 500°C isotherm and the liquidus surface of the Fe–V–C phase diagram. The predicted weight and volume percentages are presented in **Table 4.5**. The proportions of primary VC_{1-x} and α formed in the liquid prior to eutectic or peritectic reactions taking place are included in **Table 4.5**. The position of Phase 1, 2 and 3 alloys based on the chemical compositions are indicated on the liquidus, 1100°C and 500°C isotherms of the Fe–V–C equilibrium phase diagrams[9] in **Figures 4.1, 4.2** and **4.3** with "x", "+" and "*" respectively.

Table 4.2. – The weight and volume proportions calculated for the alloys assuming $VC_{0.75}$ formed.

Alloy	$VC_{0.75}$ wt% (vol%)	Fe_3C wt% (vol%)	FeV_α wt% (vol%)	V/Fe wt% in α
VC2	10.24 (13.30)	2.41 (2.36)	87.35 (84.34)	0.00
VC3	6.65 (8.75)	0.00 (0.00)	93.35 (91.25)	0.03
VC4	1.33 (1.78)	0.00 (0.00)	98.67 (98.22)	0.02
VC5	6.94 (9.11)	5.33 (5.27)	87.73 (85.62)	0.00
VC7	7.99 (10.45)	0.00 (0.00)	92.01 (89.55)	0.03
VC8	11.31 (14.64)	0.00 (0.00)	88.69 (85.36)	0.00
VF576	24.60 (30.38)	31.45 (29.26)	43.95 (40.36)	0.00
VF577	11.98 (15.47)	0.00 (0.00)	88.02 (84.53)	1.11
VF578	17.97 (22.75)	0.00 (0.00)	82.03 (77.25)	1.59
VF579	5.32 (7.03)	0.00 (0.00)	94.68 (92.97)	0.31
VF607	28.62 (35.03)	0.00 (0.00)	71 38 (64.97)	0.07
VF609	62.89 (69.50)	0.00 (0.00)	37.11 (30.50)	0.38
681A	48.02 (55.38)	2.76 (2.40)	49.22 (42.22)	0.00
681C	47.91 (55.30)	0.00 (0.00)	52.09 (44.70)	0.01
AF583C	12.24 (15.57)	18.10 (17.55)	69.66 (66.69)	0.00
AF584C	22.71 (28 24)	25.97 (24.32)	51.32 (47.45)	0.00
AF585C	33.78 (40.60)	16.81 (15.22)	49.41 (44.17)	0 00
AF586A	22.29 (27.84)	0.00 (0.00)	77.71 (72.16)	0.61
AF587C	24.01 (29.76)	17.08 (15.94)	58.91 (54.30)	0.00
AF588C	23.60 (29.20)	41.92 (39.07)	34.48 (31.73)	0.00
AF589C	21.07 (26.21)	64.05 (60.02)	14.88 (13.77)	0.00
AF583A	12.71 (16.34)	17.79 (17.23)	69.50 (66.43)	0.00
AF584A	22.48 (27.95)	30.23 (28.32)	47.29 (43.73)	0.00
AF585A	39.54 (46.70)	18.81 (16.73)	41.65 (36.57)	0.00
AF588A	21.97 (26.27)	43.87 (41.21)	35.07 (32.52)	0.00
AF589A	21.18 (26.35)	62 29 (58.36)	16.53 (15.29)	0.00

N.B. The possibility of other phases was not considered.

Table 4.3. - The weight and volume proportions calculated for the alloys assuming $VC_{0.88}$ formed.

Alloy	$VC_{0.88}$ wt% (vol%)	Fe_3C wt% (vol%)	FeV_α wt% (vol%)	V/Fe wt% in α
VC2	9.9 (12.9)	0.0 (0.0)	90.1 (87.1)	0.01
VC3	5.8 (7.6)	0.0 (0.0)	94.2 (92.4)	0.04
VC4	1.2 (1.6)	0.0 (0.0)	98.8 (98.4)	0.02
VC5	7.1 (9.3)	2.6 (2.6)	90.3 (88.1)	0.00
VC6	4.7 (6.2)	0.0 (0.0)	95.3 (93.8)	0.02
VC7	7.0 (9.1)	0.0 (0.0)	93.0 (90.8)	0.04
VC8	9.9 (12.9)	0.0 (0.0)	90.1 (87.1)	0.01
VF576	25.2 (31.1)	22.4 (20.8)	52.4 (48.1)	0.00
VF577	10.5 (13.6)	0.0 (0.0)	89.5 (86.4)	1.15
VF578	15.7 (20.0)	0.0 (0.0)	84.3 (80.0)	1.66
VF579	4.7 (6.2)	0.0 (0.0)	95.3 (93.8)	0.32
VF607	25.0 (31.0)	0.0 (0.0)	75.0 (69.0)	0.07
VF609	54.9 (62.1)	0.0 (0.0)	45.1 (37.9)	0.66
681A	43.1 (50.5)	0.0 (0.0)	56.9 (49.5)	0.11
681C	41.9 (49.2)	0.0 (0.0)	58.1 (50.8)	0.12
AF583C	12.6 (16.2)	13.1 (12.7)	74.3 (71.1)	0.00
AF584C	23.3 (28.4)	17.9 (16.7)	58.8 (54.3)	0.00
AF585C	34.7 (41.7)	3.6 (3.3)	61.7 (55.7)	0.00
AF586A	19.8 (24.9)	0.0 (0.0)	80.2 (75.1)	0.66
AF587C	24.6 (30.5)	8.5 (7.9)	66.8 (61.6)	0.00
AF588C	24.3 (30.0)	33.3 (31.0)	42.4 (39.0)	0.00
AF589C	21.6 (26.9)	56.6 (53.0)	21.8 (20.2)	0.00
AF583A	13.0 (16.7)	12.8 (12.4)	74.1 (70.9)	0.00
AF584A	23.1 (28.7)	21.5 (20.1)	55.5 (51.2)	0.00
AF585A	40.6 (47.9)	3.4 (3.0)	56.0 (49.1)	0.00
AF588A	21.6 (26.9)	35.7 (33.5)	42.7 (39.6)	0.00
AF589A	21.7 (27.0)	54.8 (51.3)	23.5 (21.7)	0.00

N.B. The possibility of other phases was not considered.

Table 4.4. – The calculated densities of the alloys assuming $VC_{0.76}$ and $VC_{0.88}$ formed and using the assumptions in Section 3.4. The measured values are also given.

Alloy	Theoretical Density assuming $VC_{0.76}$ formed (g/cm^3)	Theoretical Density assuming $VC_{0.88}$ formed (g/cm^3)	Measured Density (g/cm^3)
VC2	7.52	7.56	–
VC3	7.64	7.68	–
VC4	7.81	7.81	–
VC5	7.62	7.63	7.55
VC7	7.59	7.63	7.64
VC8	7.49	7.56	7.58
VF576	7.06	7.11	7.03
VF577	7.47	7.54	–
VF578	7.29	7.39	–
VF579	7.68	7.71	–
VF607	6.99	7.14	6.96
VF609	6.15	6.43	6.03
681A	6.49	6.70	6.50
681C	6.50	6.73	6.53
AF583C	7.43	7.46	7.45
AF584C	7.12	7.13	7.12
AF585C	6.83	6.95	6.80
AF586A	7.17	7.28	6.56
AF587C	7.10	7.14	7.09
AF588C	7.08	7.12	7.06
AF589C	7.12	7.17	6.88
AF583A	7.42	7.45	7.45
AF584A	7.12	7.17	7.09
AF585A	6.68	6.75	6.86
AF588A	7.14	7.19	6.76
AF589A	7.12	7.16	7.00

N.B. The possibility of other phases was not considered.

Table 4.5. – The phases present in the alloys on the 500°C isotherm and liquidus surface of the Fe–V–C phase diagram. The liquidus temperature is also given.

Alloy	α vol%	VC_{1-x} vol%	Fe_3C vol%	η vol%	V_2C vol%	θ vol%	VC_{1-x} vol% at solidus temp.	α vol% at solidus temp.	Liquid temp (°C)
VC2	89.5	10.5	–	–	–	–	–	13	1370
VC3	90.1	–	–	–	8.9	–	–	46	1410
VC4	94.1	–	–	5.9	–	–	–	86	1500
VC5	92.5	7.5	–	–	–	–	–	33	1390
VC6	93.8	6.2	–	–	–	–	–	55	1450
VC7	90.2	4.9	–	–	4.9	–	–	35	1390
VC8	89.1	10.9	–	–	–	–	–	13	1350
VF576	52.9	26.5	20.6	–	–	–	20	–	1390
VF577	–	–	–	–	26.9	73.1	–	–	1500
VF578	–	–	–	–	16.8	83.2	–	–	1550
VF579	77.0	–	–	23.0	–	–	–	–	1400
VF607	69.8	30.2	–	–	–	–	27	–	1415
VF609	22.6	77.4	–	–	–	–	60	–	2100
681A	48.8	50.2	–	–	–	–	42	–	1610
681C	48.8	50.2	–	–	–	–	40	–	1610
AF583C	74.2	13.0	12.8	–	–	–	4	–	1320
AF584C	59.3	24.1	16.6	–	–	–	17	–	1380
AF585C	58.5	35.8	5.7	–	–	–	28	–	1460
AF586A	–	–	–	98.2	1.8	–	5	–	1500
AF587C	64.7	25.4	9.9	–	–	–	17	–	1400
AF588C	41.1	25.5	33.4	–	–	–	20	–	1390
AF589C	25.3	25.9	48.8	–	–	–	17	–	1340
AF583A	73.3	11.1	15.6	–	–	–	5	–	1320
AF584A	56.8	23.6	19.6	–	–	–	17	–	1380
AF585A	57.5	44.5	2.0	–	–	–	34	–	1500
AF588A	36.8	21.6	41.6	–	–	–	16	–	1350
AF589A	20.7	22.4	56.9	–	–	–	12	–	1340

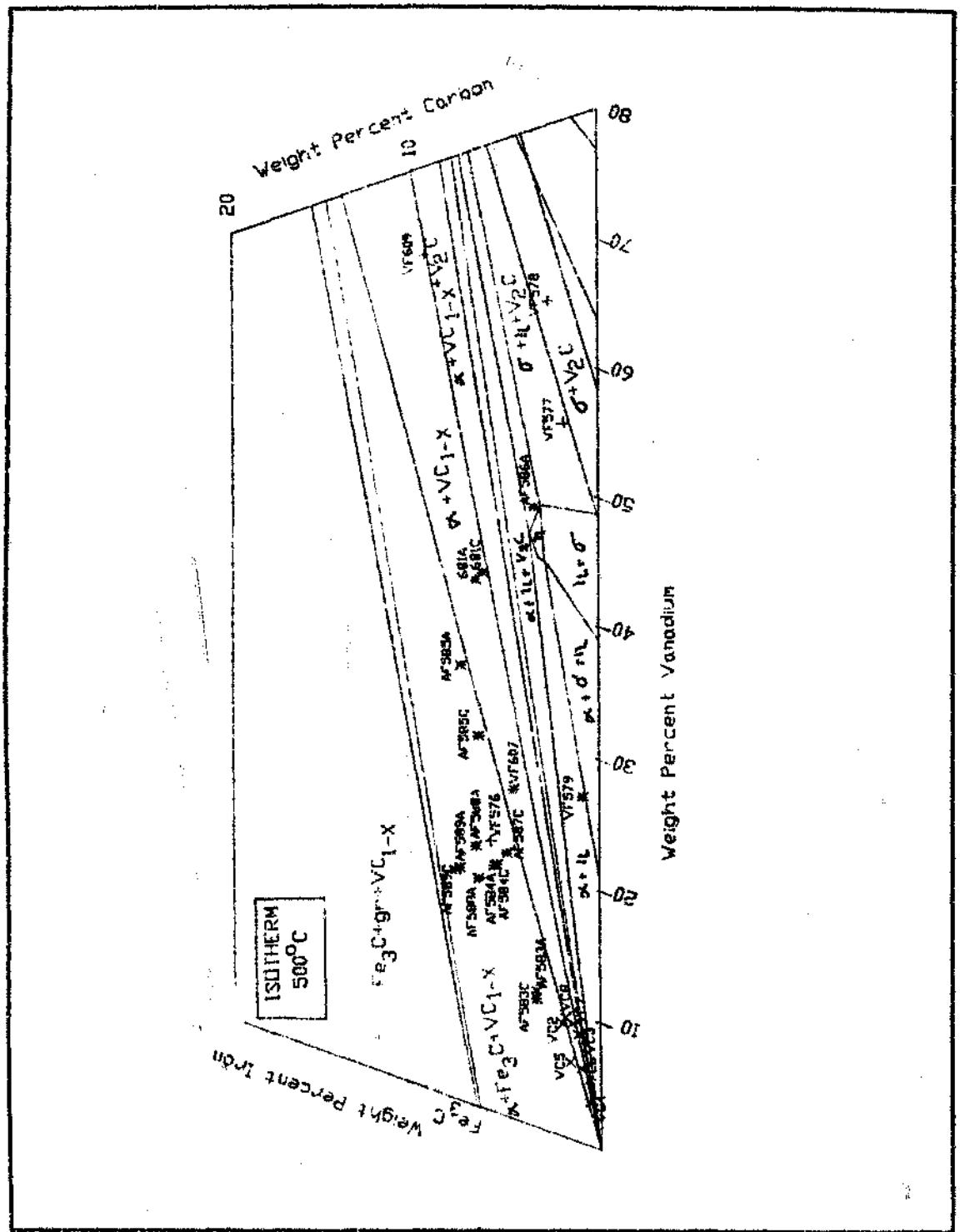

x – Phase 1 alloys
+ – Phase 2 alloys
*** – Phase 3 alloys**

Figure 4.1. – Position of alloys on the liquidus surface of the Fe–V–C equilibrium phase diagram[9].

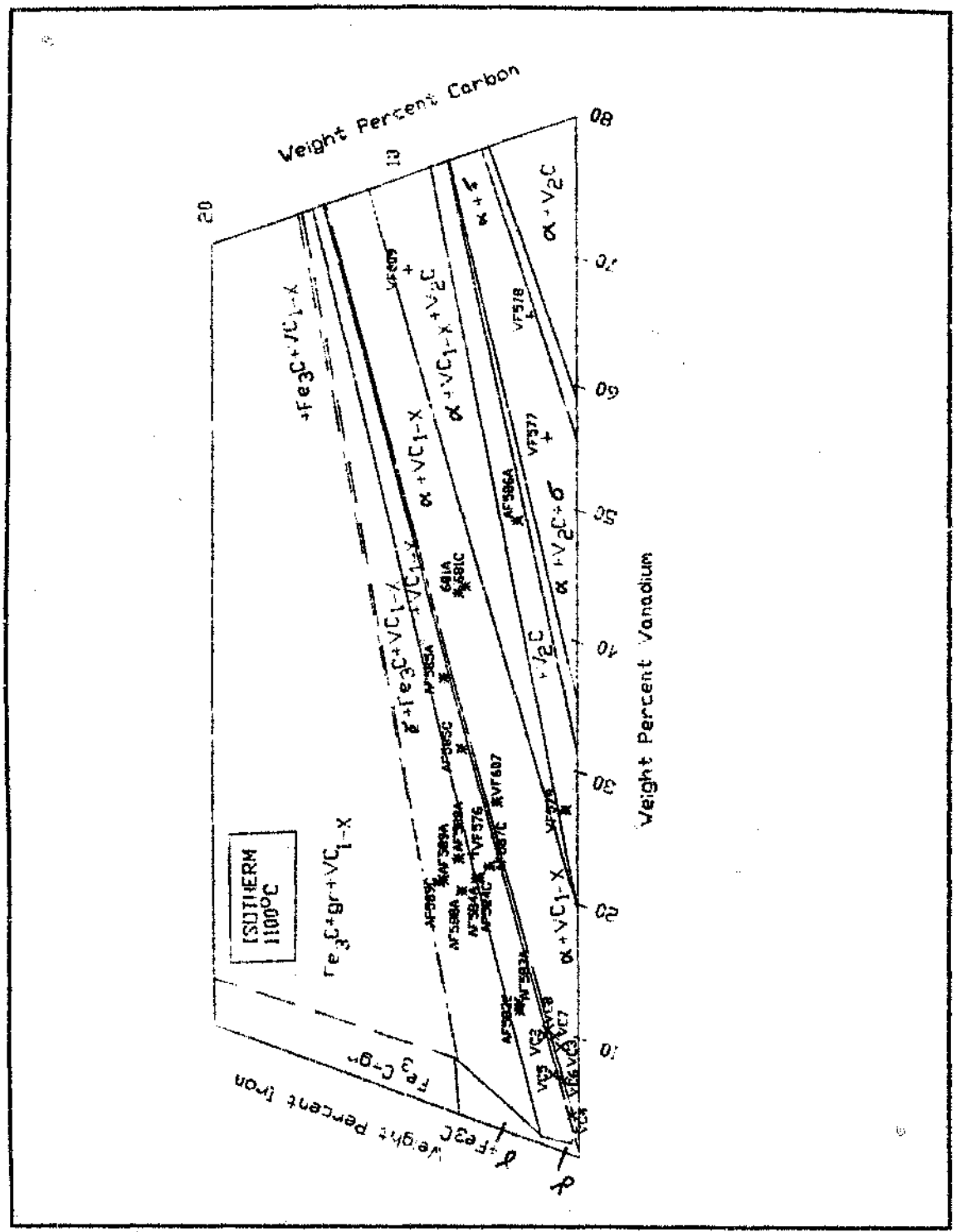

x – Phase 1 alloys
+ – Phase 2 alloys
*** – Phase 3 alloys**

Figure 4.2. – Position of alloys on the 1100°C isotherm of the Fe–V–C equilibrium phase diagram[9].

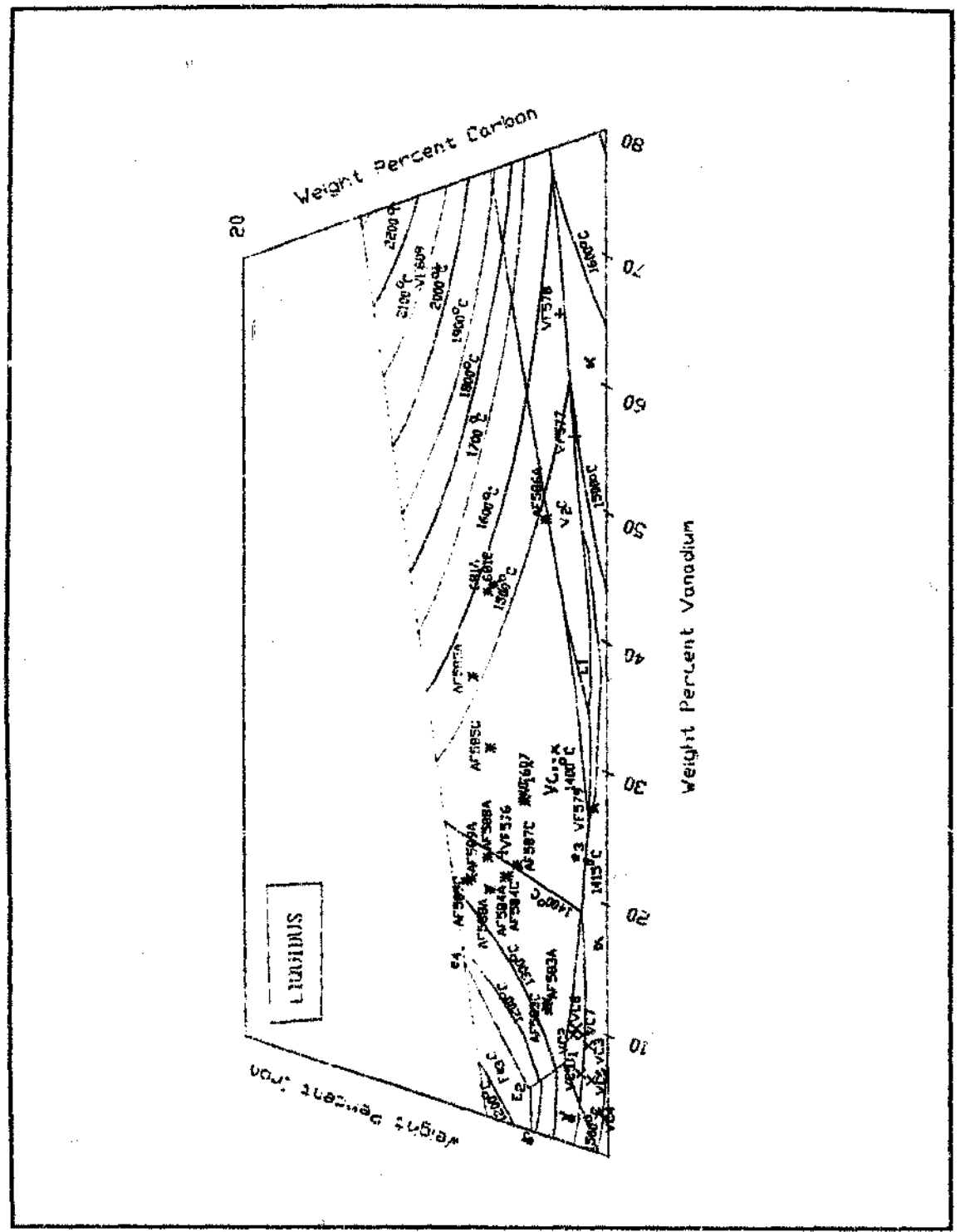

x – Phase 1 alloys
+ – Phase 2 alloys
*** – Phase 3 alloys**

Figure 4.3. – Position of alloys on the 500°C isotherm of the Fe–V–C equilibrium phase diagram[9].

4.3. X–ray diffraction analyses

Results obtained from X–ray diffraction analysis indicated the presence of α, either $VC_{0.75}$ or $VC_{0.875}$ and Fe_3C. Other peaks were seen but due to low counts could not be positively identified. The d–spacings of the two carbide types obtained from the Joint Committee on Powder Diffraction Standards (JCPDS) file, showed the peaks for the two carbides to be close to each other. Although the full diffractograms were used to identify the phases, only the four or five highest peaks were used for lattice parameter calculation purposes. The standards for pure Fe and the α solid solution with V (α–FeV) are shown in **Table 4.6**. This table shows the measured d–spacings for α. The calculated lattice parameters are also given. The 4 major d–spacings of the VC_{1-x} phase measured for the alloys are given with the calculated lattice parameters in **Table 4.7**. A large number of different Fe_XC_Y phases appear in the JCPDS files. The relatively low volume percentage of Fe_XC_Y which was present in the alloys together with d–value overlaps made it extremely difficult to determine which Fe_XC_Y phases were present. Due to the low volume percentages of Fe_XC_Y present in the alloys (ie below 5 vol%) the possible presence of other Fe_XC_Y phases could not be excluded, but the only identified Fe_XC_Y was the orthorhombic Fe_3C phase or cementite. The five major d–spacings for this phase are shown in **Table 4.8** were these could be obtained. The standard Fe_3C phase peaks are also shown.

Table 4.6. – X–ray diffraction data showing the d–spacings of the 5 highest α peaks and the lattice parameters calculated from them.

Alloy	Peak 1 (110)	Peak 2 (211)	Peak 3 (310)	Peak 4 (220)	Peak 5 (200)	Latt. Param.
FeV(1)	2.0320	1.1820	0.9180	1.0260	1.4440	2.8739
Fe(1)	2.0269	1.1702	0.9064	1.0134	1.4332	2.8665
VC2	2.0263	1.1714	0.9079	1.0146	1.4348	2.8694
VC3	2.0257	1.1720	0.908[illegible]	1.0151	1.4344	2.8667
VC4	2.0270	1.1716	0.9078	1.0152	1.4355	2.8701
VC5	2.0253	1.1710	0.9073	1.0140	1.4333	2.8655
VC6	2.0233	1.1707	0.9073	1.0140	1.4330	2.8642
VC7	2.0274	1.1722	0.9084	1.0153	1.4358	2.[illegible]714
VC8	2.0251	1.1714	0.9077	1.0147	1.4348	2.8690
VF576	2.0186	1.1701	0.9081	1.0138	1.3320	2.4505
VF607	2.0263	1.1725	0.9086	1.0159	1.4366	2.8726
VF609	2.0309	1.1750	0.9113	1.0177	1.4395	2.8793
AF583A	2.0257	1.1717	0.9080	1.0151	1.4344	2.8665
AF583C	2.0242	1.1700	0.9066	1.0136	1.4321	2.8616
AF584A	2.0246	1.1713	0.9078	1.0141	1.4348	2.8709
AF584C	2.0221	1.1693	[illegible]060	1.0128	1.4301	2.8563
AF585A	2.0240	1.1722	0.9068	1.0131	1.4342	2.8728
AF585C	2.0214	1.1699	0.9065	1.0129	1.4377	2.8843
AF586A	2.0407	1.1775	0.9153	1.0158	1.4452	2.9381
AF587C	2.0246	1.1707	0.9076	1.0137	1.4322	2.8622
AF588A	2.0238	1.1708	0.9072	1.0143	1.4341	2.8673
AF588C	2.0272	1.1724	0.9081	1.0147	1.4358	2.8735
AF589A	2.0255	1.1720	0.9072	1.0148	1.4346	2.8663
AF589C	2.0236	1.1706	0.9073	1.0142	1.4321	2.8601
681C	2.0276	1.1725	0.9086	1.0156	1.4363	2.8725

(1) Standard d–spacings

Table 4.7. – X-ray diffraction data showing the d-spacings of the 4 highest VC_{1-X} peaks with the calculated lattice parameters based on the assumption that cubic $VC_{0.75}$ or $VC_{0.875}$ formed.

Alloy	Peak 1 (111)	Peak 2 (200)	Peak 3 (220)	Peak 4 (311)	$VC_{0.75}$ Latt. param.	Corr. Coef.	$VC_{0.875}$ Latt. param.	corr. Coef.
$VC_{0.75}$(1)	2.400	2.070	1.470	1.250	4.16			
$VC_{0.875}$(1)	2.405	2.082	1.473	1.256			8.33	
VC 2	2.3921	2.0772	1.4686	1.2536	4.1639	0.823	8.3278	0.823
VC 3	2.3921	2.0720	1.4661	1.2526	4.1635	0.945	8.3270	0.945
VC 4	2.3961	–	1.4650	1.2529	–	–	–	–
VC 5	2.3945	2.0763	1.4693	1.2536	4.1631	0.967	8.3262	0.967
VC 6	2.3912	2.0733	1.4659	1.2517	4.1541	0.861	8.3082	0.861
VC 7	2.3955	2.0747	1.4680	1.2519	4.1542	0.966	8.3084	0.966
VC 8	2.3930	2.0709	1.4687	1.2534	4.1576	0.804	8.3152	0.804
VP576	2.3866	2.0702	1.4689	1.2529	4.1698	0.987	8.3396	0.987
VP607	2.3878	2.0681	1.4662	1.2508	4.1567	0.974	8.3134	0.974
VP609	2.3811	2.0650	1.4626	1.2472	4.1455	0.974	8.2910	0.974
681C	2.3921	2.0720	1.4609	1.2503	4.1523	0.996	8.3046	0.996
AF583A	2.3964	2.0774	1.4703	1.2548	4.1670	0.988	8.3340	0.988
AF583C	2.3995	2.0788	1.4716	1.2551	4.1671	0.989	8.3342	0.989
AF584A	2.3958	2.0760	1.4703	1.2538	4.1646	0.978	8.3292	0.978
AF584C	2.3964	2.0772	1.4700	1.2541	4.1641	0.985	8.3282	0.985
AF585A	2.3964	2.0765	1.4693	1.2533	4.1601	0.992	8.3202	0.992
AF585C	2.3915	2.0738	1.4680	1.2528	4.1616	0.985	8.3232	0.985
AF587C	2.3964	2.0760	1.4691	1.2537	4.1613	0.984	8.3226	0.984
AF588A	2.3955	2.0742	1.4706	1.2543	4.1678	0.949	8.3356	0.949
AF588C	2.4004	2.0792	1.4719	1.2551	4.1666	0.961	8.3332	0.961
AF589A	2.4007	2.0785	1.4719	1.2552	4.1676	0.925	8.3352	0.925
AF589C	2.3946	2.0763	1.4700	1.2544	4.1672	0.991	8.3344	0.991

(1) Standard d-spacings

Table 4.8. – X–ray diffraction data showing the d–spacings of the 4 highest Fe_3C peaks.

Alloy	Peak 1 (103)	Peak 2 (210)	Peak 3 (021)	Peak 4 (121)	Peak 5 (022)
Fe_3C(1)	2.010	2.060	2.380	2.100	2.020
VC2	–	–	–	–	–
VC3	–	–	–	–	–
VC4	–	–	–	–	–
VC5	–	2.0763	2.3945	2.1046	2.0253
VC6	–	–	–	–	–
VC7	–	–	–	–	–
VC8	–	–	–	–	–
VF576	2.0186	2.0702	2.3866	2.0969	–
VF607	–	–	–	–	–
VF609	–	–	–	–	–
AF583A	2.0095	2.0774	2.3964	–	2.0257
AF583C	–	2.0788	2.3760	2.1022	2.0242
AF584A	–	2.0760	2.3958	2.1029	2.0246
AF584C	–	2.0715	2.3687	2.1004	2.0221
AF585A	–	2.0713	2.3964	2.1004	2.0240
AF585C	–	2.0738	2.3915	2.0981	2.0214
AF586A	–	–	–	–	–
AF587C	–	2.0760	2.3761	2.1025	2.0246
AF588A	2.0080	2.0596	2.3778	2.1004	2.0238
AF588C	2.0120	2.0792	2.4004	–	2.0238
AF589A	2.0093	2.0785	2.3796	2.1027	2.0255
AF589C	–	2.0610	2.3714	2.0981	2.0236
681C	–	–	–	–	–

(1) Standard d–spacings

4.4. Results of Mössbauer Spectroscopy

Only four of the Mössbauer Spectra obtained together with their magnetic hyperfine profiles are presented in detail. **Figure 4.4** gives the distributions for Alloys VF607, AF584C, AF588C and AF609 which are representative of the remaining results given in **Table 4.9.**

The Mössbauer spectra obtained from Alloys AF584C, AF588C and VF607 resembled the pure Fe spectra relatively closely with AF584C and AF588C showing additional peaks. The analysis of these indicated a sextet corresponding to a magnetic field smaller than 26T with an isomeric shift higher than that of α–Fe. A fit indicated that this second component had Mössbauer parameters close to those of Fe_3C.

Figure 4.4 shows the magnetic field distribution extracted from the Mössbauer spectra for the **α–FeV phase** and for the Fe_xC_Y phase. In the case of Alloy VF609, only the distribution for the α–FeV phase is given because no Fe_xC_Y phase was present. In the α–FeV phase, Fe and V were assumed to be distributed at random, so that an Fe atom could be surrounded by 8 or 7 or 6, etc., Fe atoms and 0 or 1 or 2, etc., V atoms. The magnetic field depends on the number of magnetic neighbours and the presence of V neighbours is expected to reduce the magnetic field of pure Fe (33T at 300K) because V has no magnetic moment. As shown in **Figure 4.4** the magnetic hyperfine fields obtained were as follows:

Alloy VF607 : 33, 31, 29, 27 and 25 T
Alloy AF584C : 33, 31, 27 T
Alloy AF588C : 33, 31, 27 T
Alloy VF609 : 33, 31, 27 T

Thus, the reduction in magnetic field appeared to be of the order of 2.1±0.4 T per neighbour. The magnitude of this reduction in magnetic field agrees with the results obtained when Fe atoms were substituted by Al or Ti atoms[28,29] and the work done on FeV alloys[30], where the reduction per V atom in the nearest neighbours shell is not exactly proportional to the number of V neighbours due to the fact that : (1) there is more than one possible configuration with an Fe atom surrounded by more than one V atom, and (2) the influence of the next–nearest neighbours is not negligible.

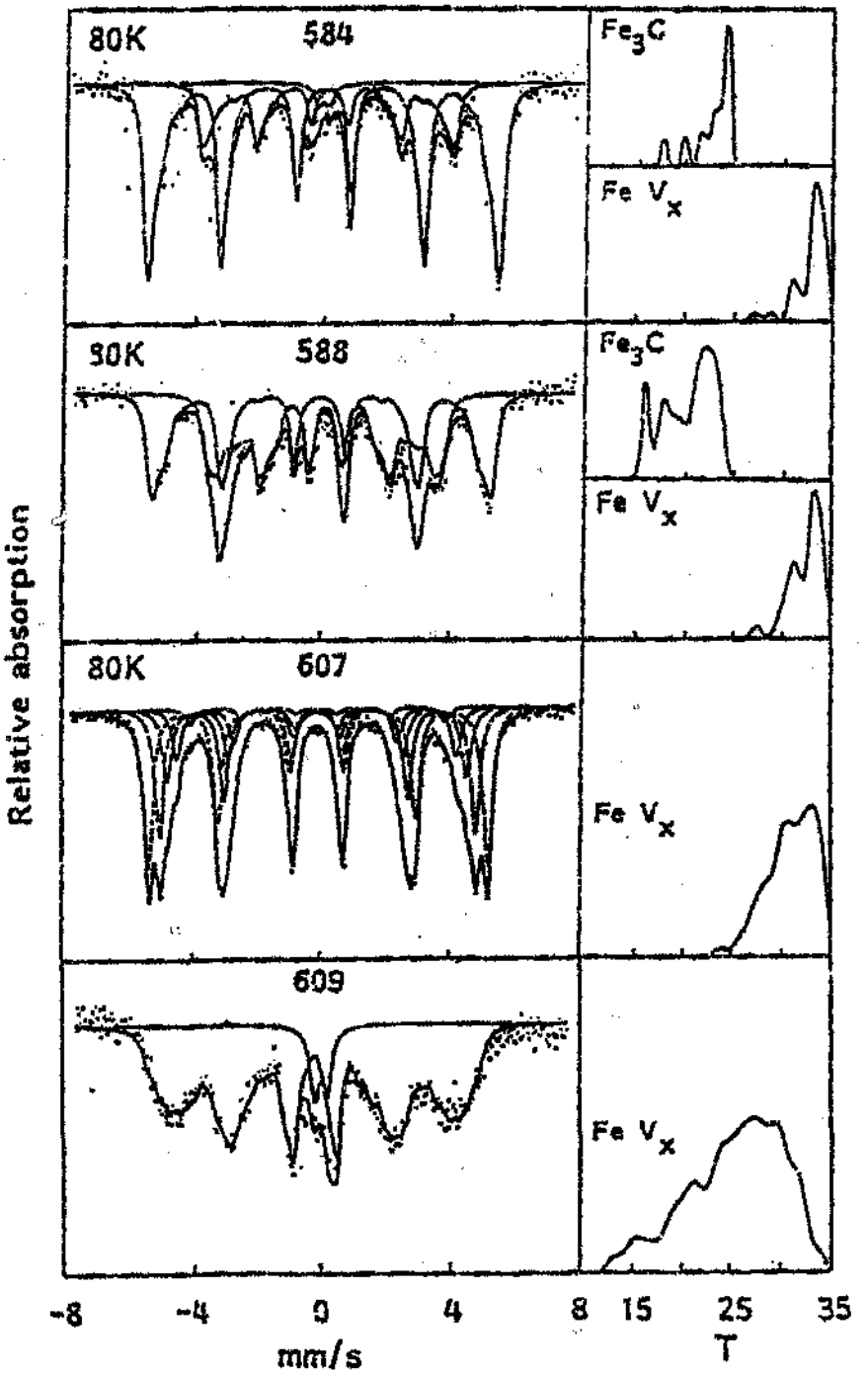

Figure 4.4. – Mössbauer spectra obtained from alloys VF607, AF584C, AF588C and VF609, including the magnetic hyperfine profiles for the α–FeV solid solution and Fe_3C phases.

By comparing the α–FeV magnetic hyperfine distributions (MHD) for Alloys VF609, AF584C and AF588C (see **Figure 4.4**), it appears that in Alloy VF609 the majority of the Fe atoms had three V neighbours (27 T), while in the other alloys the majority of the Fe atoms had no V neighbours. This agrees with the higher V content of α–FeV in Alloy VF609 predicted by stoichiometric calculations (see **Table 4.9**). The α–FeV magnetic field distributions were compared with the simulated distributions and good agreement was found.

The MHD profiles of the Fe_XC_Y phase consisted of almost discrete peaks (see **Figure 4.4**). The highest peaks were in the 22 to 24 T region in Alloys AF584C and AF585C (at 80K) which were expected to contain Fe_3C and in which Fe_3C had been confirmed by X–ray diffraction. Many peaks coincided with the peaks reported by Matteazzi et al[31], which were attributed to Fe_XC_Y carbides of various stoichiometries. Some of the peaks are still unidentified. From the work it was deduced that Fe_3C was present although the presence of other peaks indicate that small amounts of other phases were also present. Good agreement was found with the stoichiometric calculations in **Table 4.9**.

In the case of Alloy VF609, the second component (at 80K) was not Fe_3C (as confirmed by X–ray diffraction) but it appears to correspond to a quadropole doublet. The origin of this component may be superparamagnetism. The room temperature spectra of Alloys AF584C and AF588C present, besides the two components already described, a third component which is also a strong central quadropole doublet around zero velocity. Since the absorbtion lines disappear at 80K, they may be due to very small particles (less then 30nm in diameter) in which the magnetic moments cannot be aligned, leading therefore to superparamagnetism. In the case of Alloy VF609, the quadropole doublet is present at both 80 and 300K, which suggested the presence of particles even smaller than ~25nm.

Table 4.9. – Comparison of matrix and α–FeV compositions obtained by stoichiometric calculations and Mössbauer measurements

Alloy	Matrix composition from MS[i] Fe_3C mol%/ α–Fe mol%	Calculated matrix composition Fe_3C mol%/ α–Fe mol%	α–Phase composition from MS[i] Fe mol%/ V mol%	Calculated α–phase composition Fe mol%/ V mol%
VF576	44/56	46/54	9.4/0.6	10/0
681C	16/84	0/100	6/4	8/2
VF607	7/93	0/100	9/1	9.7/0.3
VF609	27/73[ii]	0/100	6/4	7/3
AF583C	36/64	26/74	9.9/0.1	10/0
AF584C	38/62	39/61	9.97/0.03	10/0
AF585C	30/70	29/71	9.5/0.5	10/0
AF588C	55/45	60/40	8.9/1.1	10/0
AF589C	48/52	59/41	9.6/0.4	10/0

(i) MS = Mössbauer Spectroscopy

(ii) This value was obtained assuming that the additional phase that appeared to be present was Fe_3C.

4.5. Metallography

Most of the alloys showed phases which agreed with the phase diagram. The non equilibrium cooling resulted in the shifting of the composition boundaries so that the Fe_3C and graphite phases appeared at lower C contents than predicted. These are described later in this section.

Overlaps between Phase 2 and 3 alloys lead to all the alloys being classified according to the microstructure. Phase 1 alloys had α as the primary phase. Most of Phase 2 alloys and all of Phase 3 alloys had VC_{1-x} as the primary phase. VC only formed in Phase 1 alloys by one of the transformation reactions. The resultant carbide particles in Phase 1 alloys were therefore small. The solidification of Phase 1 alloys is described in groups 1 to 3 with the remainder of the groups containing Phase 2 and 3 alloys.

Group 1 contained Alloys VC2, VC5 and VC8. All these alloys showed α and VC_{1-x} at room temperature. Solidification started with primary ferrite dendrites and ended with a eutectic reaction to form α and VC_{1-x} in the interdendritic regions. Further cooling caused a secondary finer precipitation of VC_{1-x} in the α dendrites (see **Figures 4.5** to **4.7**).

Figure 4.5. – Alloy VC2 – Dendrites of *α* in a matrix of eutectic *α* and VC_{1-x}.
Etched 2% Nital, 500X

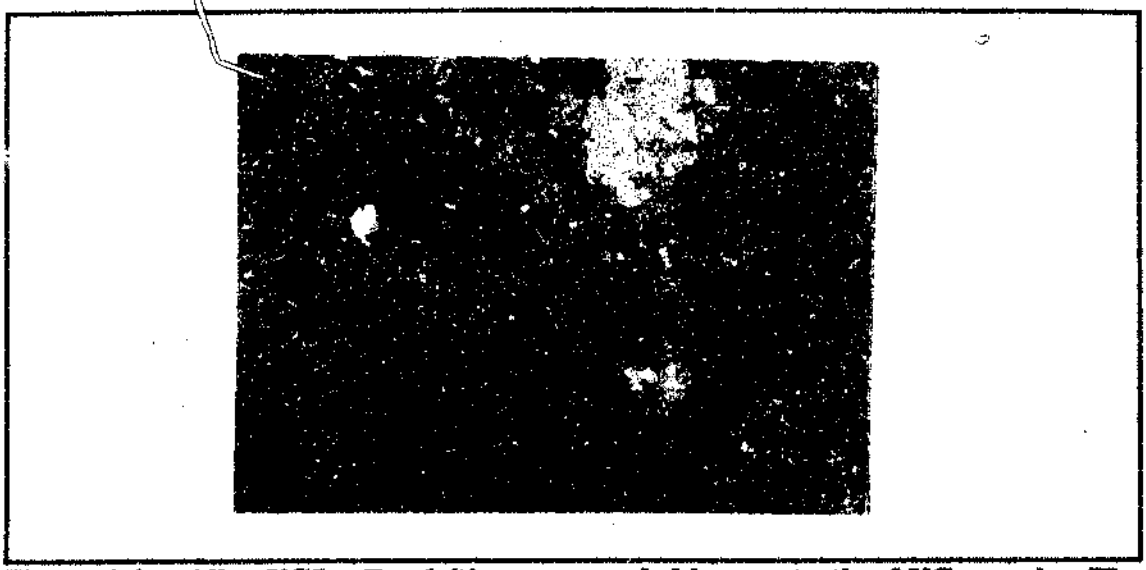

Figure 4.6. – Alloy VC5 – Dendritic α surrounded by a eutectic of VC_{1-x} and α. The dendritic α shows small, darker precipitate particles probably of VC_{1-x}.
Etched 2% Nital, 500X

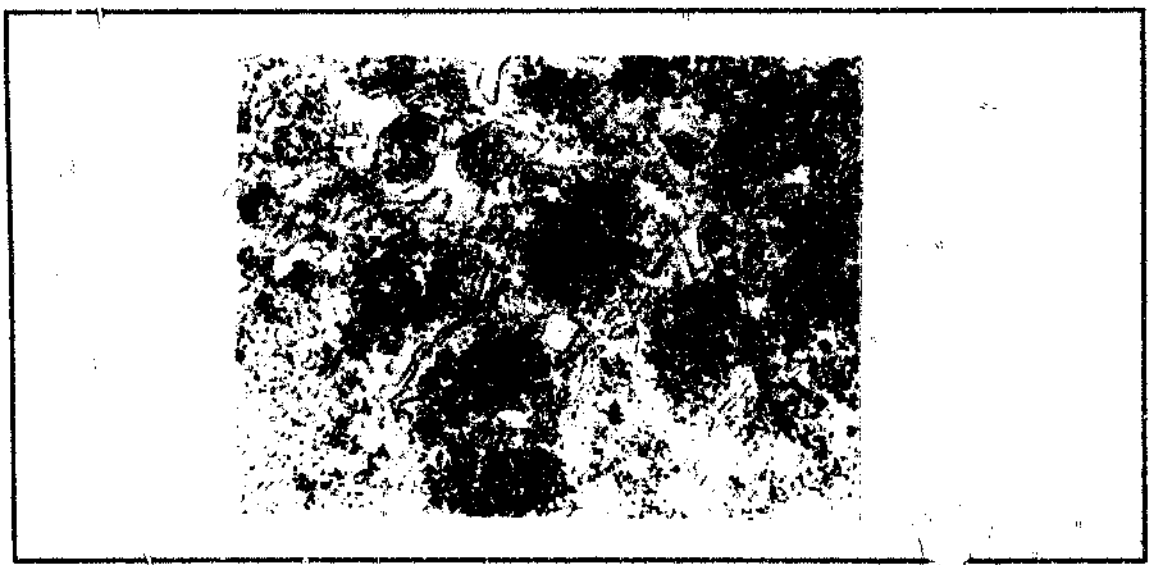

Figure 4.7. – Alloy VC8 – α surrounded by a eutectic of VC_{1-x} and α. The α shows precipitate particles of VC_{1-x}.
Etched 2% Nital, 500X

Group 2 consists of Alloys VC3, VC6 and VC7. These alloys contained primary α with a eutectic of VC_{1-x} and α. Cooling predicted a peritectoid reaction in which VC_{1-x} and some α were consumed to form V_2C. The microstructures of these alloys are seen in **Figure 4.8**

The last group of Phase 1 alloys consists only of Alloy VC4. After the primary α, a small

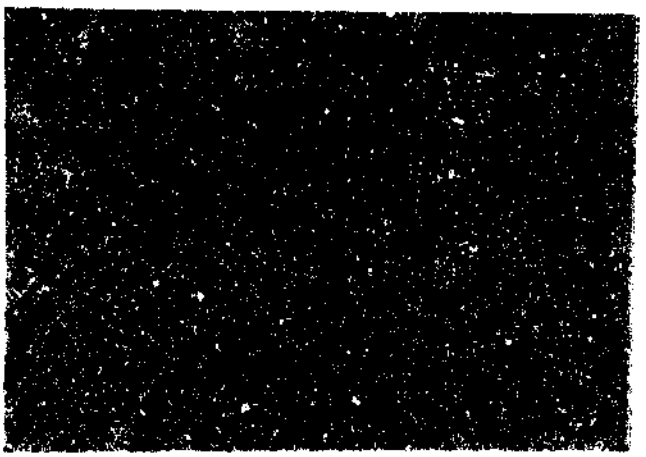

Figure 4.8. – Alloy VC3 – Dendritic α surrounded by eutectic VC_{1-X} and α. A few V_2C particles appear to be present in the α.
Etched 2% Nital, 500X

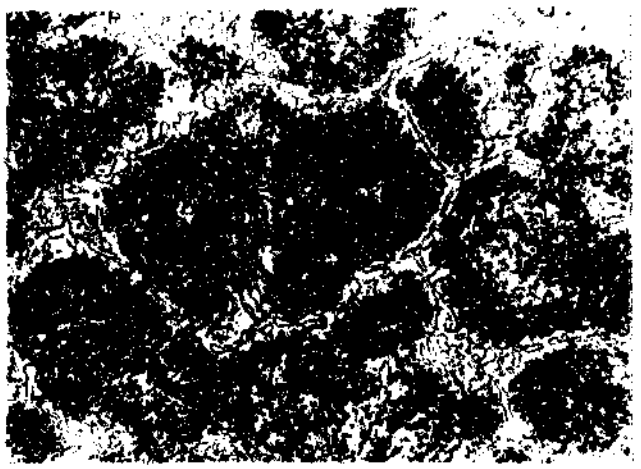

Figure 4.9. – Alloy VC6 – Dendritic α surrounded by eutectic VC_{1-X} and α. Few secondary V_2C particles are also present.
Etched 2% Nital, 500X

amount of eutectic VC_{1-X} and α was formed. Further cooling resulted in the ternary η being formed in a peritectoid reaction. The morphology of the carbide tends to be more rod-like in contrast with previous carbides seen. Figure 4.11 shows the microstructure of this alloy.

Group 4 contained the Phase 2 and 3 Alloys VF576, AF583A, AF583C, AF584A, AF584C,

Figure 4.10. – Alloy VC7 – Dendritic α surrounded by eutectic VC_{1-X} and α. Few secondary V_2C particles are present due to the incomplete peritectoid reaction.
Etched 2% Nital, 500X

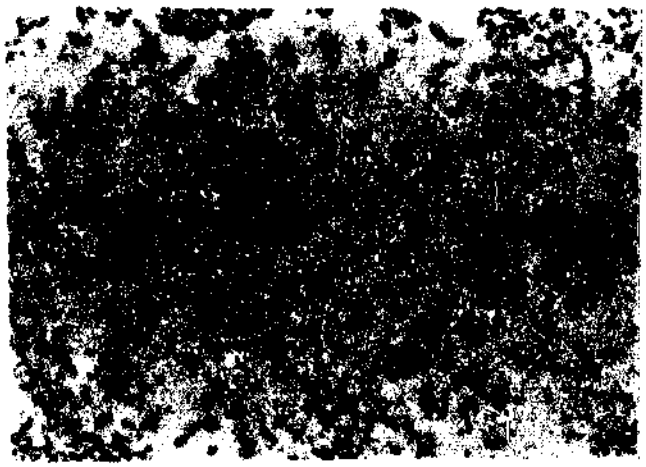

Figure 4.11. – Alloy VC4 – Eutectic α and VC_{1-X} with some V_2C
Etched 2% Nital, 500X

AF585A, AF585C and AF587C. Solidification started with dendritic VC_{1-X}. This continued until the eutectic composition was reached when γ and VC1–X precipitated. These are the phases present on the 1100°C isotherm of the Fe–V–C phase diagram. Further cooling resulted in the γ undergoing the eutectoid reaction forming pearlite (α and Fe_3C). The alloys are shown in **Figures 4.12** to **4.19.**

Group 5 contains Alloys AF588A, AF588C, AF589A and AF589C. Solidification starts with

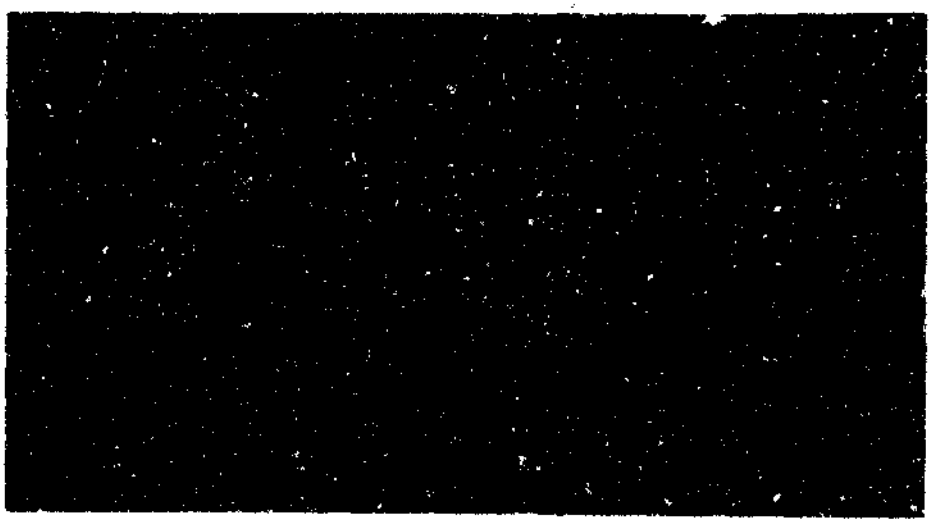

Figure 4.12. – Alloy VF576 – Dendrites of VC_{1-x} in pearlite and cementite.
Etched in 2% nital followed by 30seconds etch at 1.5V in lead acetate, 1000X

Figure 4.13. – Alloy AF583A – Spheroidal VC_{1-x} in pearlite.
Etched in 2% nital followed by 30seconds etch at 1.5V in lead acetate, 400X

the precipitation of VC_{1-x}. This is then followed by the coarse eutectic of Fe_3C and γ. The remaining liquid then probably undergoes a ternary eutectic reaction to form ledeburite (Fe_3C and γ). Further cooling results in the γ undergoing the eutectoid reaction to form pearlite. For Alloys AF589A and AF589C, the non equilibrium cooling moved the composition into the free graphite region causing the precipitation of graphite. These alloys are shown in **Figure 4.20** to **4.23**.

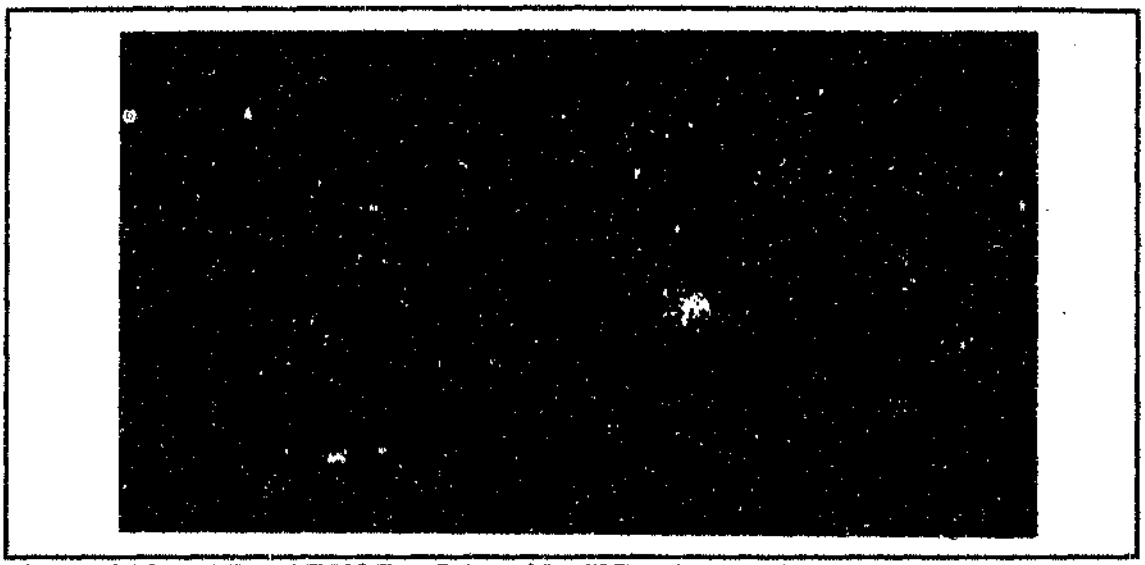

Figure 4.14. – Alloy AF583C – Spheroidal VC_{1-x} in pearlite.
Etched in 2% nital followed by 30seconds etch at 1.5V in lead acetate, 400X

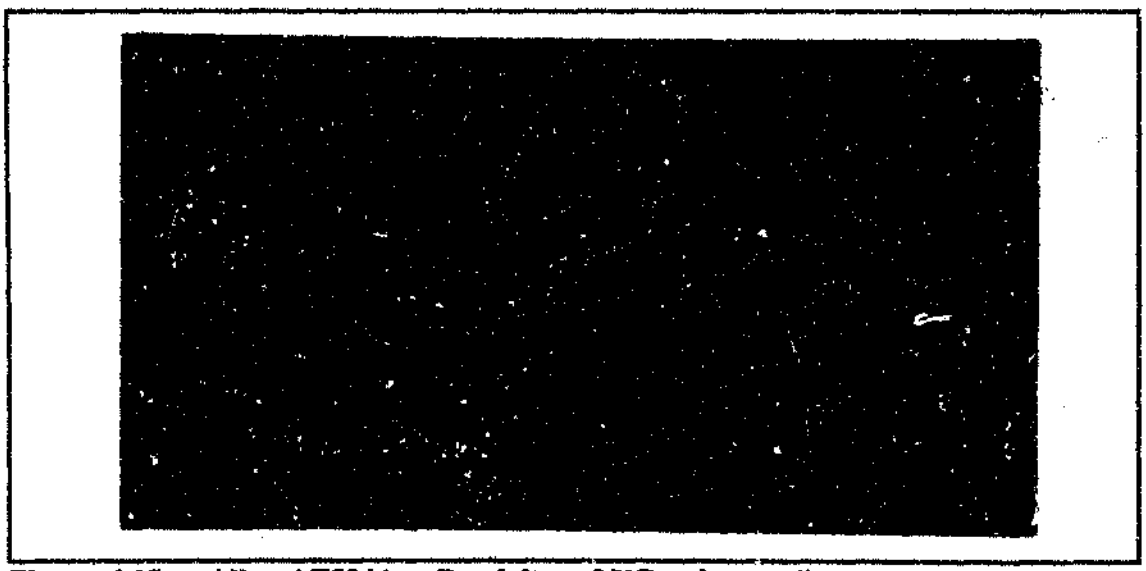

Figure 4.15. – Alloy AF534A – Dendrites of VC_{1-x} in pearlite.
Etched in 2% nital followed by 30seconds etch at 1.5V in lead acetate, 400X

The next group of alloys contain Alloys VF607, VF609, 681A and 681C. These alloys all formed primary dendritic VC_{1-x}. The remaining liquid underwent a eutectic reaction forming VC_{1-x} and α. These alloys are shown in **Figure 4.24** to **4.27**.

The remaining four alloys fall into a separate category. These alloys showed inferior microstructures. The surfaces of these alloys were extremely difficult to prepare as material would detach from the bulk sample during polishing. The most successfully prepared samples

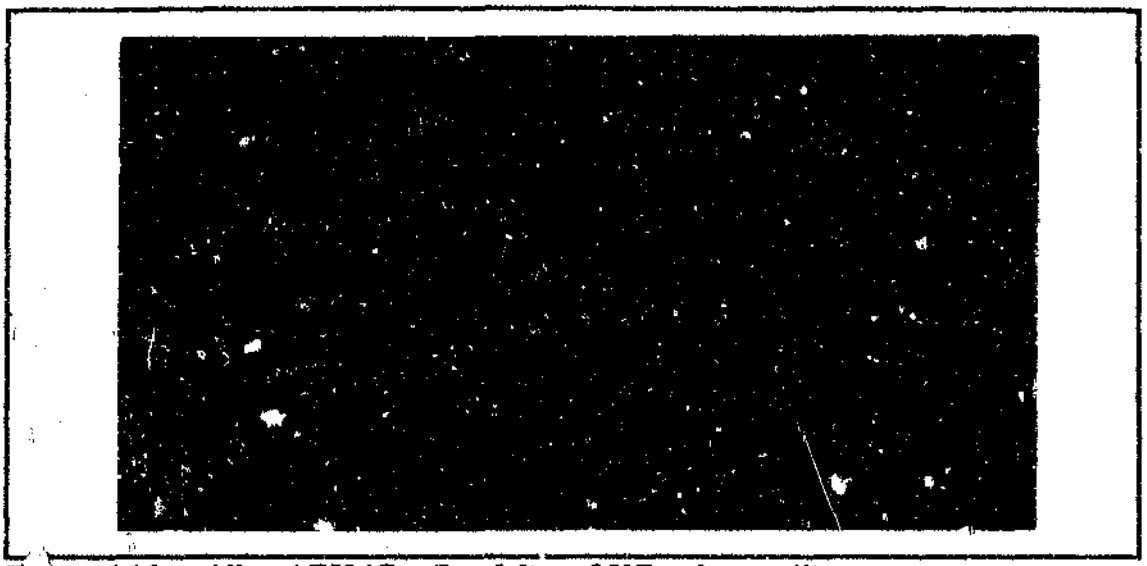

Figure 4.16. – Alloy AF584C – Dendrites of VC_{1-x} in pearlite.
Etched in 2% nital followed by 30seconds etch at 1.5V in lead acetate, 400X

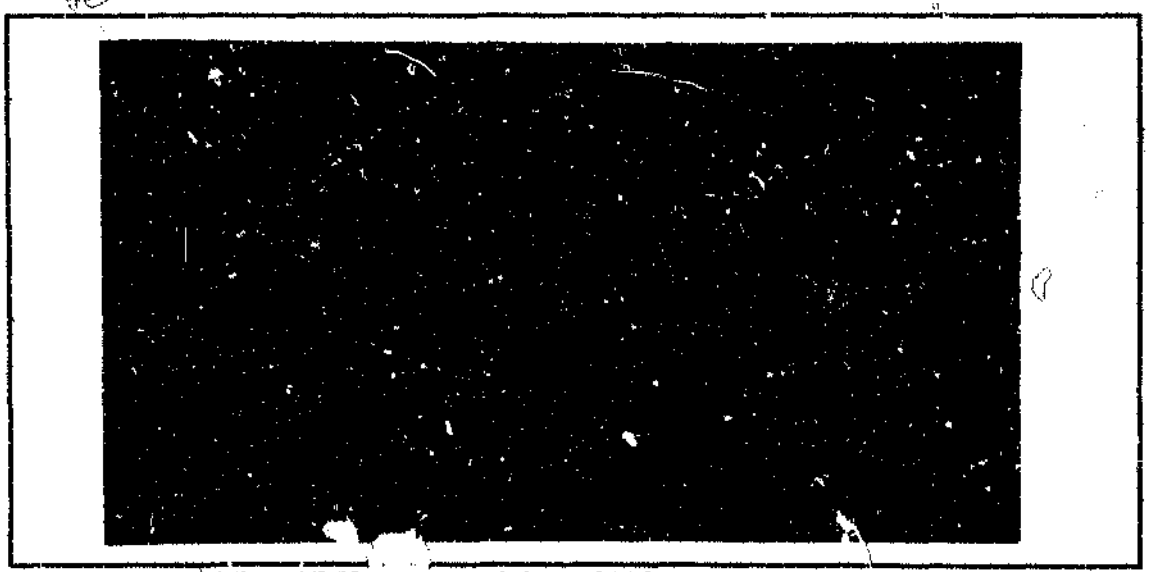

Figure 4.17. – Alloy AF58[illegible] – Dendrites of VC_{1-x} in pearlite.
Etched in 2% nital followed by 30seconds etch at 1.5V in lead acetate, 400X

are shown here. They still show cracking and areas in which some phases have spalled. From the 500°C isotherm of the Fe–V–C phase diagram the alloys are supposed to contain the phases as follows:

Alloy VF577 σ, η and V_2C.

Alloy VF578 σ and V_2C.

Alloy VF579 α and η.

Alloy AF586A η and V_2C.

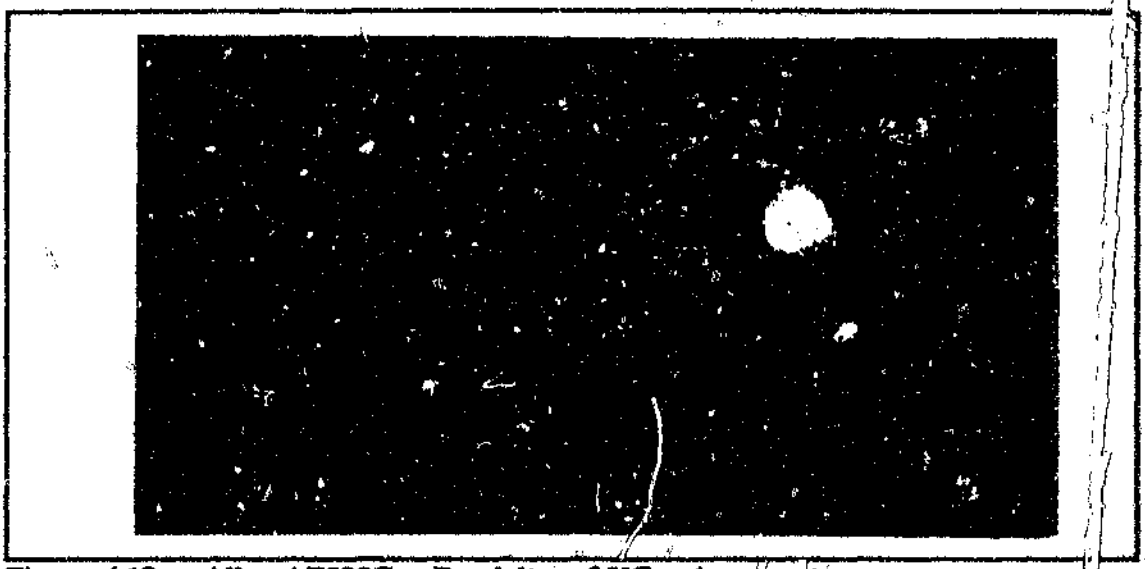

Figure 4.18. – Alloy AF585C – Dendrites of VC_{1-x} in pearlite.
Etched in 2% nital followed by 30seconds etch at 1.5V in lead acetate, 400X

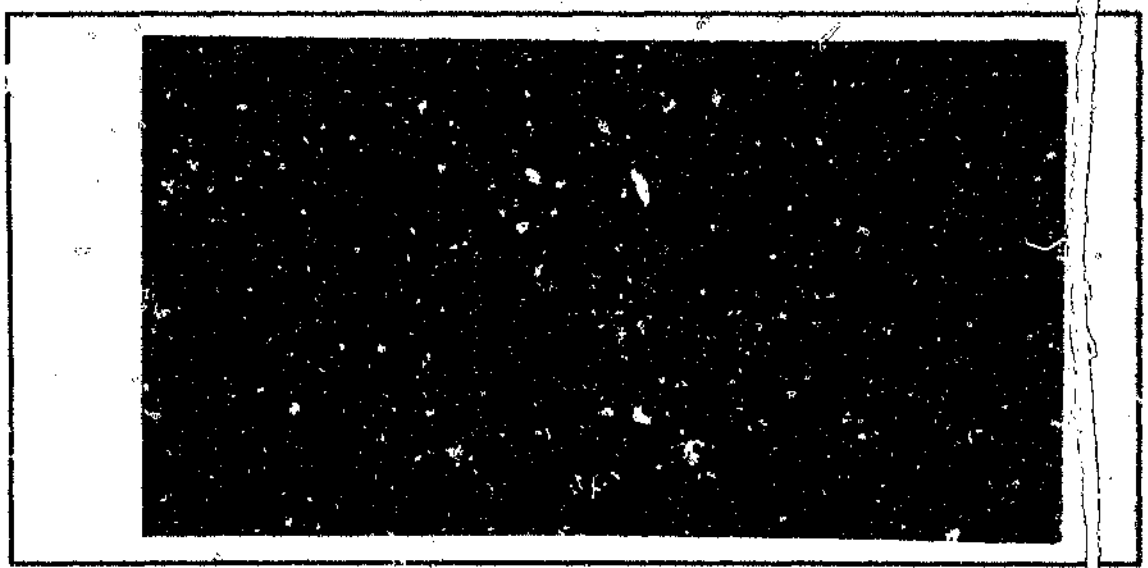

Figure 4.19. – Alloy AF587C – Dendrites of VC_{1-x} in pearlite.
Etched in 2% nital followed by 30seconds etch at 1.5V in lead acetate, 400X

These alloys are shown in **Figure 4.28** to **4.31**.

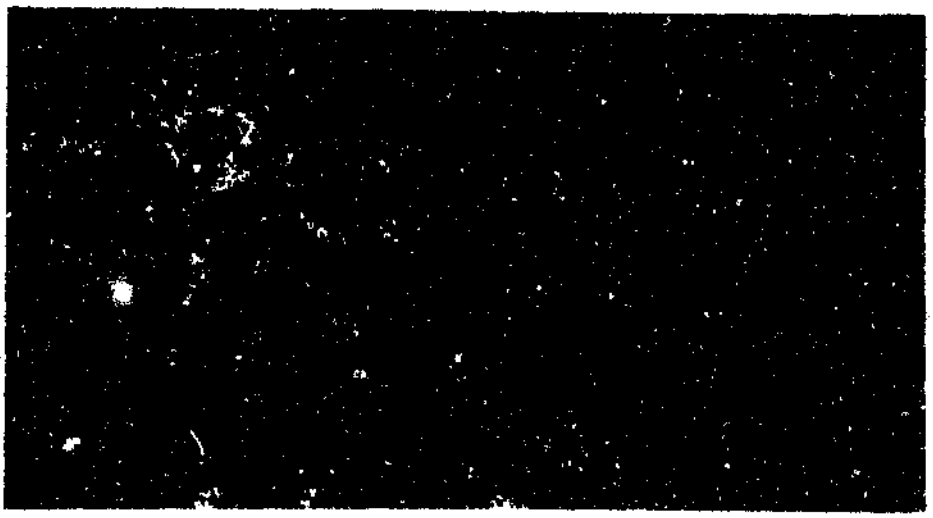

Figure 4.20. – Alloy AF588A – Dendritic VC_{1-x} in a matrix of ledeburite and pearlite. Etched in 2% nital, followed by 30seconds at 1.5V in lead acetate, 400X

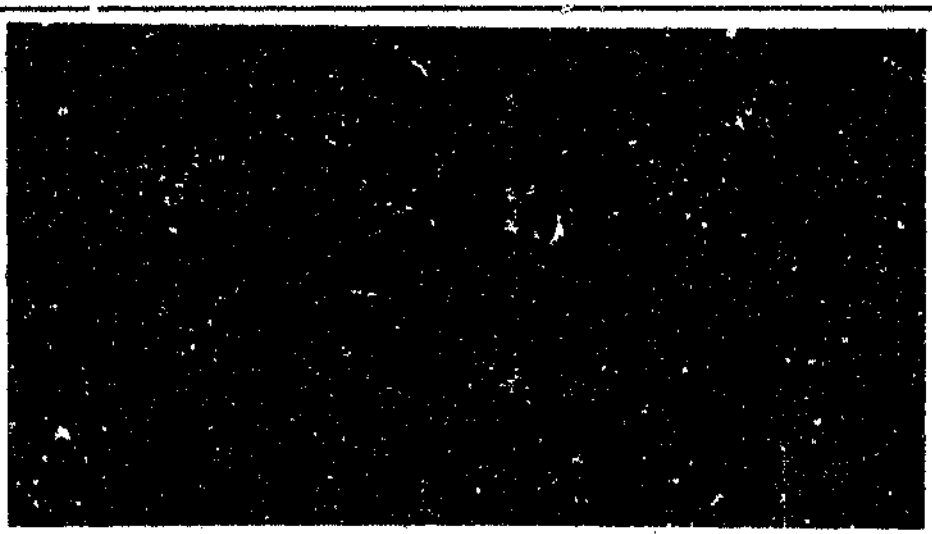

Figure 4.21. – Alloy AF588C – Dendritic VC_{1-x} in a matrix of ledeburite and pearlite. Etched in 2% nital, followed by 30seconds at 1.5V in lead acetate, 400X

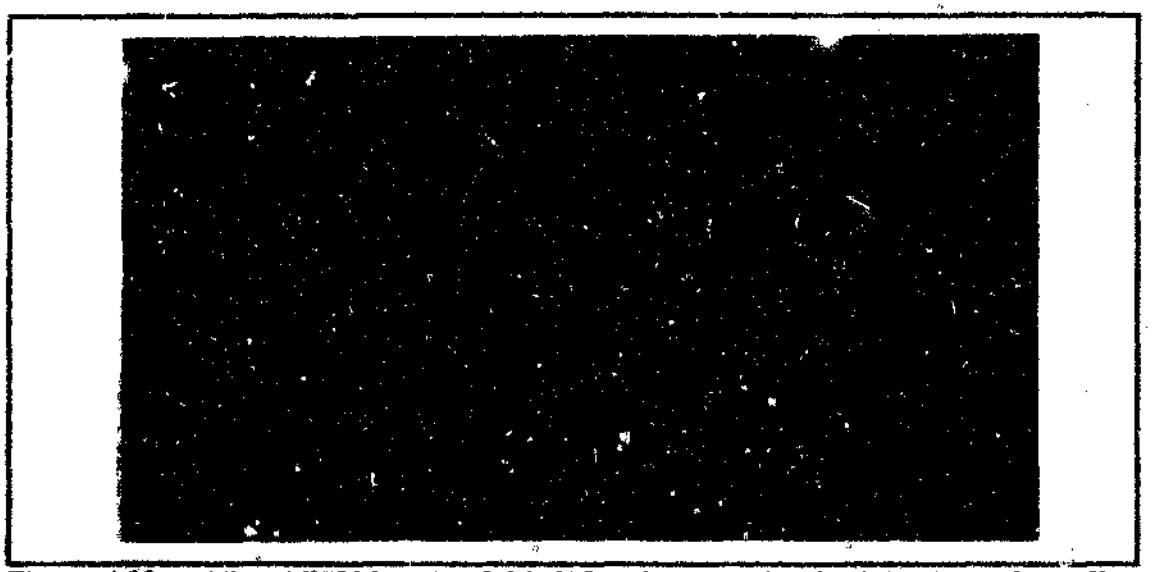

Figure 4.22. – Alloy AF589A – Dendritic VC_{1-x} in a matrix of ledeburite and pearlite. Free graphite appears in an unusual ring form.
Etched in 2% nital, followed by 30seconds at 1.5V in lead acetate, 400X

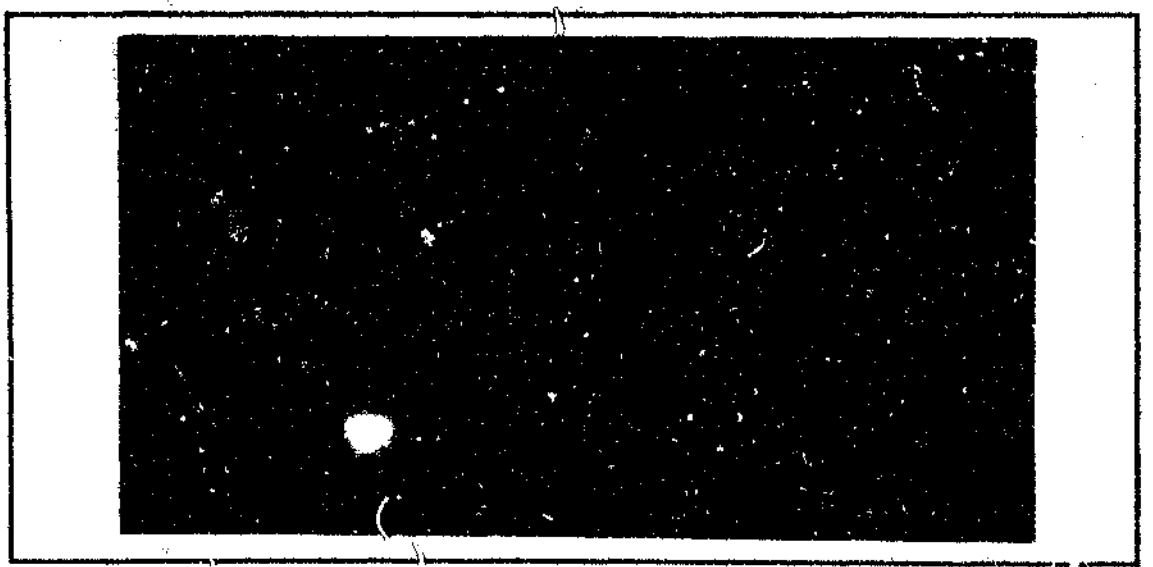

Figure 4.23. – Alloy AF589C – Dendritic VC_{1-x} in a matrix of ledeburite and pearlite. Free graphite also present.
Etched in 2% nital, followed by 30seconds at 1.5V in lead acetate, 400X

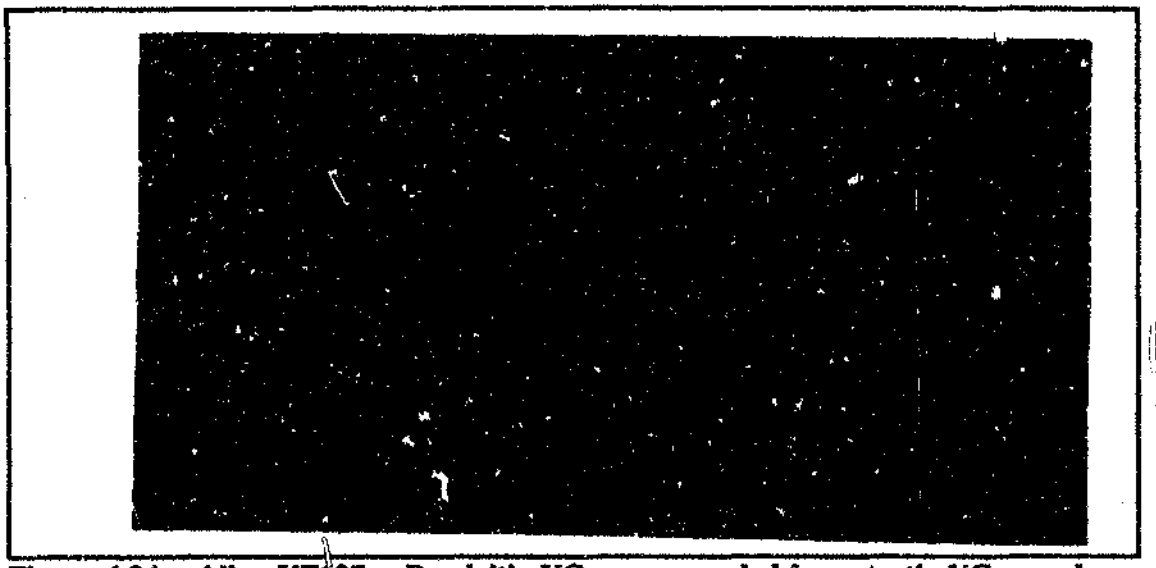

Figure 4.24 – Alloy VF607 – Dendritic VC_{1-X} surrounded by eutectic VC_{1-X} and α
Etched in 2% nital followed by 30 seconds at 1.5V in lead acetate, 400X

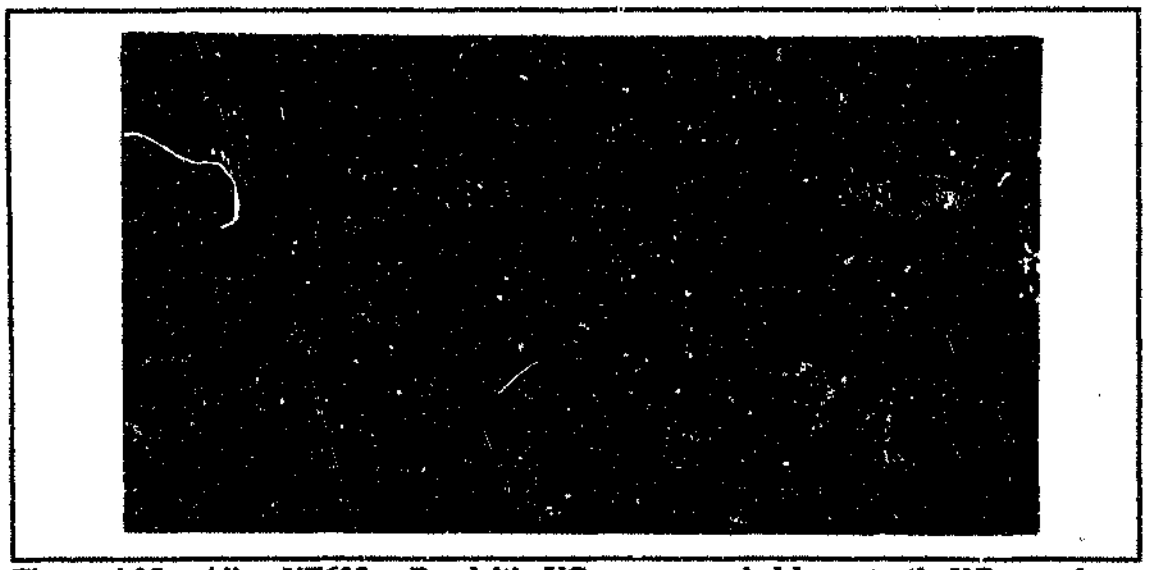

Figure 4.25 – Alloy VF609 – Dendritic VC_{1-X} surrounded by eutectic VC_{1-X} and α
Etched in 2% nital followed by 30 seconds at 1.5V in lead acetate, 400X

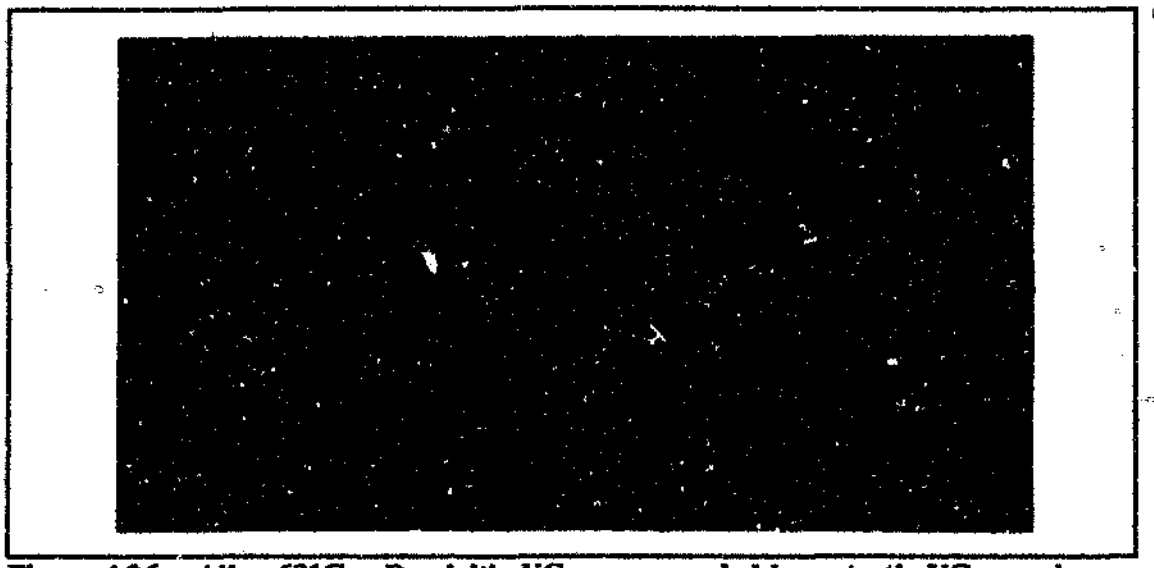

Figure 4.26 – Alloy 681C – Dendritic VC_{1-x} surrounded by eutectic VC_{1-x} and α
Etched in 2% nital followed by 30 seconds at 1.5V in lead acetate, 400X

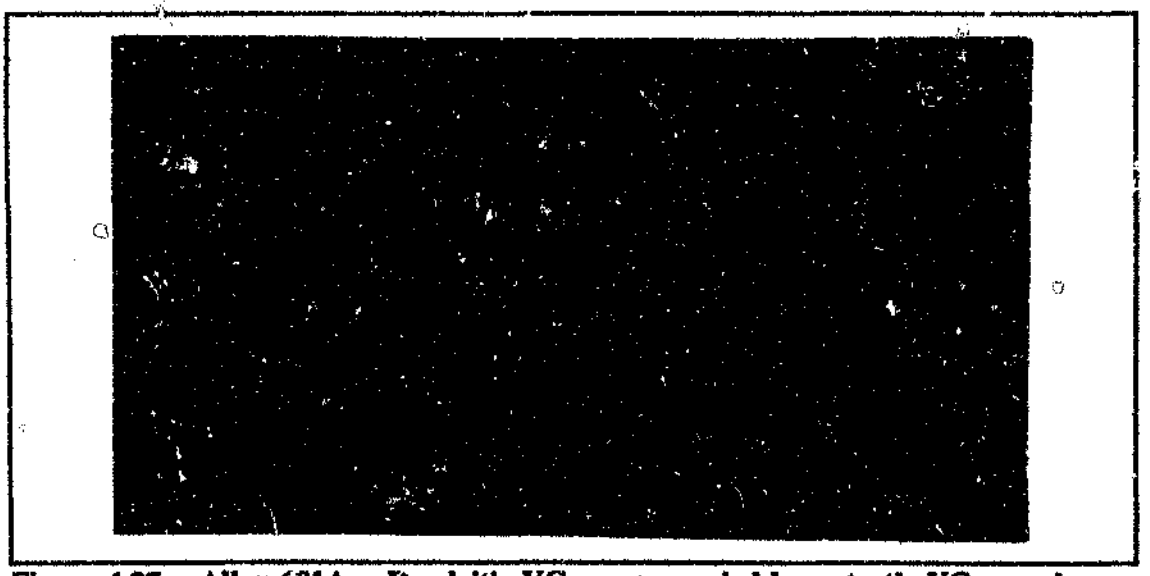

Figure 4.27 – Alloy 681A – Dendritic VC_{1-x} surrounded by eutectic VC_{1-x} and α
Etched in 2% nital followed by 30 seconds at 1.5V in lead acetate, 400X

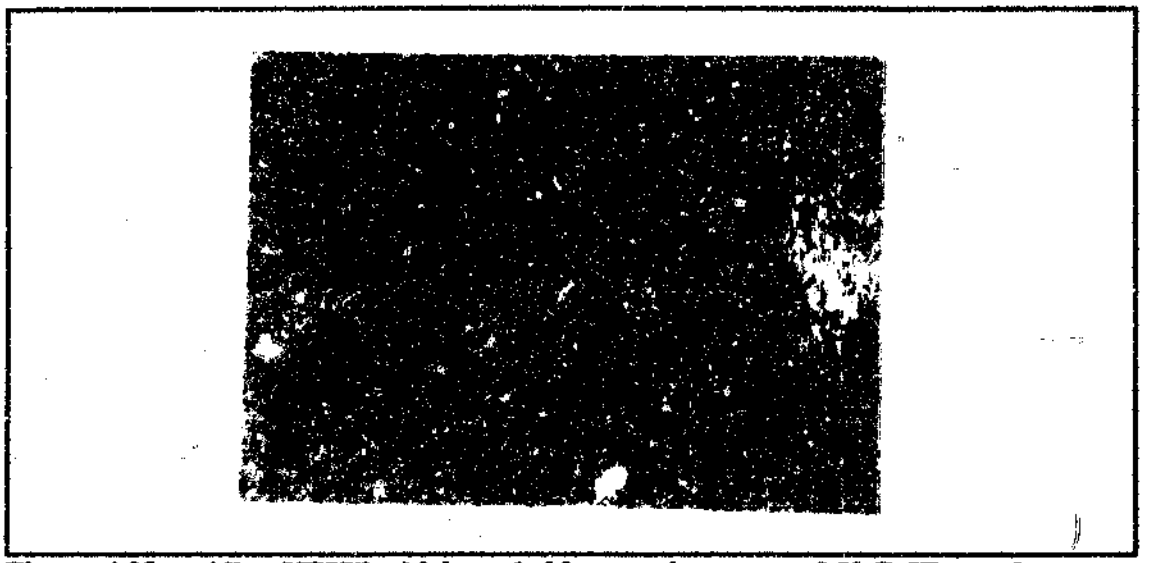

Figure 4.28. – Alloy VF577 which probably contains σ, η and V_2C. These phases are predicted on the 500°C isotherm of Fe–V–C equilibrium phase diagram.
Etched in 2% nital, 500X.

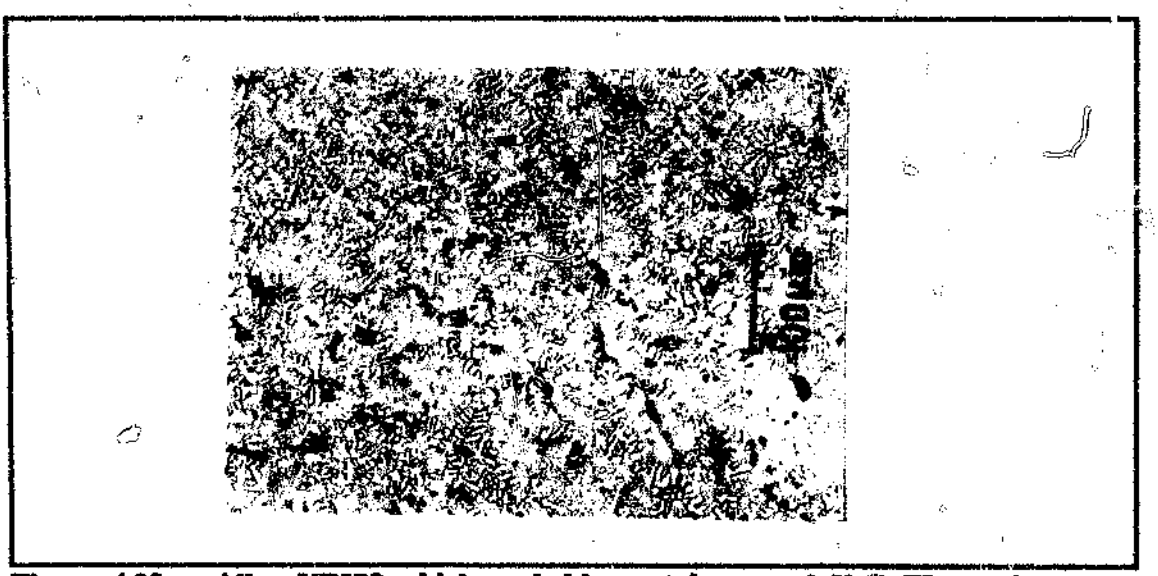

Figure 4.29. – Alloy VF578 which probably contains σ and V_2C. These phases are predicted on the 500°C isotherm of Fe–V–C equilibrium phase diagram.
Etched in 2% nital, 100X.

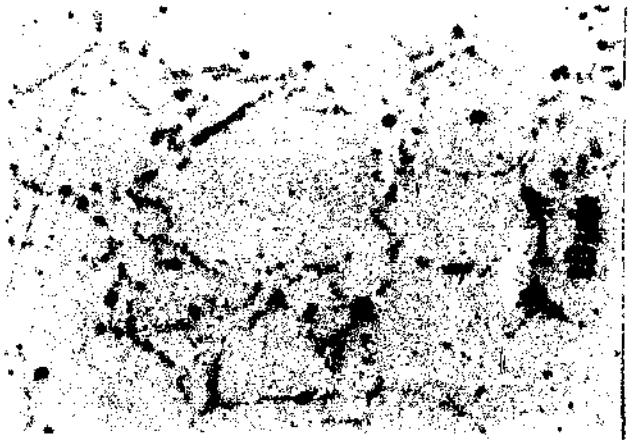

Figure 4.30. – Alloy VF579 which probably contains α and η. These phases are predicted on the 500°C isotherm of Fe–V–C equilibrium phase diagram.
Etched in 2% nital, 100X.

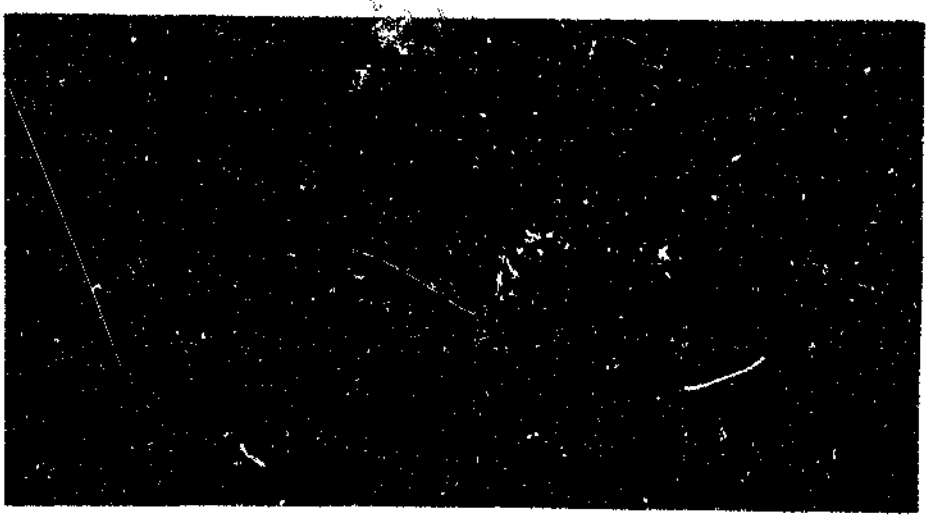

Figure 4.31. – Alloy AF586A which is predicted to contain σ, η and V_4C.
Etched in 2% nital followed by 10s at 1.5V in lead acetate, 400X.

4.6. Image analysis results

A significant scatter in results was noted between different fields of view. A measure of this scatter is given by the standard deviation. The results were obtained using two different techniques. Those obtained from the Ibas I and II machine are given in **Table 4.10.** The results obtained by manual counting on the microscope are given in **Table 4.11.**

It was noted that in general the VC particle size increased with C content. This is shown in **Figure 4.32.**

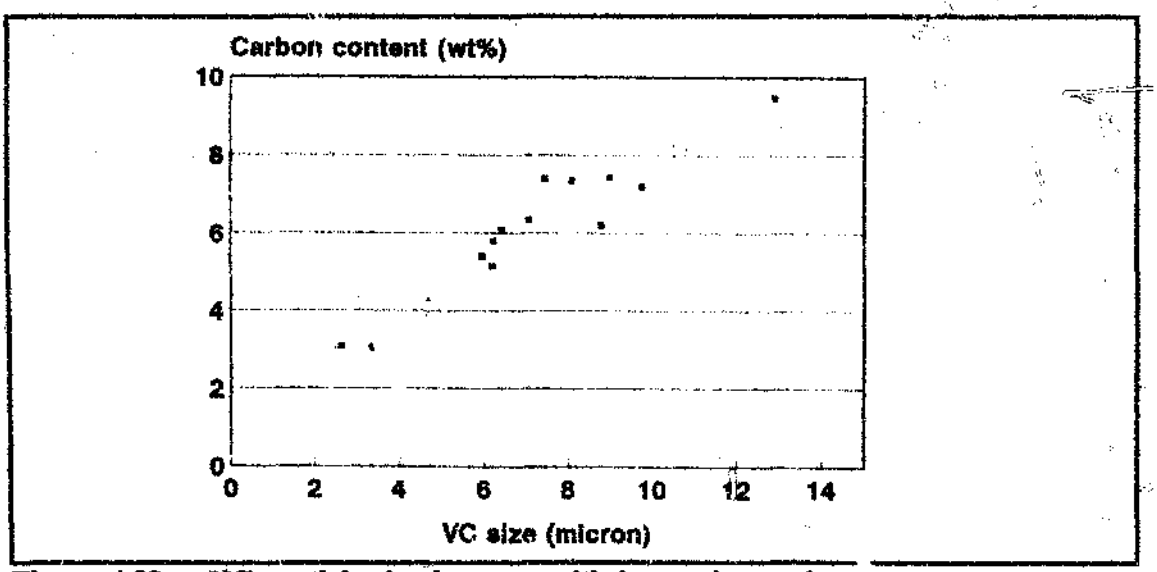

Figure 4.32. – VC particle size increases with increasing carbon content.

4.7. SEM results from metallography and worn surfaces

Polished and worn samples were examined using a SEM. Dot mapping was used to identify areas containing V and those containing Fe. The analyses revealed the low Fe content of the VC particles. A split, backscattered image and Fe window dot map are shown in

Table 4.10. – Image analysis results giving the VC volume %, size and average distance (mean free path) between VC particles

Alloy	VC Vol%	Std dev.	Mean VC Size[i] (µm)	Std dev.	MFP[ii] (µm)	Std dev.	Max VC size (µm)
VF576	36.0	2.4	6.2	4.4	10.7	11.1	42.75[iii]
VF607	49.2	2.2	4.7	4.7	4.9	4.2	48.75
VF609	71.9	12.5	12.9	14.5	5.0	5.0	145.5
681C	60.9	5.6	7.4	7.4	4.9	4.6	70.50
AF583C	7.2	1.3	3.3	2.2	37.1	42.8	17.25
AF584C	30.2	2.4	6.2	5.2	13.9	17.3	58.50
AF585C	35.6	5.3	8.8	9.3	15.4	19.1	75.75
AF588C	37.7	4.5	7.1	6.8	11.5	14.0	72.75
AF589C	32.5	2.8	9.0	7.1	18.2	22.0	87.00
AF583A	7.4	1.1	2.6	1.6	28.8	31.3	12.00
AF584A	29.3	1.6	6.0	4.6	13.9	13.8	41.25
AF585A	40.3	4.2	9.7	5.8	14.3	14.9	80.25
AF588A	30.9	2.7	6.4	5.1	13.8	16.3	51.75
AF589A	29.5	3.4	8.1	7.5	18.5	20.8	102.00

(i) VC size determined by a series of straight lines which intercept VC particles only in one direction. This corresponds to the apparent VC particle size as seen by the abrasive particle when moving across the alloys.

(ii) The mean free path was measured as the distance between carbide particles of the primary and eutectic form and not only between primary carbides particles.

(iii) This value was lower than expected (see Section 5.7).

Table 4.11. – Image analysis results showing the volume % of pearlite, cementite and ferrite.

Alloy	Pearlite Vol%	Std dev	Cementite Vol%	Ferrite Vol%
VF576	42.5	12.1	21.5	0.0
VF607	0.0	0.0	0.0	50.8
VF609	0.0	0.0	0.0	28.1
681C	0.0	0.0	0.0	39.1
AF583C	92.8		0.0	0.0
AF584C	56.1	13.4	13.7	0.0
AF585C	51.3	13.9	13.5	0.0
AF588C	33.9	13.4	28.4	0.0
AF589C(i)	22.3	8.5	40.7	0.0
AF583A	89.6	7.2	3.0	0.0
AF584A	62.1	11.7	8.6	0.0
AF585A	54.0	13.6	5.7	0.0
AF588A	31.6	10.4	37.5	0.0
AF589A(ii)	12.4	8.7	52.2	0.0

(i) 4.5 vol% graphite

(ii) 5.9 vol% graphite

Figure 4.33. **Figure 4.34** shows the same image using a V window dot map. This technique identified the dendritic phase in Phase 2 and 3 alloys as being VC. Semi-quantitative spot EDS analyses showed VC particles to contain less than 1.9wt% Fe[26]. EDS analyses in **Figures 4.35** to **4.37** show typical spectra of the VC, α and Fe_3C phases respectively. **Figure 4.38** shows how backscattered imaging highlighted the different phases on the worn surfaces.

The globules lying within the Fe_3C phase in Alloy VF576 were identified as pearlite in **Figure 4.39.** The hardness tests done on Alloy VF576 (**Figure 4.40**) revealed cracking in the

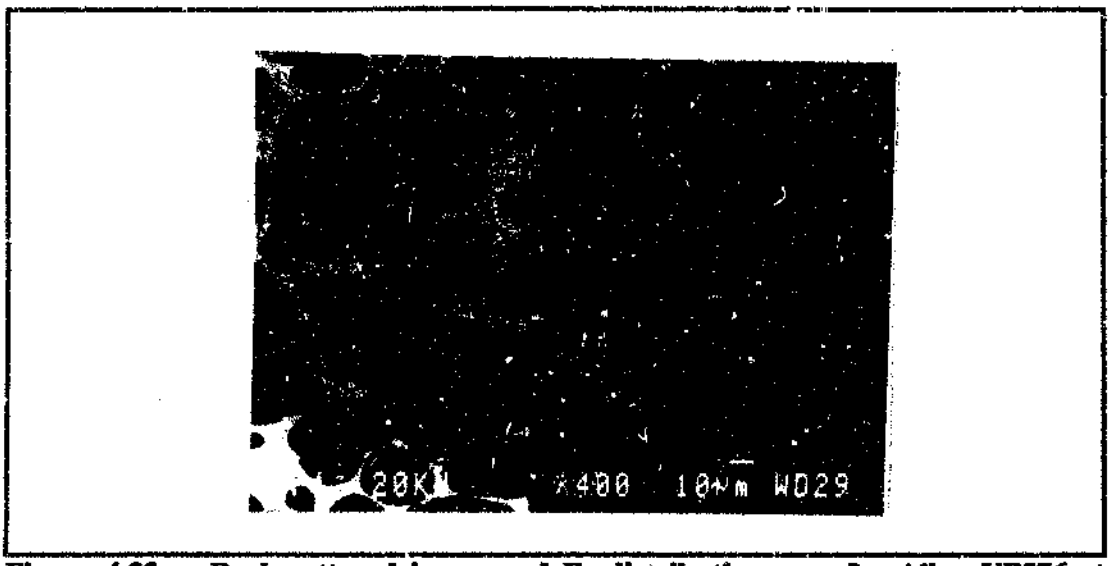

Figure 4.33. – Backscattered image and Fe distribution map for Alloy VF576 at 800X.

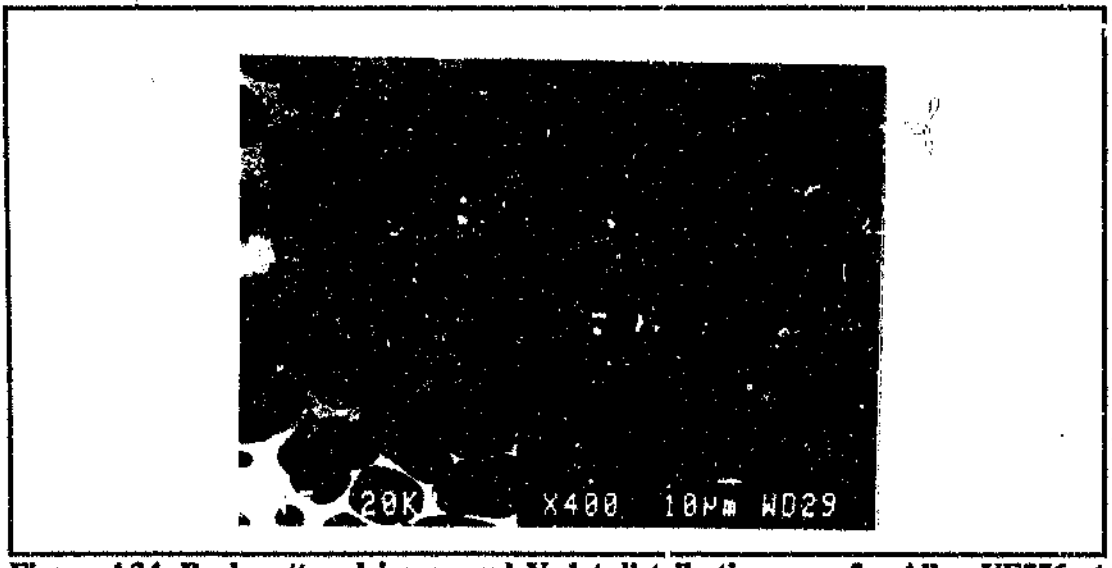

Figure 4.34. Backscattered image and V dot distribution map for Alloy VF576 at 800X.

long dendritic VC particles in the plastically deformed region surrounding the hardness indentations. These cracks are thought to result in accelerated wear occurring in alloys containing long dendrites during 3–body abrasion testing(**Figure 4.41**). In this figure the dendritic VC particle can be seen to have been removed preferentially. Examination of alloys tested under 3–body abrasion conditions, showed multi–directional wear grooves (**Figure 4.42**). These were not found using the 2–body and modified 3–body abrasive wear apparatus. Cracks in Alloy VF609 proved to be a areas of accelerated wear as seen in **Figure 4.43.**

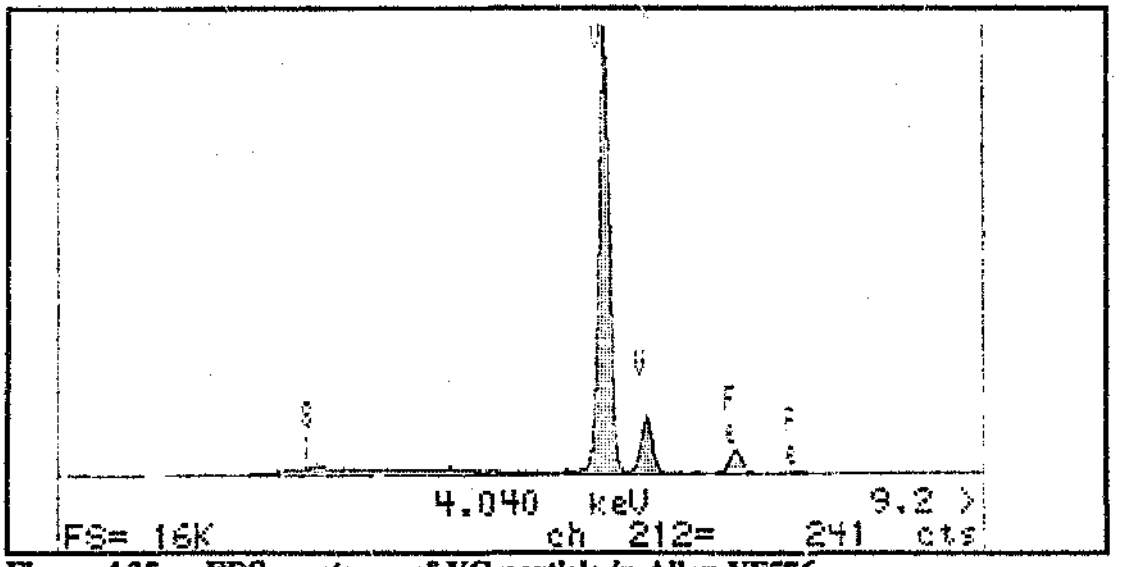

Figure 4.35. – EDS spectrum of VC particle in Alloy VF576.

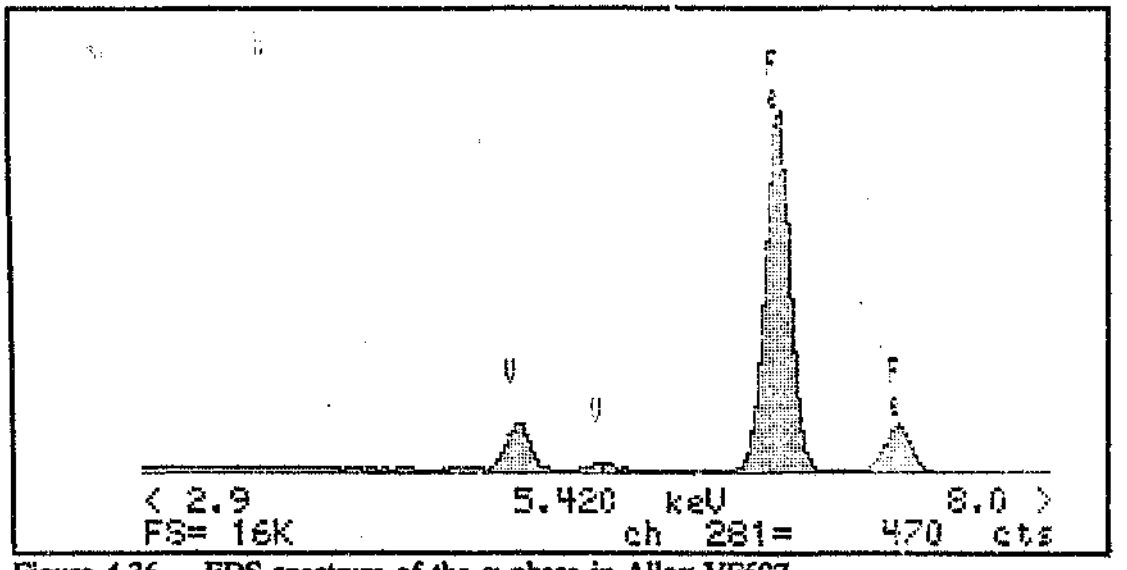

Figure 4.36. – EDS spectrum of the α phase in Alloy VF607.

These cracks caused deep grooves to form on the surface of the alloys by acting as weak points for preferential attack of the alloys. The cracks were most probably caused by thermal residual stresses in the material resulting from the differences in coefficient of expansion of the phases[31]. **Figure 4.44** shows a crack propagating from the matrix into a VC particle.

The effect on VC particles of abrasive wear was found to be a function of the carbide particle size. The wear grooves on mild steel are straight with little interruption along the length of the groove (**Figure 4.45**). Small VC particles affect the passage of abrasive particles only slightly (**Figure 4.46**). The intermediate sized VC particles are seen to break up by a brittle

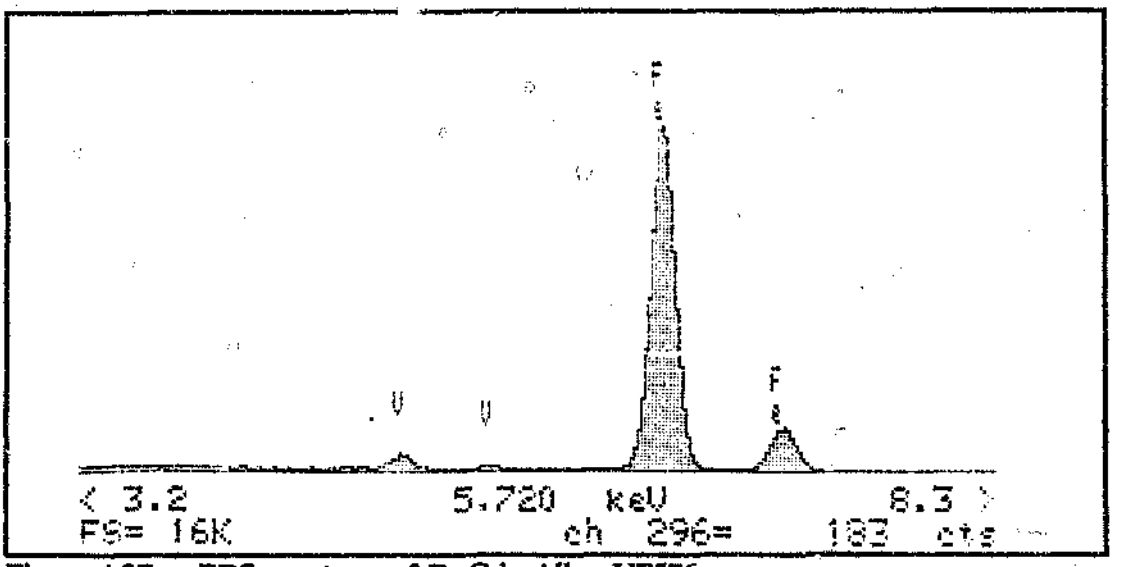

Figure 4.37. – EDS spectrum of Fe_3C in Alloy VF576.

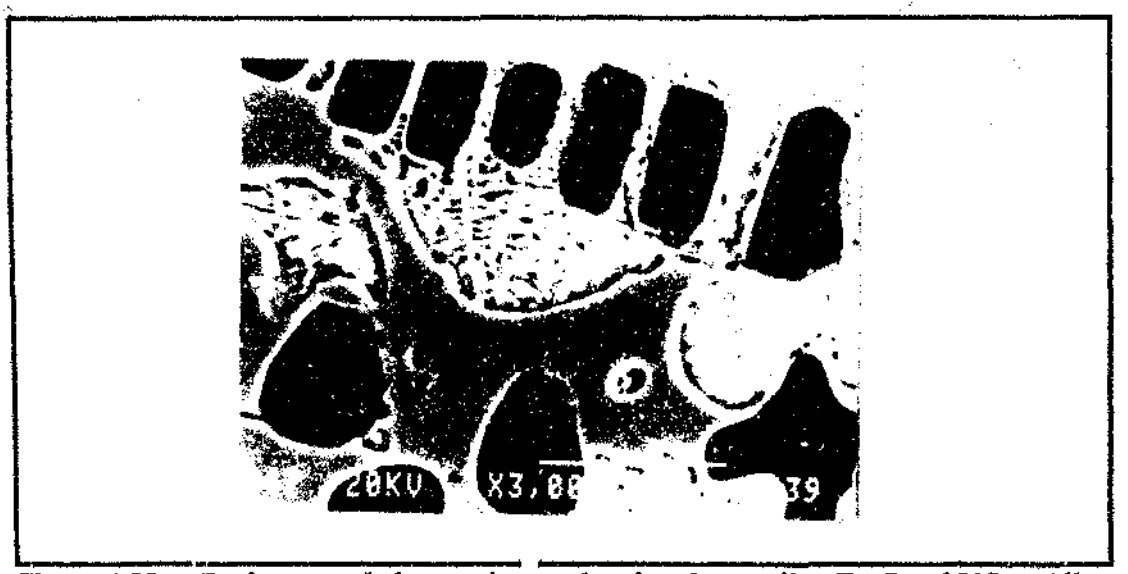

Figure 4.38. – Backscattered electron image showing the pearlite, Fe_3C and VC in Alloy VF576.

fracture mechanism and are not very effective in preventing the passage of abrasive particles (**Figure 4.47**). The large VC particles prevented the passage of abrasive particles through the alloy surface and tended to break up to a lesser degree (see **Figure 4.48**). A comparison of the size effect is seen in a heterogeneous region of Alloy VF609 in **Figure 4.49**. Large VC particles which are not fully spheroidal showed a greater tendency to break up by brittle fracture (**Figure 4.50**). **Figure 4.51** indicates one way in which deterioration of the large spheroidal VC particles occurred. The outside edges of these VC particles showed micro indentations and/or spalling. The matrix was removed preferentially, leaving the VC particles

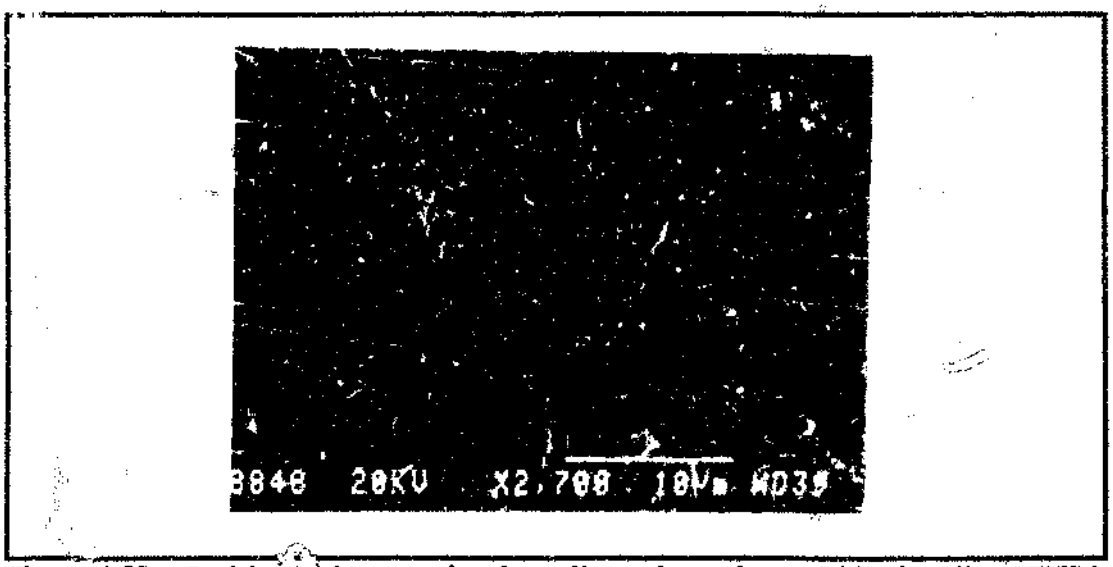

Figure 4.39 – Ledeburite in a matrix of pearlite and massive carbides in Alloy VF576.

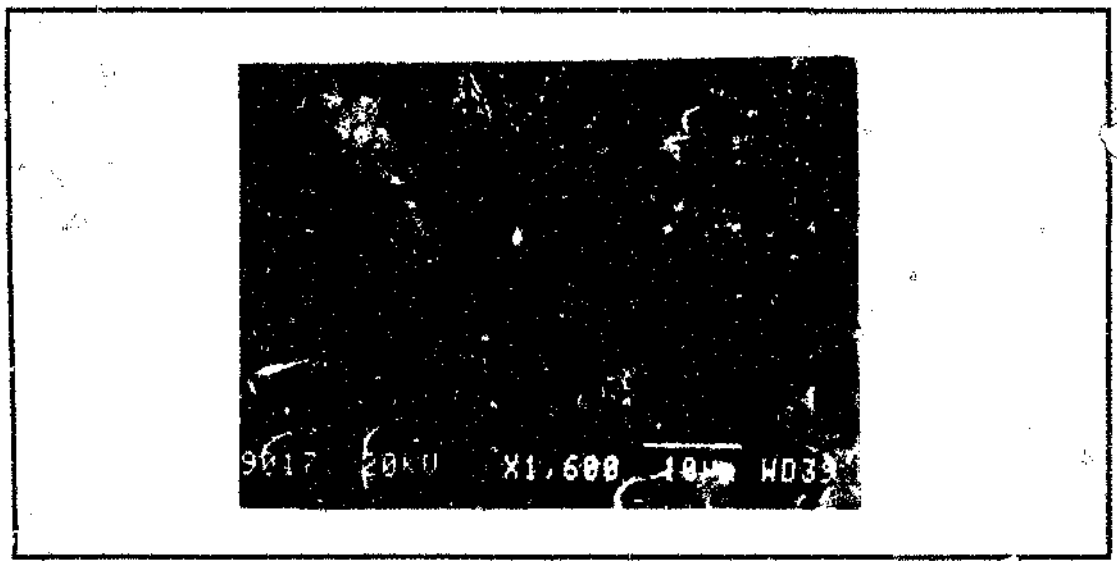

Figure 4.40. – Cracking of $VC_{0.76}$ dendrites surrounding the hardness indentation in Alloy VF576.

standing proud of the worn surface (Figure 4.52).

4.8. TEM results

TEM work was performed to identify the microstructure of the alloys at high magnification (up to 160000x). The microstructures showed areas containing pearlite (Figure 4.53). Small precipitates were also seen in the matrix. These had not been seen when using either optical or SEM imaging (see Figure 4.54).

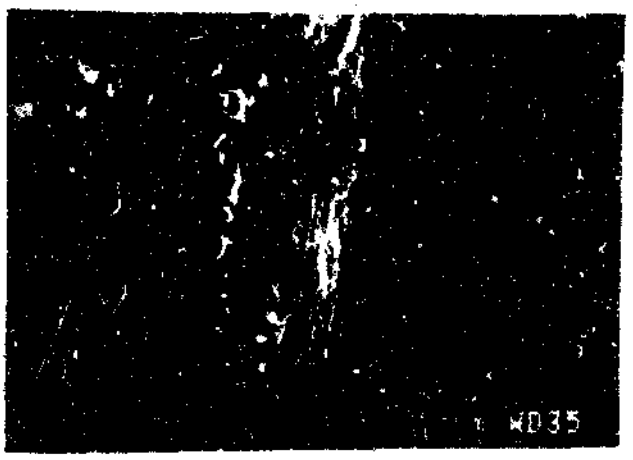

Figure 4.41. – Accelerated 3–body abrasion occuring in the region of dendritic VC particles.

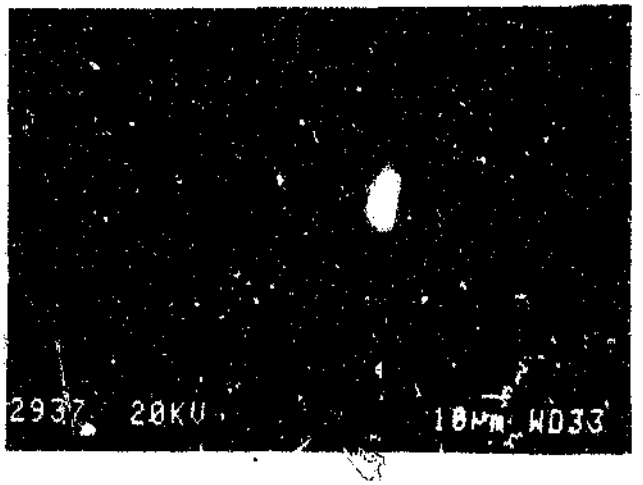

Figure 4.42. – Grooves running in 2–directions after wear tests carried out on the 3–body abrasion test machine prior to using the modified holder system.

Using SAD, the VC_{1-X} and α phases were analysed. The precipitates were too small to analyse. The diffraction patterns obtained are shown in **Figures 4.55** and **4.56** respectively. The VC_{1-X} phase had a lattice parameter of 4.16Å which corresponded to $VC_{0.76}$.

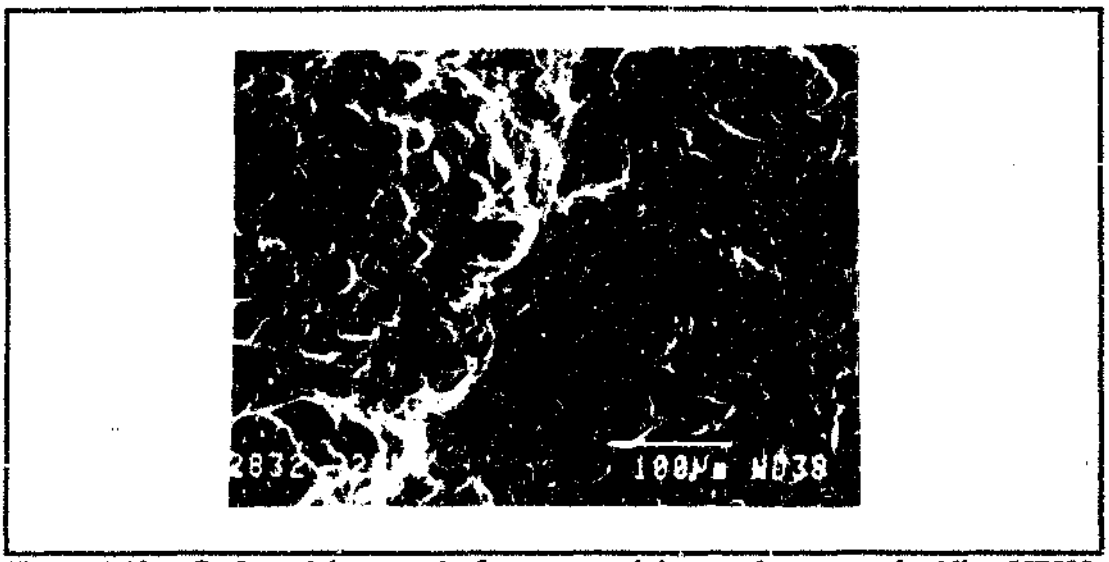

Figure 4.43. – Preferential removal of areas containing cracks as seen in Alloy VF609.

Figure 4.44. – Crack in a VC particle probably caused by release of residual stress during alloy preparation in Alloy VF609.

4.9. Jominy hardness traverses

The three round bar specimens of Alloy AF587C were tested under nominally the same quenching conditions. **Figure 4.57** shows the variation found in the hardenability. The thickness of material hardened is small. The variation in hardness indicates the low hardenability of the alloy matrix.

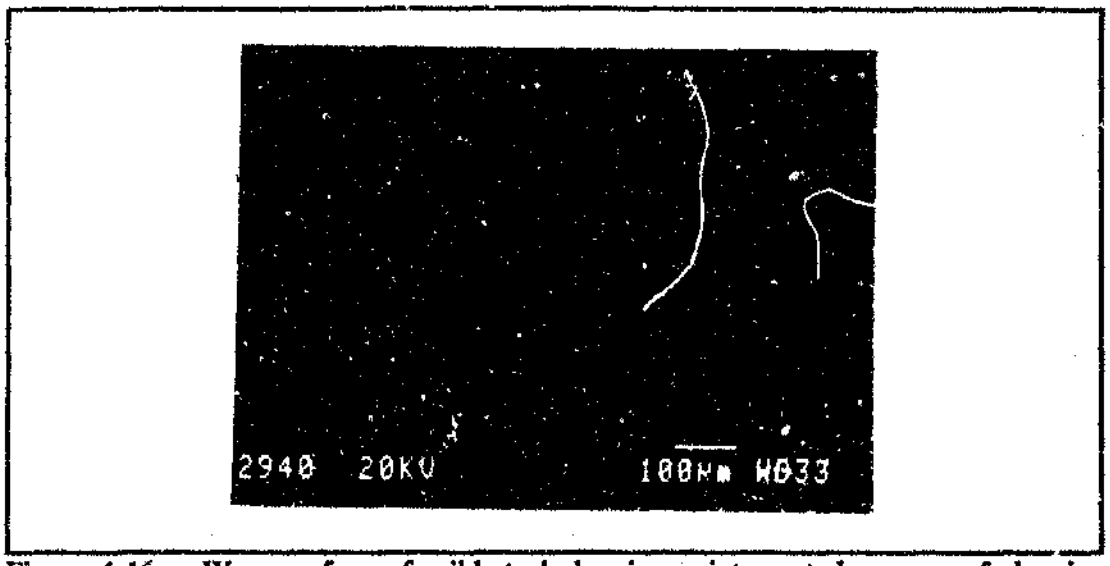

Figure 4.45. – Worn surface of mild steel showing uninterrupted passage of abrasive particles.

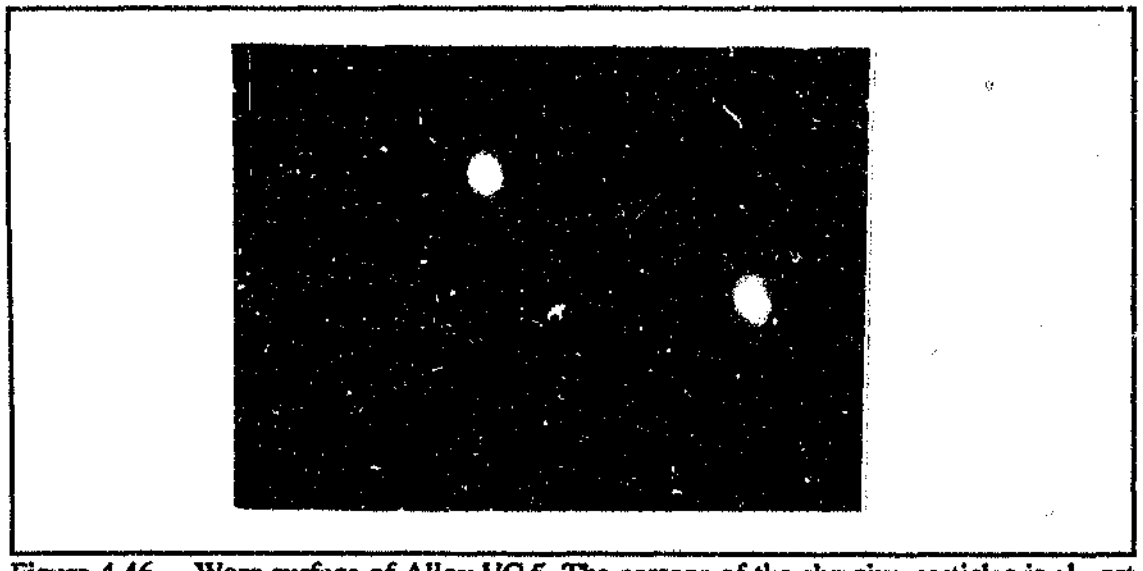

Figure 4.46. – Worn surface of Alloy VC 5. The passage of the abrasive particles is almost unhindered by the small VC particles.

4.10. Hardness results

Several of the alloys showed a high degree of scatter in hardness measurements. This scatter was highest in Phase 2 alloys due to the heterogeneous microstructures. The hardness measurements and standard deviations are reported, later in **Table 4.17.**

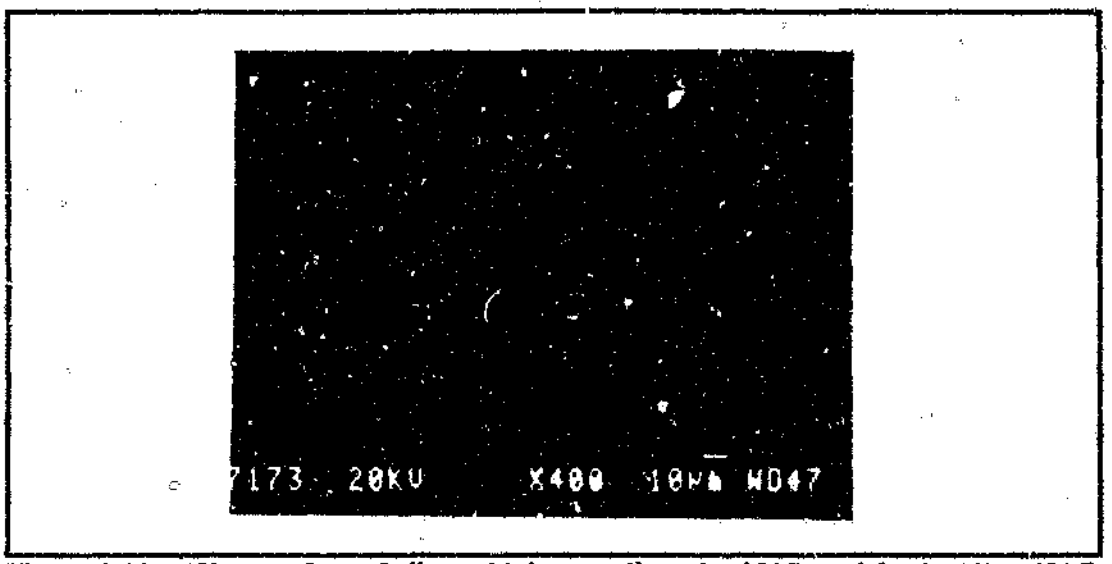

Figure 4.47. – Worn surface of alloy with intermediate sized VC particles in Alloy 681C. The abrasive particles are only partially hindered in their passage across the alloy surface.

Figure 4.48 – Worn surface of Alloy VF609 with large VC particles. Passage of the abrasive particles through the alloy surface prevented by the large VC particles.

The hardness of the arc melted alloys was higher than the corresponding as cast alloys. No correlation between the hardness and abrasive wear resistance could be found. No correlation between the increase in hardness and the microstructure could be found.

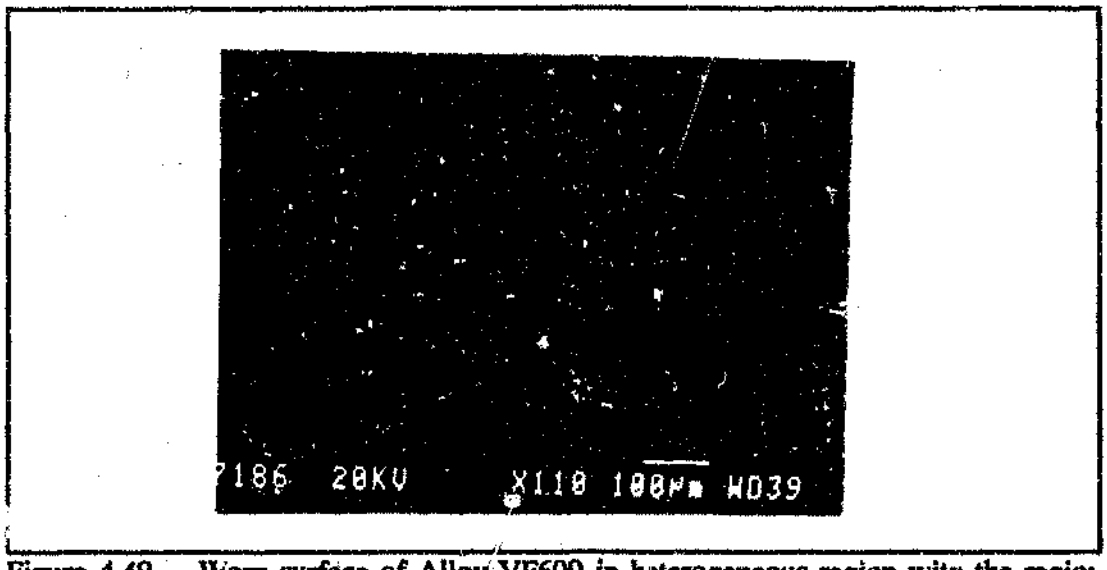

Figure 4.49. – Worn surface of Alloy VF609 in heterogeneous region with the region containing small VC particles showing faster wear.

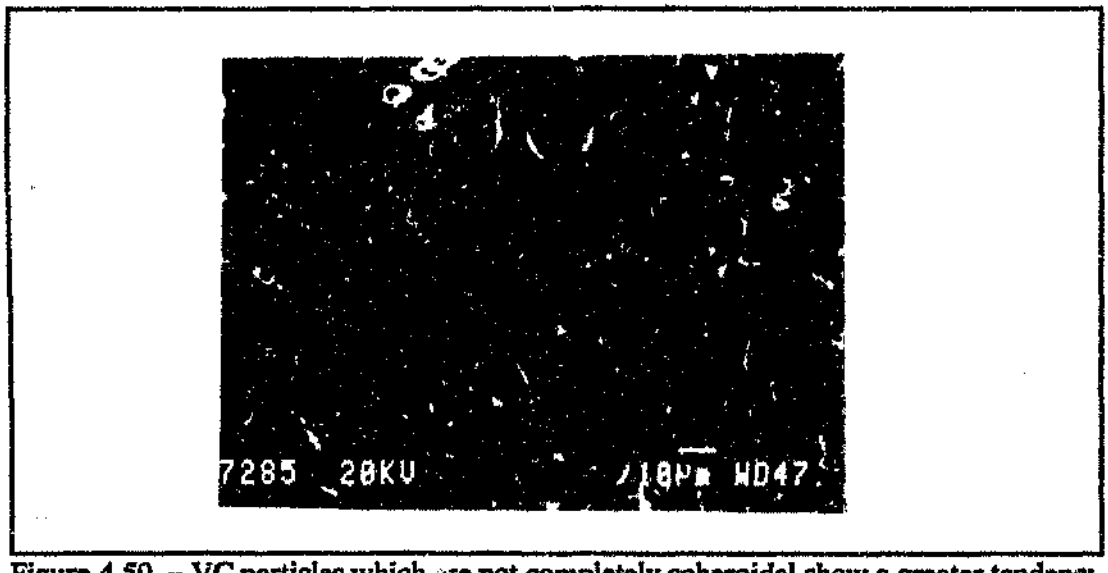

Figure 4.50. – VC particles which are not completely spheroidal show a greater tendency to spall.

4.11. 3–body abrasion test results

The 3–body abrasion test results showed a high degree of scatter (**Table 4.12**). VF608 had fluctuations in the mass loss per period of 2 orders of magnitude. Generally the wear rate dropped during a test run. The results are given graphically in **Figures 4.58** to **5.65**, and show the mass loss per period followed by the cumulative mass loss for each batch of alloys tested.

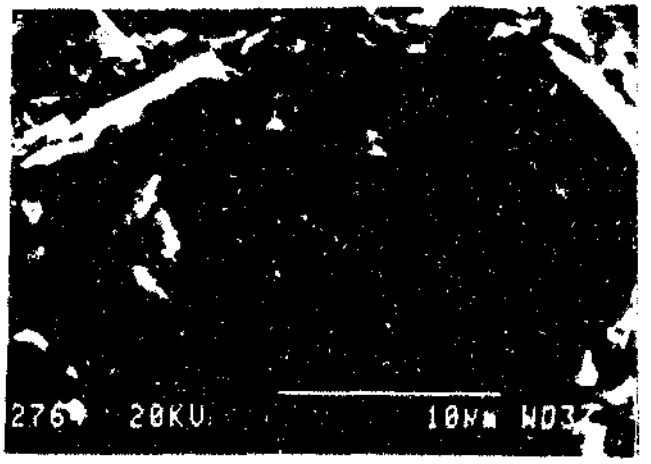

Figure 4.51. – The large VC particles break–up slowly by micro–fracture around the edges as seen in Alloy VF609.

Figure 4.52. – For large VC particles the matrix of the alloys is removed preferentially under 3 -body abrasive conditions as seen in Alloy VF609.

The four test runs performed are shown in sequence.

The results of the mild steel samples were extracted and are given in **Table 4.13.** From these the average and standard deviations measured during testing were calculated. The experimental error and accuracy of measurement were also calculated based on the formulae given in ASTM G65 – 84. The calculated errors are reported at the end of **Table 4.13.**

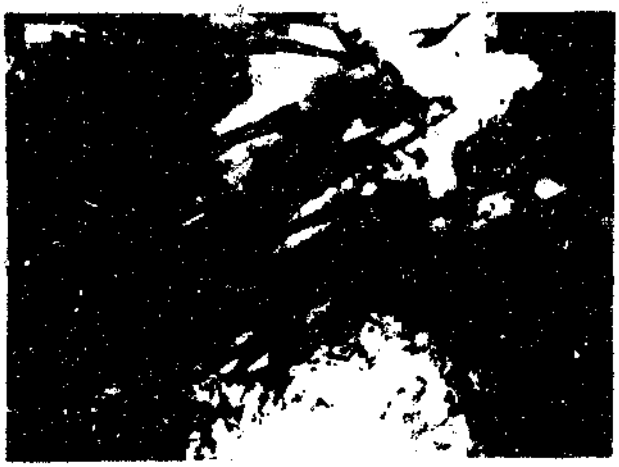

Figure 4.53. – Area of pearlite showing the lamellae of α and Fe_3C.

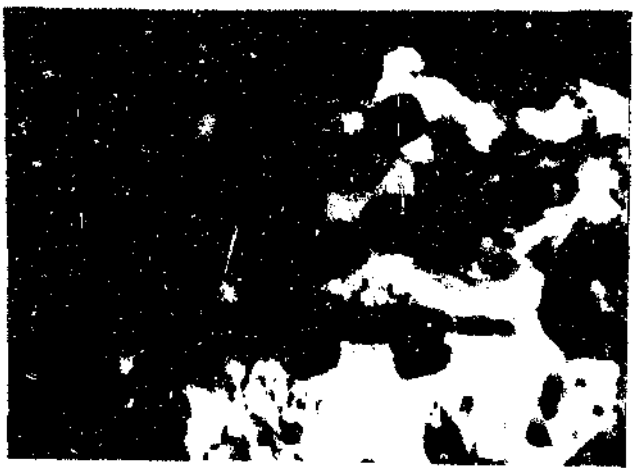

Figure 4.54. – Small precipitates detected by TEM in the α region.

Figure 4.55. - Diffraction pattern from VC_{1-x} obtained by the SAD technique.

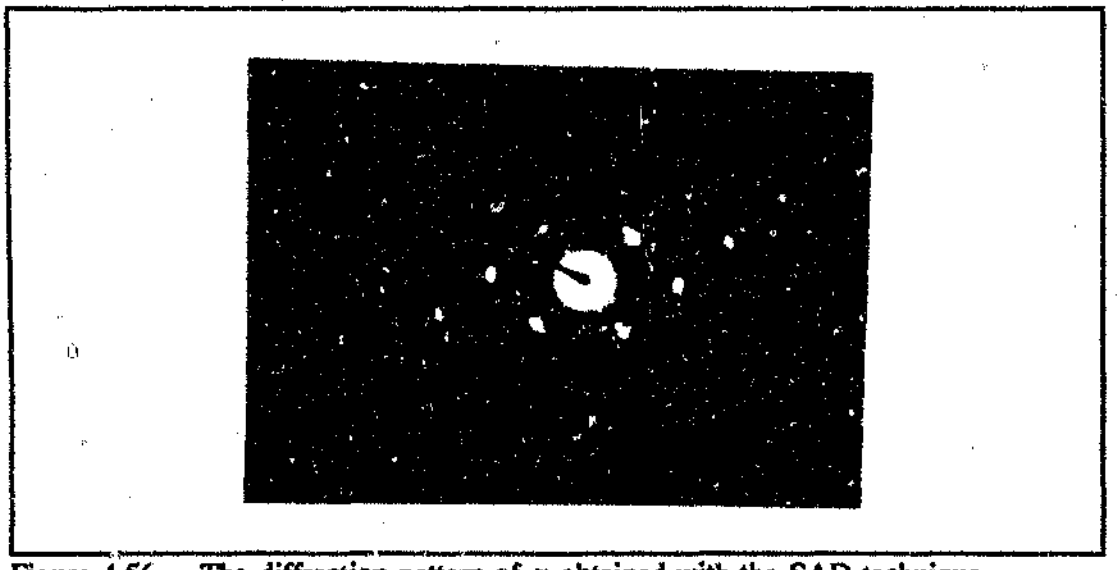

Figure 4.56. - The diffraction pattern of α obtained with the SAD technique.

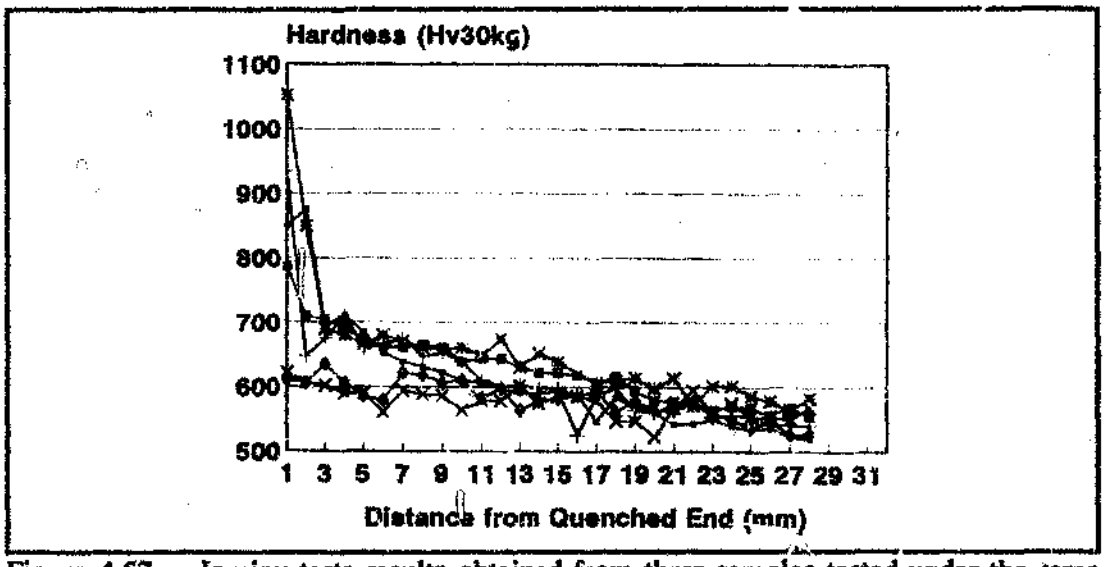

Figure 4.57. – Jominy tests results obtained from three samples tested under the same conditions. The low hardenability of these alloys is demonstrated by these experimental results.

Table 4.12. – 3 body abrasion test results

Batch	Alloy	Mass loss after first 15 mia period (mg)	Mass loss after second 15 min period (mg)	Mass loss after third 15 min period (mg)	Mass loss after fourth 15 min period (mg)	Mass loss after fifth 15 min period (mg)	Cumulative mass loss (mg)
1	MS 1	50.4	34.3	39.4	34.5	36.2	194.8
1	VF579	82.5	32.4	43.2	59.8	28.6	246.5
1	MS 2	48.7	36.0	21.4	40.9	33.9	180.9
1	VC7	19.2	14.7	19.3	16.9	11.0	81.1
2	MS 1	50.1	39.8	50.4	24.8	22.2	187.3
2	VF607	50.1	37.2	36.5	19.5	41.4	184.7
2	MS 2	23.1	48.7	40.3	16.4	36.1	78.2
2	VF576	11.4	20.8	27.0	7.7	11.3	78.2
3	MS 1	53.2	47.9	40.6	39.3	21.5	202.5
3	VF608	12.7	10.2	1.0	8.7	0.1	32.7
3	MS 2	39.5	33.8	39.1	32.0	34.0	178.4
3	VF609	4.7	3.5	2.1	4.4	0.7	15.4
4	MS 1	51.3	29.5	48.2	36.1	36.4	201.5
4	VC5	35.9	29.2	10.1	23.0	17.0	115.2
4	MS 2	40.9	47.0	39.1	19.7	30.6	177.3

Table 4.13. – Wear results from the calibration steel samples used in 3–body abrasion tests.

Specimen	Mass loss after first 15 min period (mg)	Mass loss after second 15 min period (mg)	Mass loss after third 15 min period (mg)	Mass loss after fourth 15 min period (mg)	Mass loss after fifth 15 min period (mg)	Cumulative mass loss (mg)
MS 1	78.6	78.7	48.4	41.6	31.4	278.7
MS 2	70.4	69.2	56.4	35.6	37.5	269.1
MS 1	50.4	34.3	39.4	34.5	36.2	194.8
MS 2	48.7	36.0	21.4	40.9	33.9	180.9
MS 1	50.1	39.8	50.4	24.8	22.2	187.3
MS 2	23.1	48.7	40.3	16.4	36.1	164.6
MS 1	53.2	47.9	40.6	39.3	21.5	202.5
MS 2	39.5	33.8	39.1	32.0	34.0	178.4
MS 1	51.3	29.5	48.2	36.1	36.4	201.5
MS 2	40.9	47.0	39.1	19.7	30.6	177.3
Max	78.6	78.7	56.4	41.6	37.5	278.7
Min	23.1	29.5	21.4	16.4	21.5	164.6
Avg	50.6	46.5	42.3	32.1	32.0	203.5
Std. dev.	14.7	15.2	9.0	8.4	5.5	36.9

NB a) A measure of the experimental error can be obtained by comparing the range of cumulative mass loss (CML) values to the average cumulative mass loss value

ie $\frac{(\text{Max CML} - \text{Min CML})}{\text{Avg CML}} \times \frac{100}{1} = 56.1\%$

b) Method used to determine the error in measurement in a system in ASTM G65–84, compares the standard deviation with the cumulative mass loss

ie $\frac{(\text{std. dev})}{\text{Avg CML}} \times \frac{100}{1} = 25.6\%$

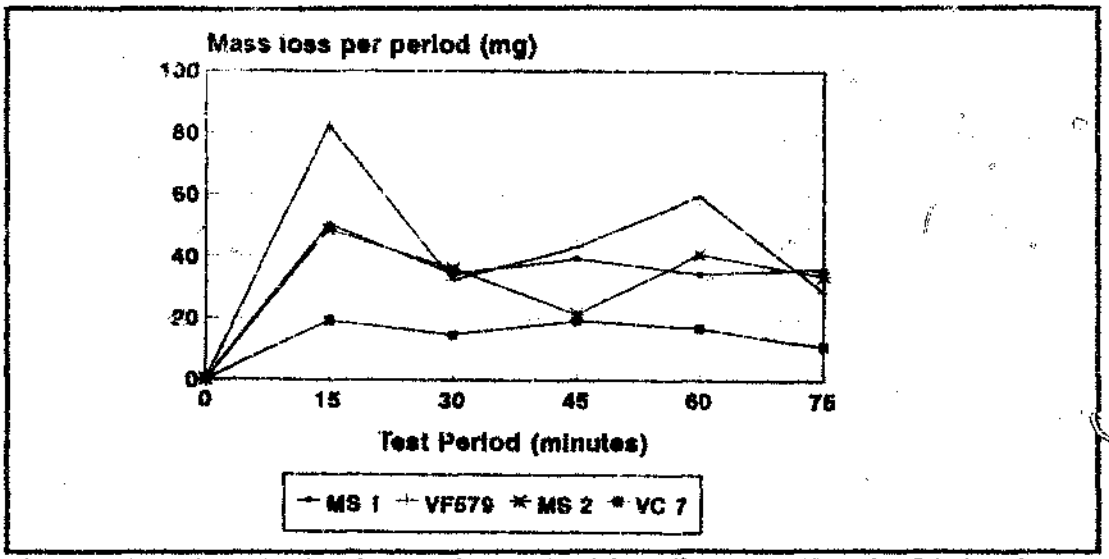

Figure 4.58. – 3–body abrasion results obtained for Alloys VF579 and VC7 showing the mass loss per period.

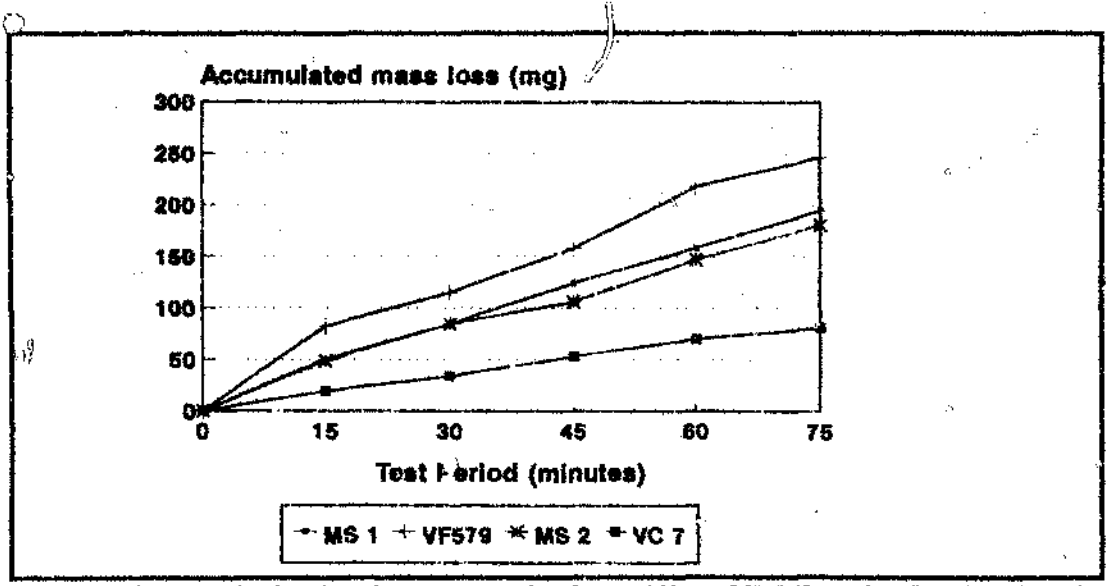

Figure 4.59. – 3–body abrasion test results from Alloys VF579 and VC7 showing the accumulated mass loss.

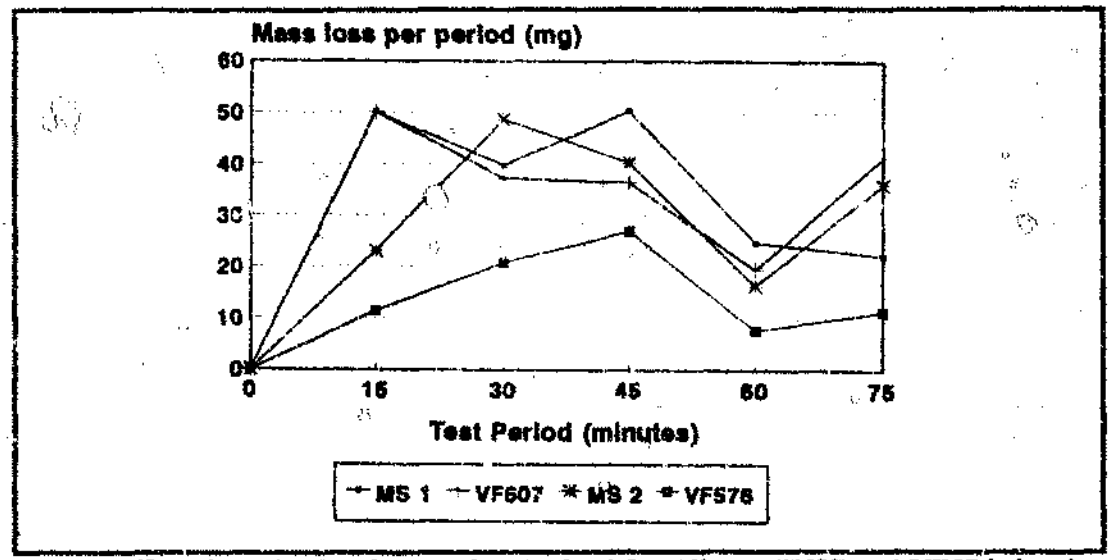

Figure 4.60. – 3–body abrasion results obtained for Alloys VF607 and VF576 showing the mass loss per period.

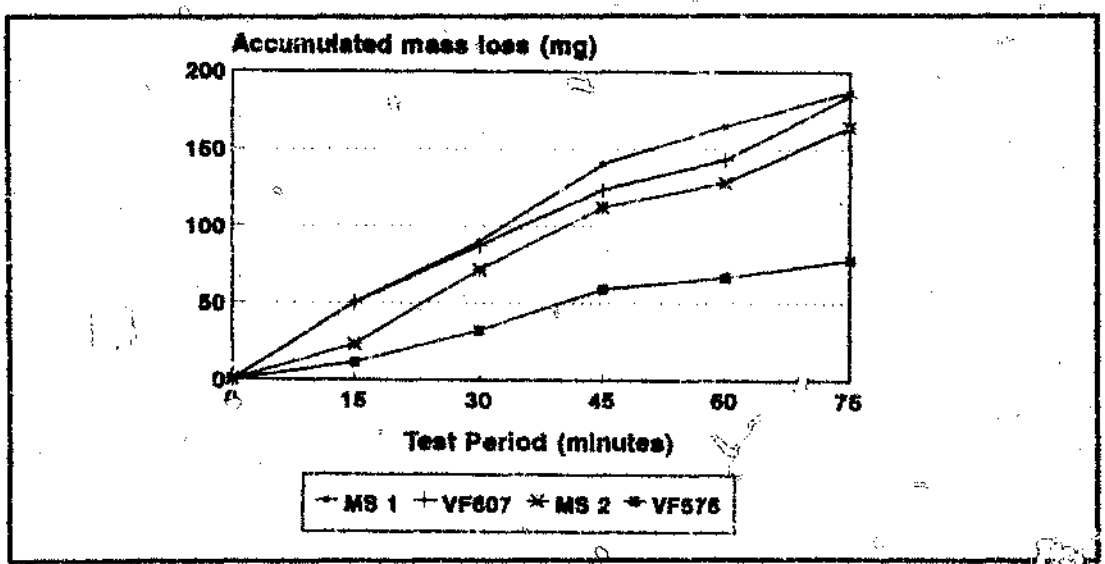

Figure 4.61. – 3–body abrasion test results from Alloys VF607 and VF576 showing the accumulated mass loss.

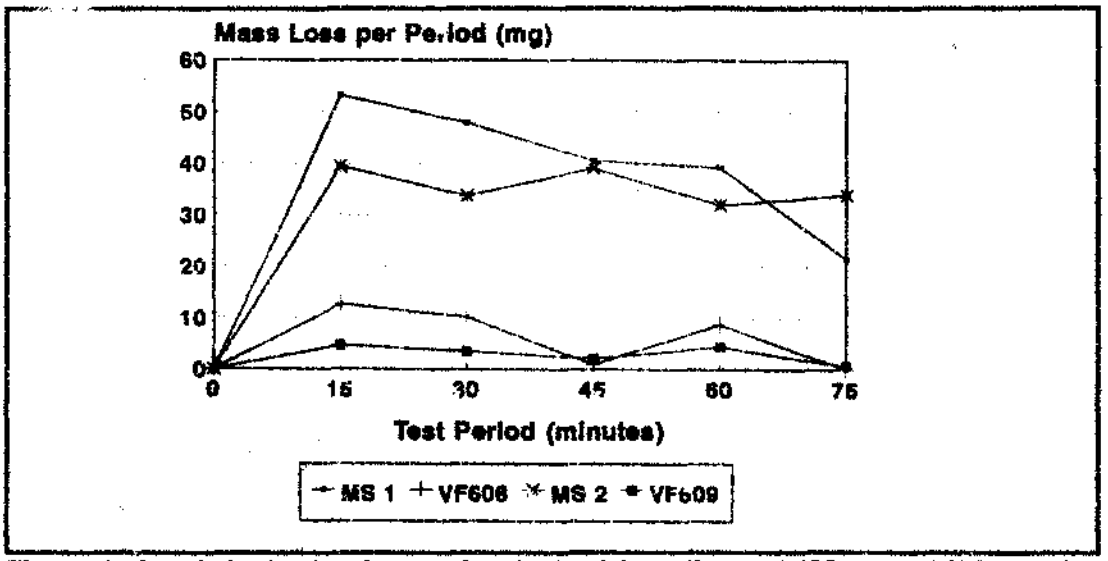

Figure 4.62. - 3-body abrasion results obtained for Alloys VF608 and VF609 showing the mass loss per period.

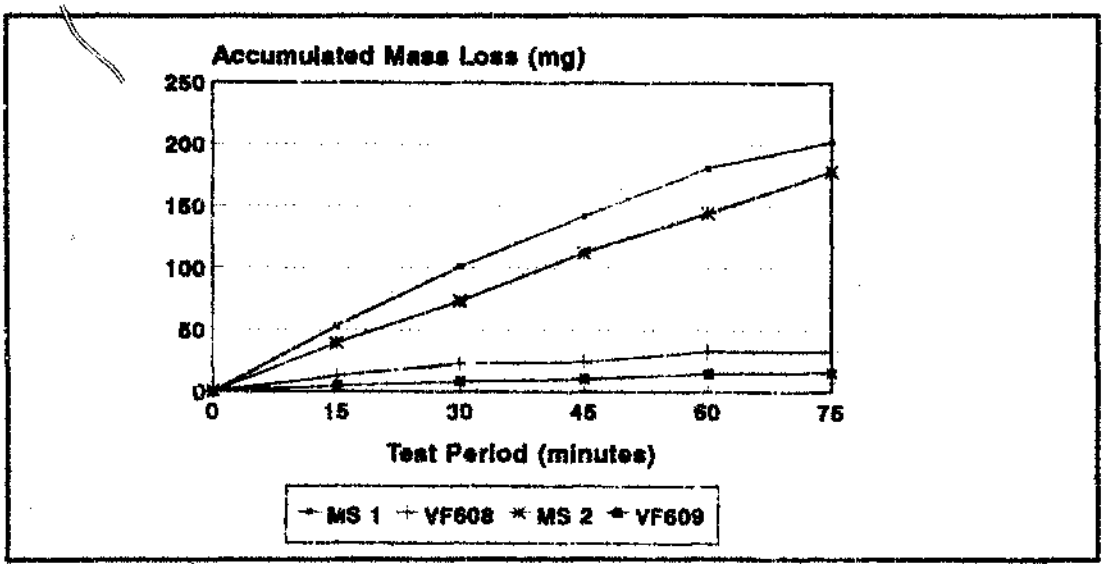

Figure 4.63. - 3-body abrasion test results from Alloys VF608 and VF609 showing the accumulated mass loss.

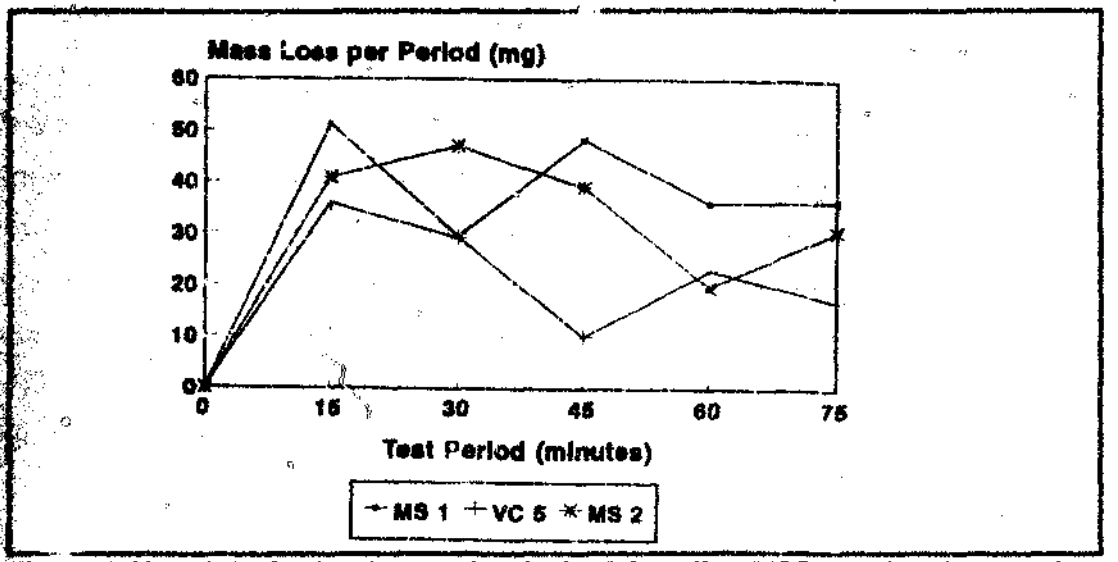

Fig : 4.64. – 3–body abrasion results obtained for Alloy VC5 showing the mass loss per period.

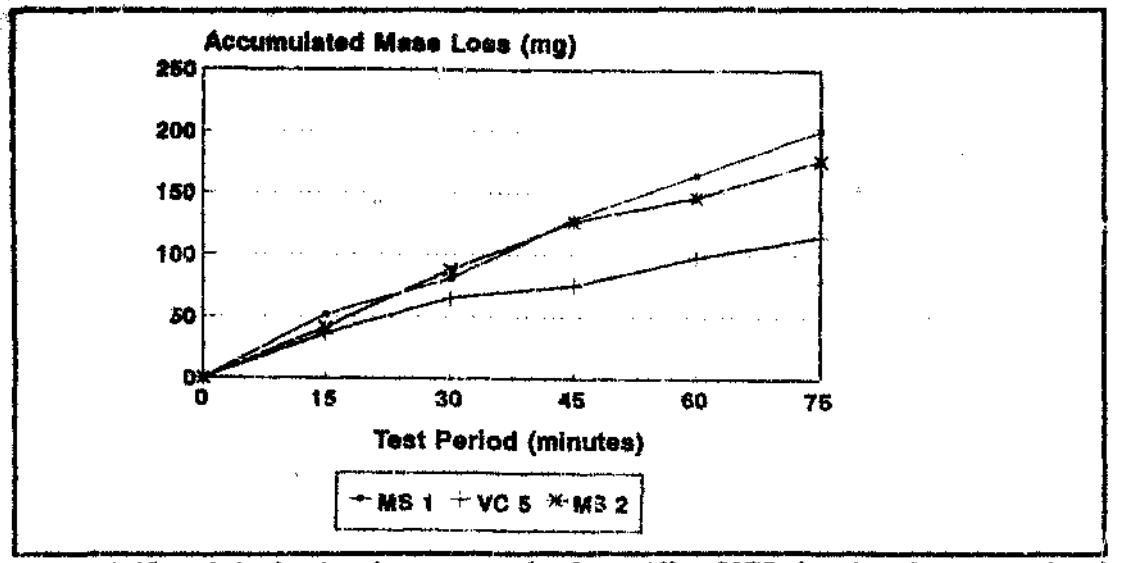

Figure 4.65. – 3–body abrasion test results from Alloy VC5 showing the accumulated mass loss.

4.12. Modified 3-body abrasion test results

The abrasion results obtained with the modified holder system are shown in **Table 4.14**. The wear rate dropped during the course of a test run. The same fluctuation in mass loss did not occur. The comparative mass loss of the steel calibration samples is shown in **Table 4.15**. No increase in measured weight loss occurred during a test run on any of the steel calibration samples. The experimental error and measuring accuracy was again determined according to ASTM G65-84 and are shown in **Table 4.15**. Graphs showing the mass loss per period and cumulative mass loss per period are shown for each run in **Figures 4.66** to **4.87**.

Table 4.14. – Modified 3–body abrasion test results. Note that the test period is double that in Table 4.12.

Alloy	Mass loss after first 30 min period (mg)	Mass loss after second 30 min period (mg)	Mass loss after third 30 min period (mg)	Mass loss after fourth 30 min period (mg)	Mass loss after fifth 30 min period (mg)	Cumulative mass loss (mg)
VC5	94.40	69.29	49.50	37.78	33.84	248.81
VC7	56.19	29.99	20.61	16.29	13.46	136.54
VC8	59.77	36.00	25.10	19.79	16.43	157.09
VF576	97.68	78.21	63.55	49.68	41.87	330.99
VF607	22.57	17.35	11.53	11.81	9.85	73.11
VF608	41.93	29.22	22.97	18.25	15.82	128.19
VF609	4.01	1.42	1.11	0.43	1.28	8.25
681A	72.57	57.35	43.18	56.51	34.19	263.80
681C	20.59	8.10	5.82	4.43	4.24	43.18
AF583C	26.28	20.79	16.14	13.49	12.52	89.22
AF584C	35.18	23.89	20.17	17.12	16.29	112.65
AF585C	19.38	9.37	8.98	7.19	5.96	50.88
AF586A	36.84	22.01	16.01	11.46	10.00	96.32
AF587C	35.32	26.07	22.61	18.28	17.04	119.32
AF588C	21.20	11.38	8.96	7.70	7.32	56.56
AF589C	26.19	15.83	13.24	11.39	10.20	76.85
AF583A	31.64	24.16	15.62	9.88	11.89	94.19
AF584A	28.88	19.63	29.33	15.53	14.14	107.51
AF585A	39.30	23.24	19.87	16.87	12.56	111.84
AF588A	21.28	14.36	11.54	7.99	8.53	63.70
AF589A	28.26	18.35	15.03	12.81	11.29	85.74
WC[i]	6.67	5.17	3.61	4.71	2.35	22.51
MC[ii]	3.75	2.05	1.92	2.19	2.02	11.93
CrC[iii]	5.02	2.38	2.08	3.10	2.42	15.00

(i) – Commercial Tungsten Carbide Hardfacing alloy[32].
(ii) – Commercial Mixed Carbide Hardfacing alloy[32].
(iii) – Commercial Chromium Carbide Hardfacing alloy[32].

Table 4.15. – Wear results from the calibration steel samples used in the modified 3–body abrasion tests. Note that the period of each test is double that in Table 4.13.

Sample	Mass loss after first 30 min period (mg)	Mass loss after second 30 min period (mg)	Mass loss after third 30 min period (mg)	Mass loss after fourth 30 min period (mg)	Mass loss after fifth 30 min period (mg)	Cumulative mass loss (mg)
MS 1	136.4	111.5	92.5	72.7	58.6	471.70
MS 2	132.6	85.7	62.8	46.9	40.2	368.20
MS 3	150.3	120.4	81.6	61.2	54.4	467.90
MS 4	141.2	110.5	80.2	64.4	53.4	449.70
MS 5	147.4	118.9	86.3	61.6	53.2	467.40
MS 6	145.6	106.8	80.4	73.4	54.3	460.50
MS 7	146.8	117.5	85.5	66.3	57.0	473.10
MS 8	138.1	108.8	77.8	64.8	56.3	445.80
MS 9	125.8	105.2	83.9	65.3	55.3	435.50
MS 10	118.6	101.7	75.1	60.3	51.2	406.90
MS 11	125.1	103.6	83.7	68.4	56.3	437.10
MS 12	119.0	97.2	67.2	51.6	43.9	378.90
MS 13	118.4	108.5	95.1	83.8	75.3	481.10
MS 14	116.0	107.8	88.4	77.8	70.1	460.10
MS 15	122.1	108.8	95.6	82.0	69.2	477.70
MS 16	119.6	109.4	93.2	83.0	87.6	492.80
Max	150.3	120.4	95.6	83.8	87.6	492.80
Min	116.0	85.7	62.8	46.9	40.2	368.20
Avg	131.4	107.6	83.1	67.7	58.5	448.40
Std	11.8	8.2	9.1	10.3	11.4	34.8

Notes :

1) The experimental error is less than seen in **Table 4.13.**
ie $\frac{(\text{Max AML} - \text{Min AML})}{\text{Avg AML}} \times \frac{100}{1} = 27.8\%$

2) The error in measurement is also less than in **Table 4.13.**
ie $\frac{(\text{std. dev})}{\text{Avg AML}} \times \frac{100}{1} = 7.8\%$

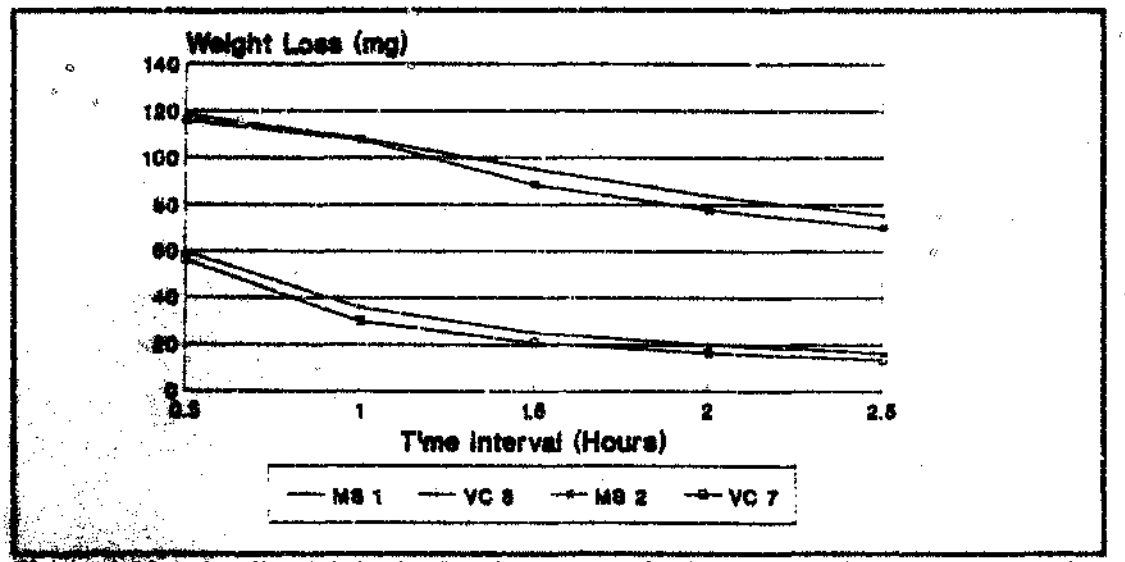

Figure 4.66. – Modified 3–body abrasion test results for alloys VC7 and VC8 showing the mass loss per period.

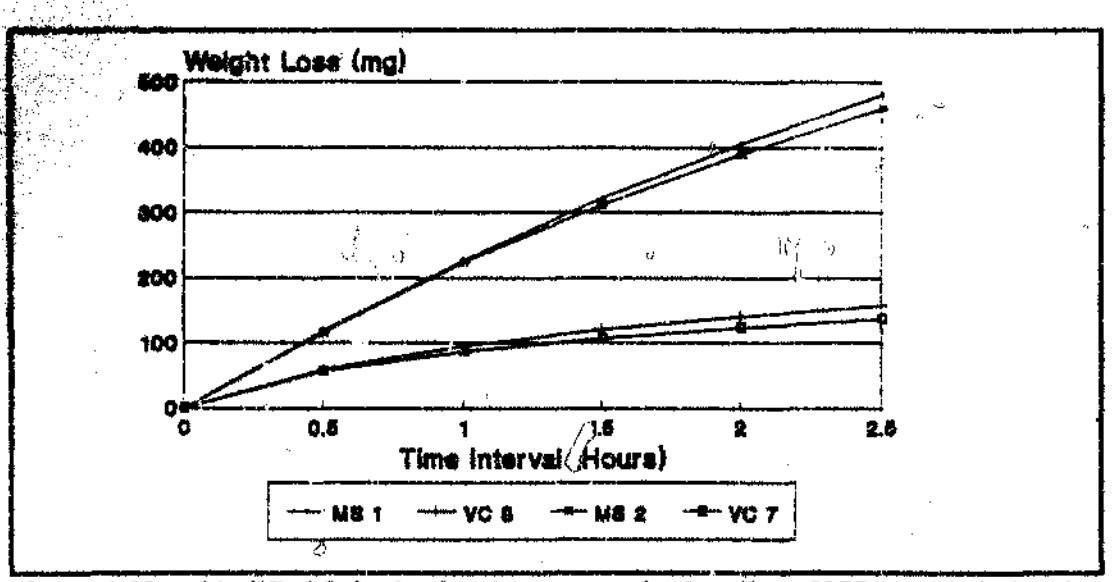

Figure 4.67. – Modified 3–body abrasion test results for alloys VC7 and VC8 showing the accumulated mass loss.

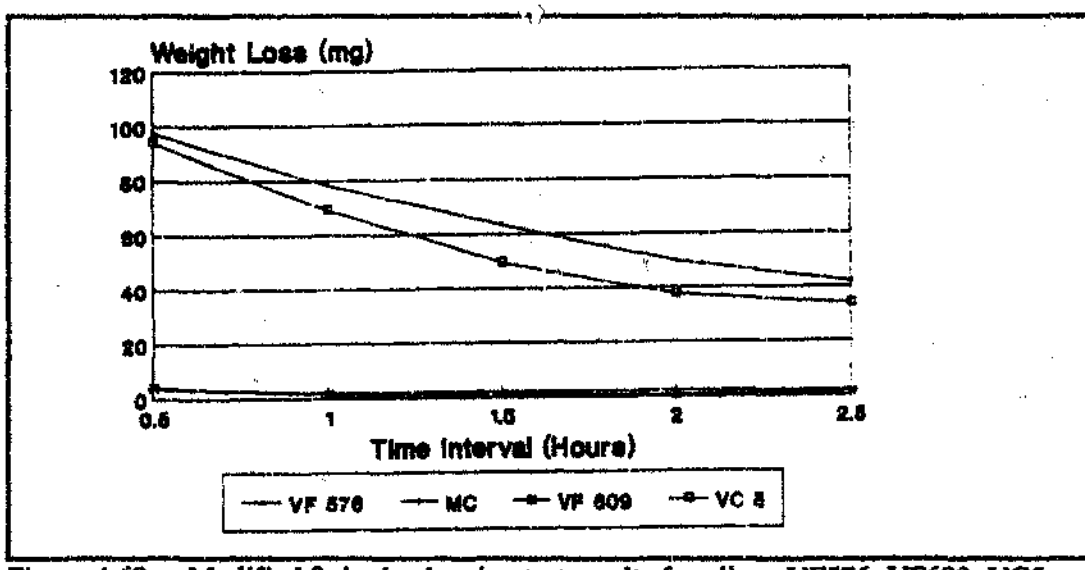

Figure 4.68. – Modified 3–body abrasion test results for alloys VF576, VF609, VC5 and the mixed carbide[37] hardfacing sample showing the mass loss per period.

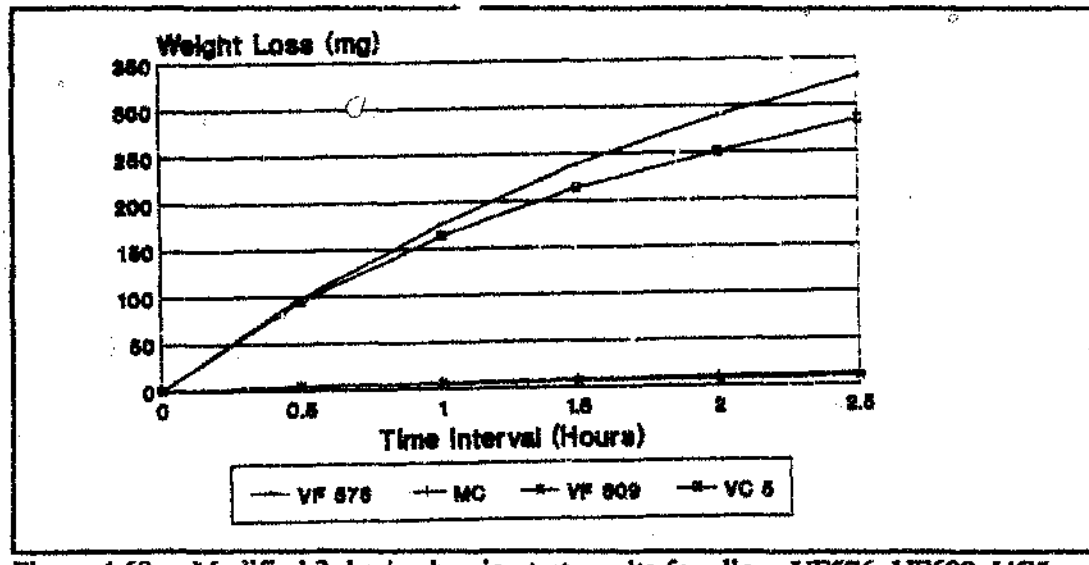

Figure 4.69. – Modified 3–body abrasion test results for alloys VF576, VF609, VC5 and the mixed carbide[37] hardfacing sample showing the accumulated mass loss.

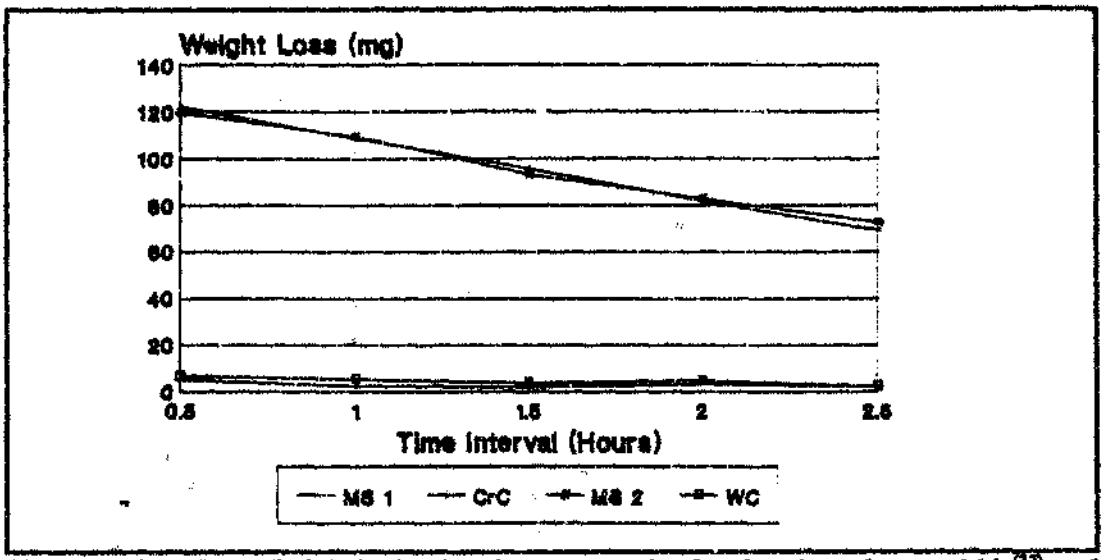

Figure 4.70. – Modified 3–body abrasion test results for the chromium carbide[37] and tungsten carbide[37] hardfacing alloys showing the mass loss per period.

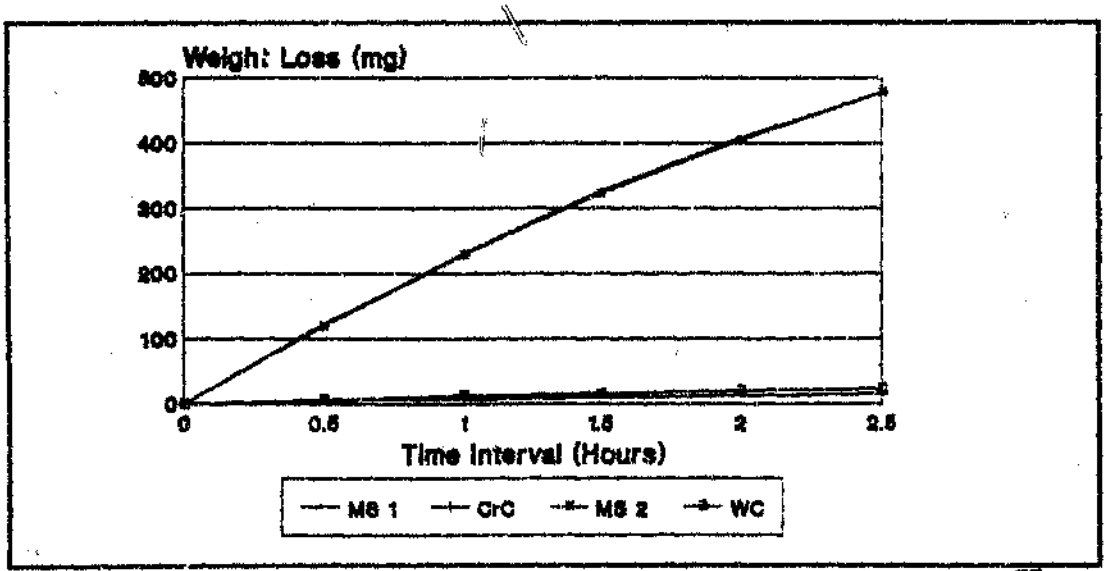

Figure 4.71. – Modified 3–body abrasion test results for the chromium carbide[37] and tungsten carbide[37] hardfacing alloys showing the accumulated mass loss.

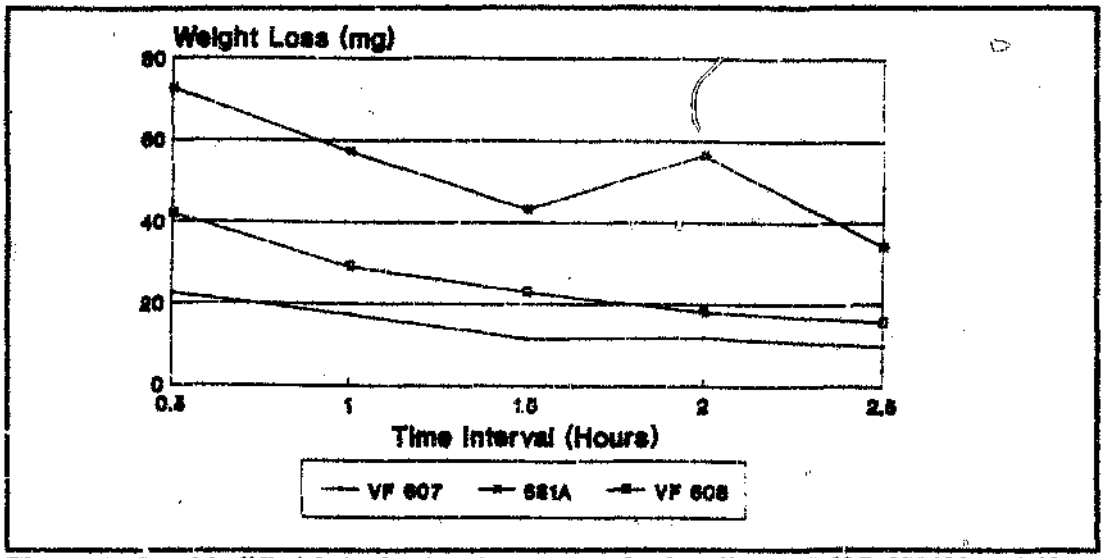

Figure 4.72. – Modified 3–body abrasion test results for alloys VF607, VF608 and 681A showing the mass loss per period.

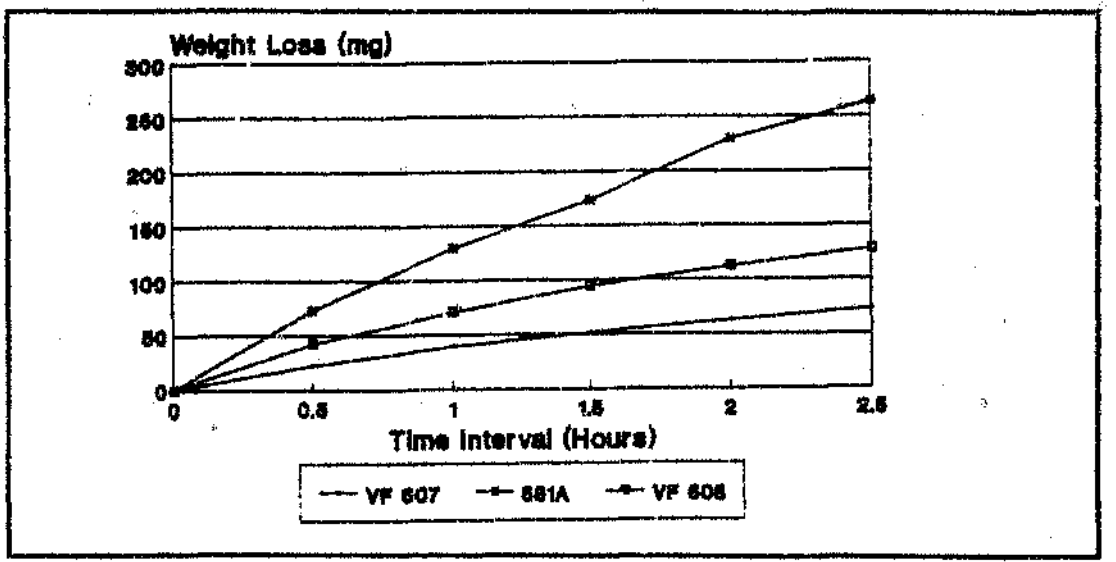

Figure 4.73. – Modified 3–body abrasion test results for alloys VF607, VF608 and 681A showing the accumulated mass loss.

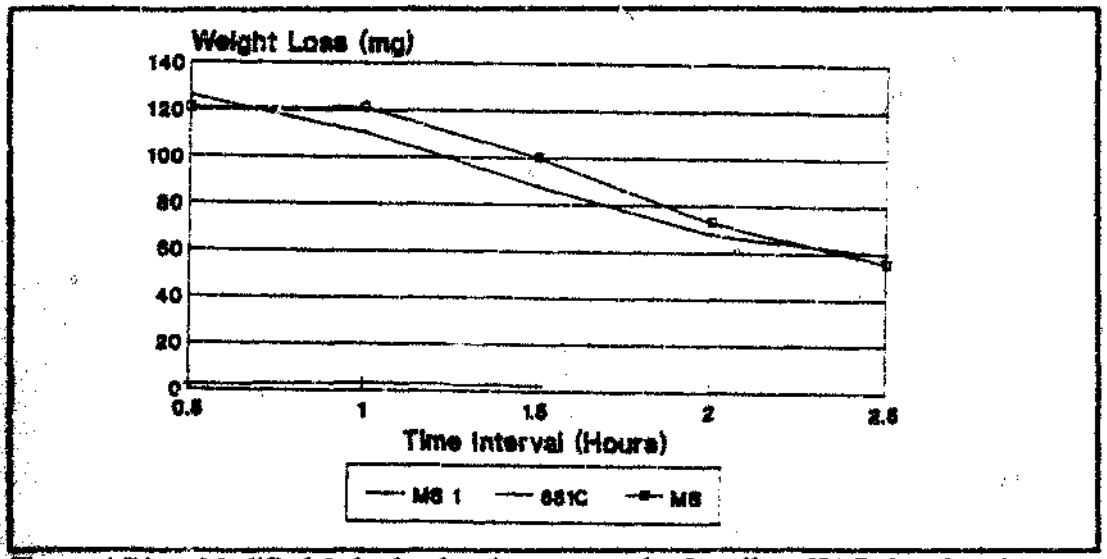

Figure 4.74. - Modified 3-body abrasion test results for alloy 681C showing the mass loss per period.

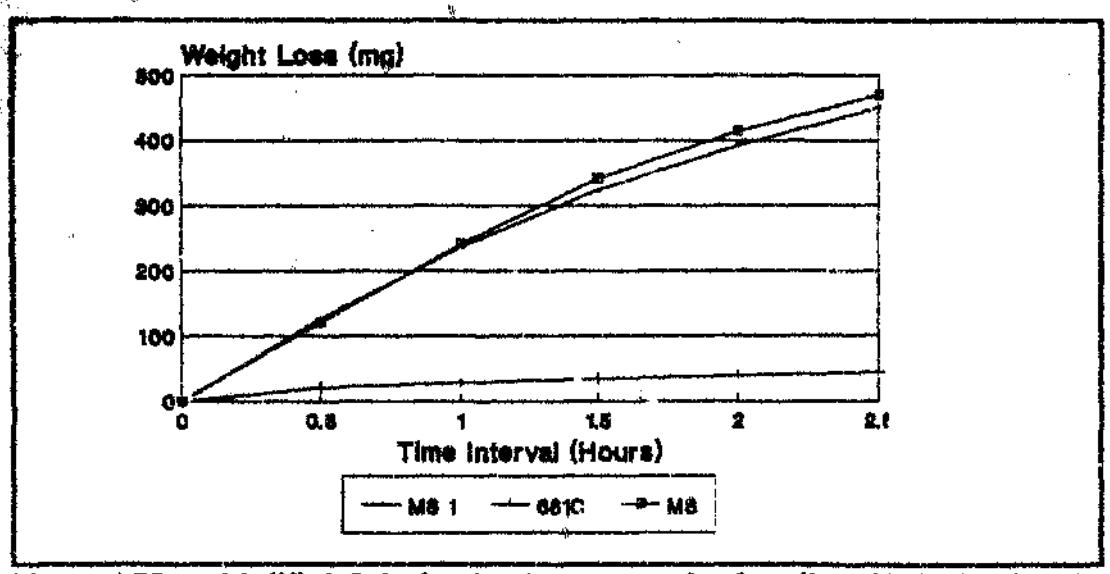

Figure 4.75. - Modified 3-body abrasion test results for alloy 681C showing the accumulated mass loss.

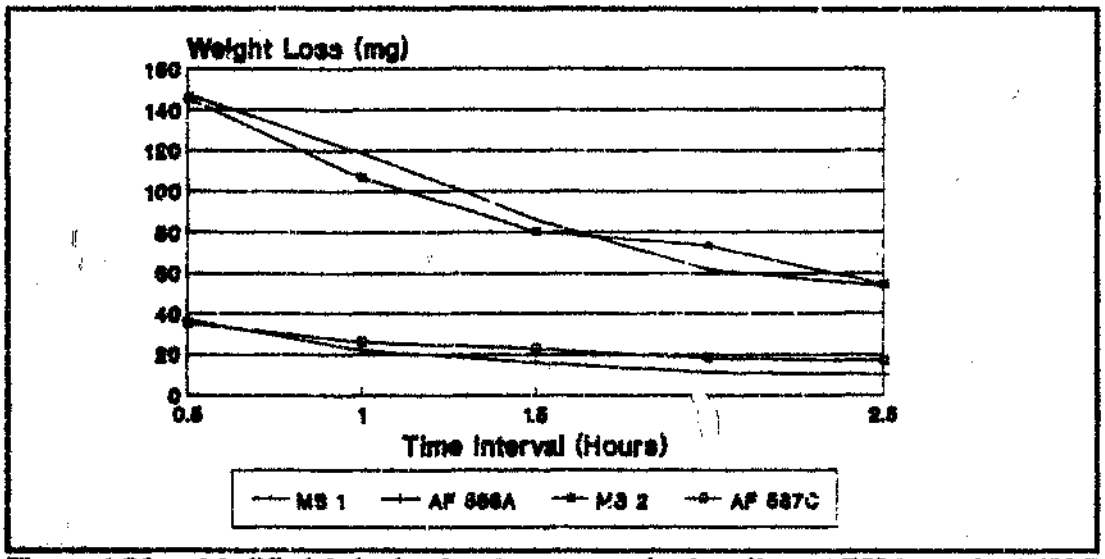

Figure 4.76. – Modified 3–body abrasion test results for alloys AF586A and AF587C showing the mass loss per period.

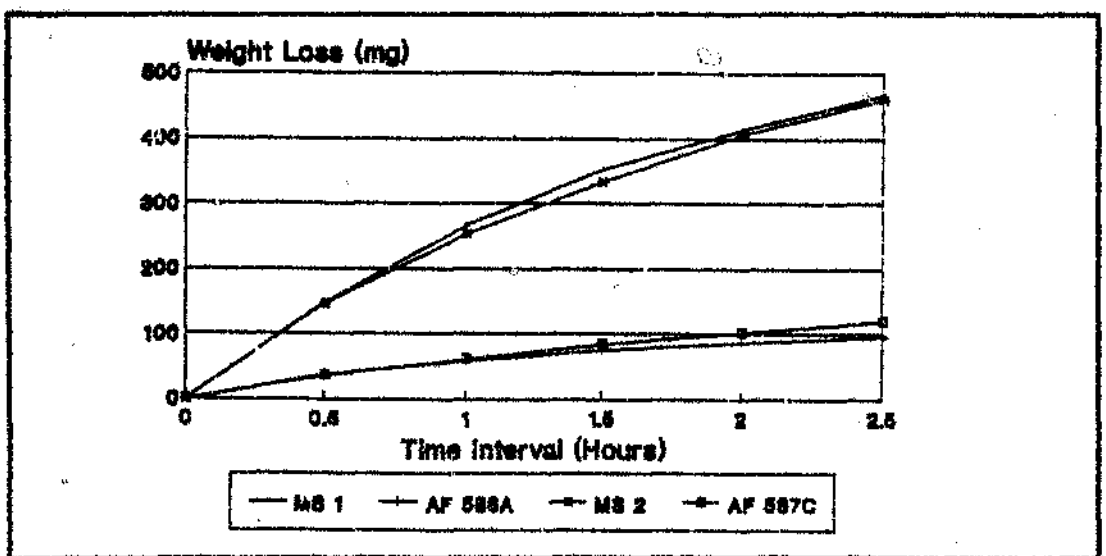

Figure 4.77. – Modified 3–body abrasion test results for alloys AF586A and AF587C showing the accumulated mass loss.

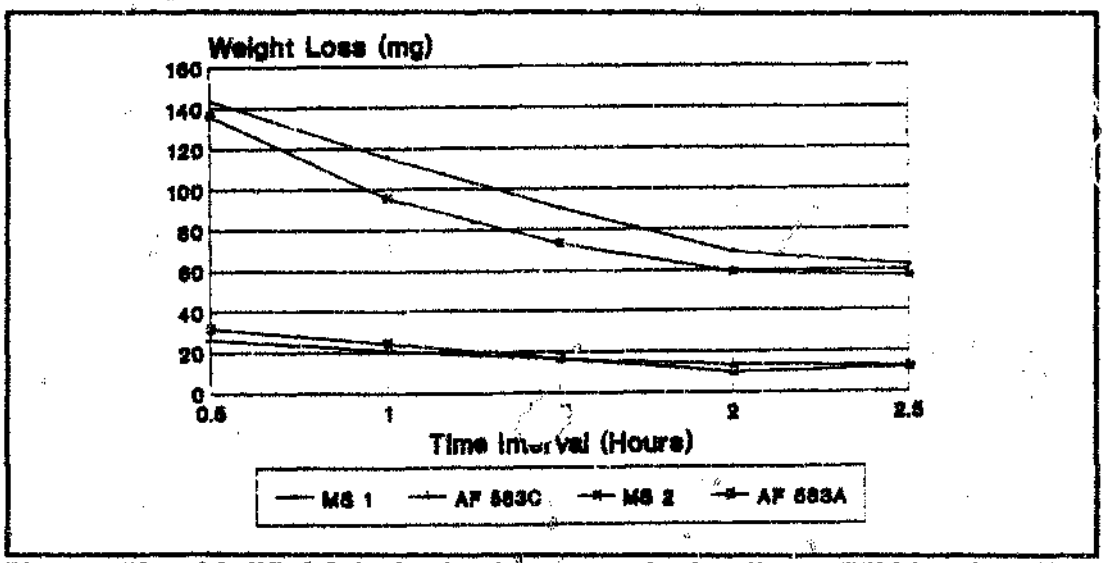

Figure 4.78. – Modified 3–body abrasion test results for alloys AF583C and AF583A showing the mass loss per period.

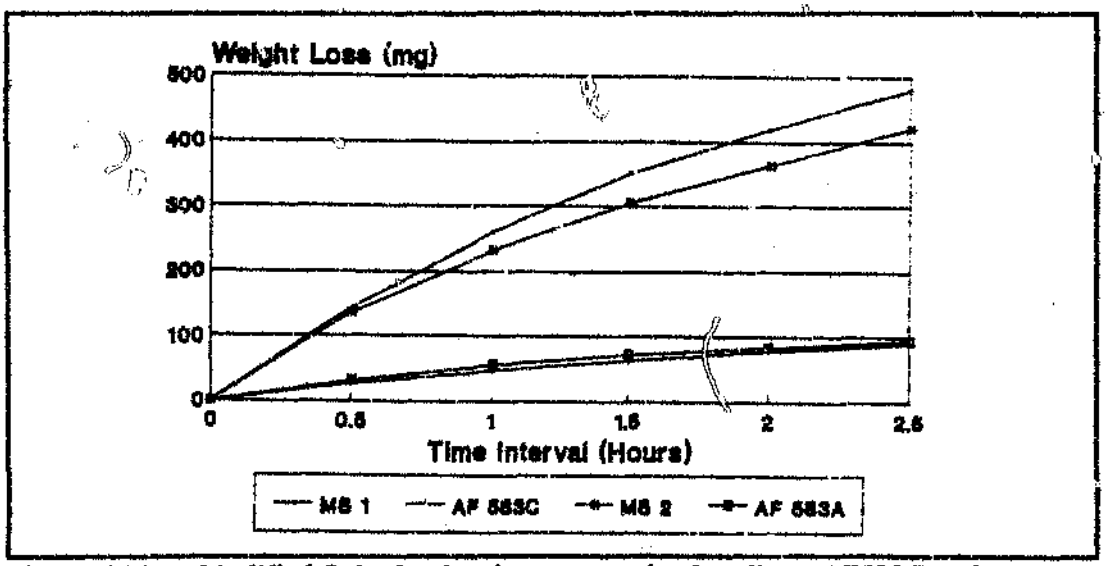

Figure 4.79. – Modified 3–body abrasion test results for alloys AF583C and AF583A showing the accumulated mass loss.

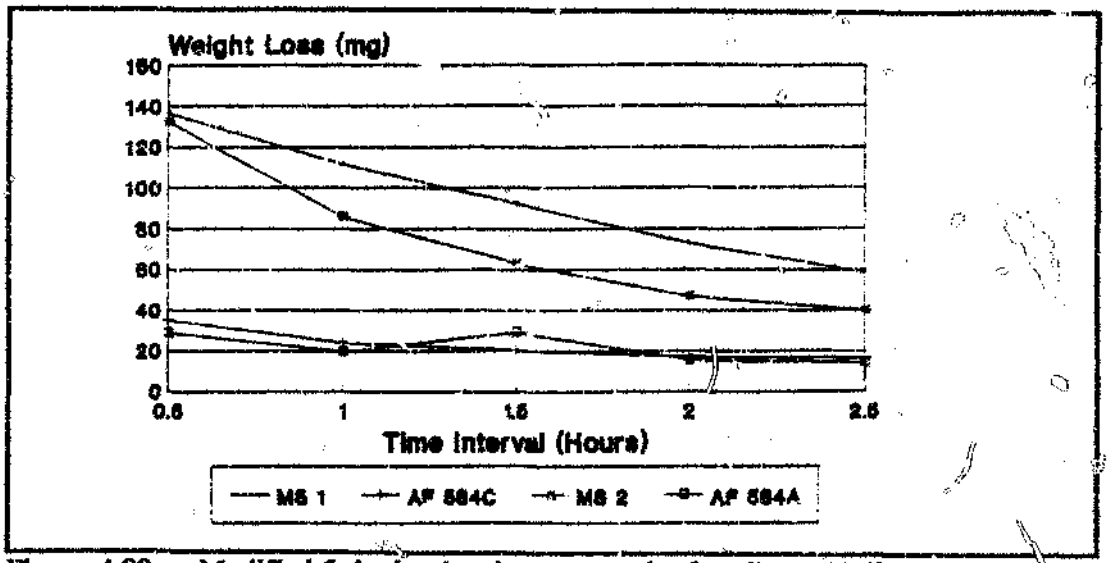

Figure 4.80. – Modified 3-body abrasion test results for alloys AF584C and AF584A showing the mass loss per period.

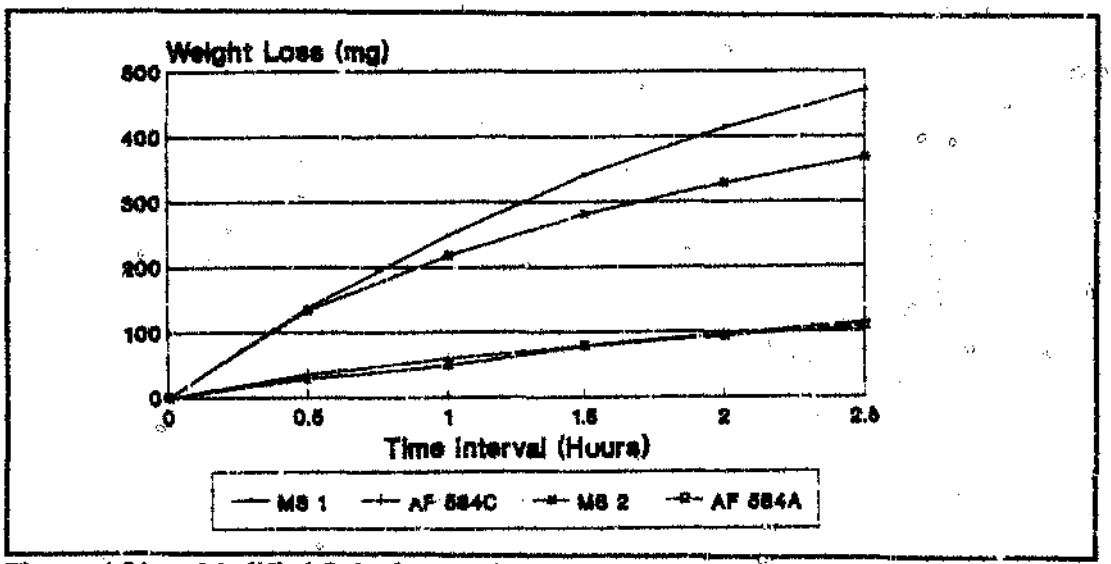

Figure 4.81. – Modified 3-body abrasion test results for alloys AF584C and AF584A showing the accumulated mass loss.

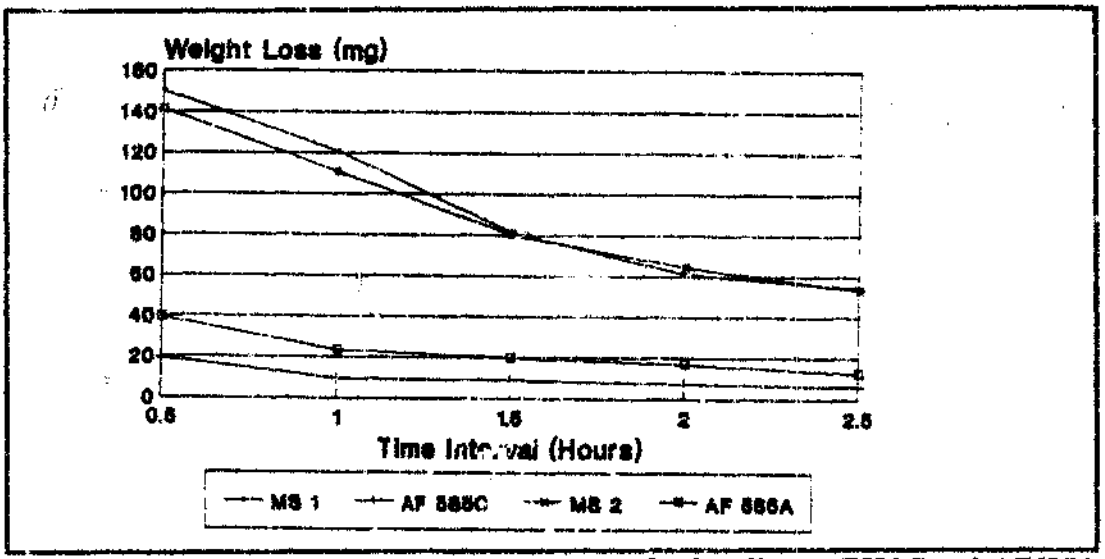

Figure 4.82. - Modified 3-body abrasion test results for alloys AF585C and AF585A showing the mass loss per period.

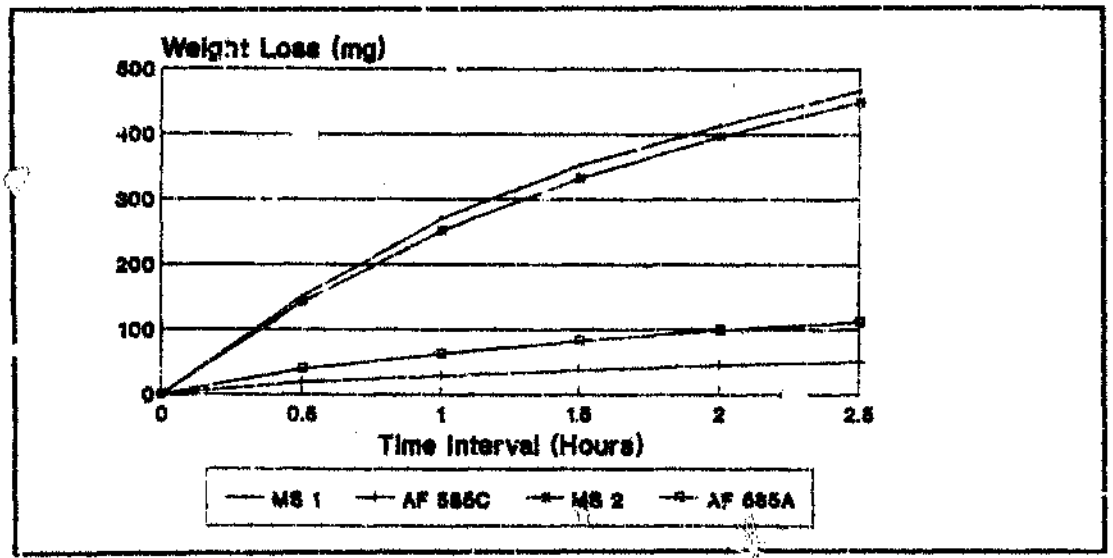

Figure 4.83. - Modified 3-body abrasion test results for alloys AF585C and AF585A showing the accumulated mass loss.

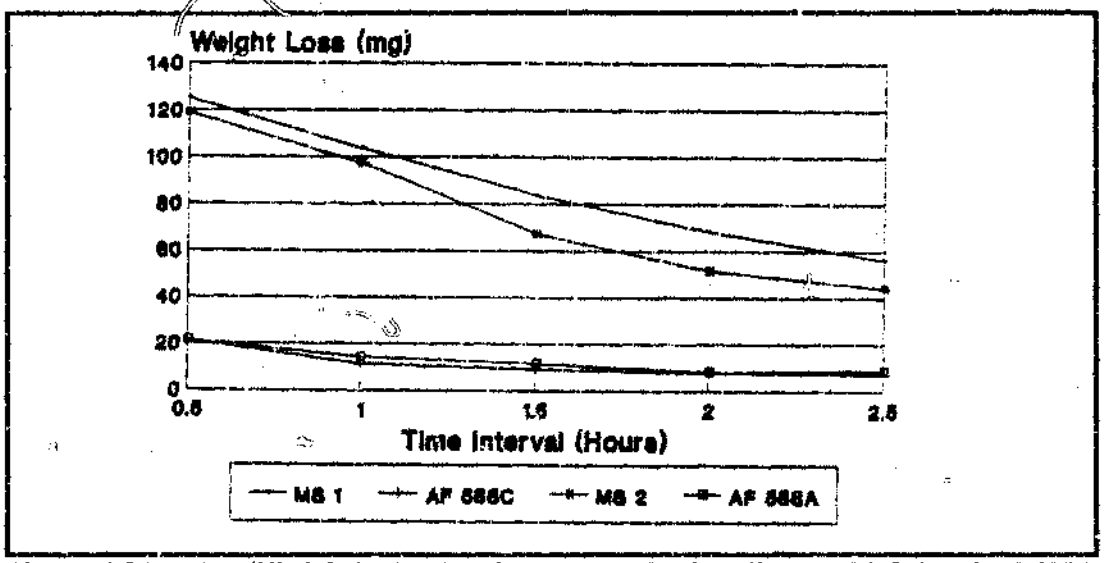

Figure 4.84. - Modified 3-body abrasion test results for alloys AF588C and AF588A showing the mass loss per period.

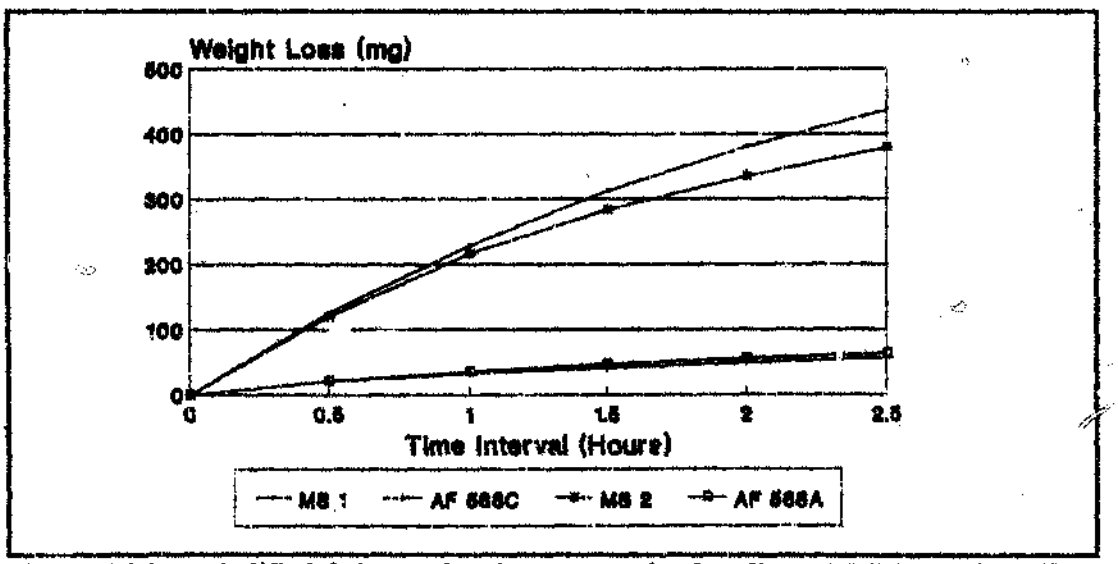

Figure 4.85. - Modified 3-body abrasion test results for alloys AF588C and AF588A showing the accumulated mass loss.

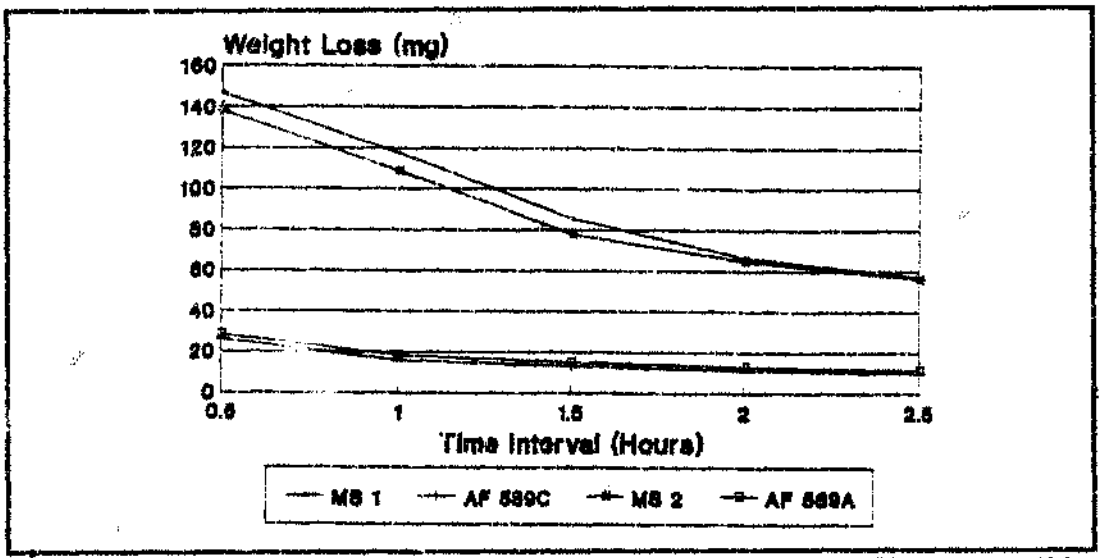

Figure 4.86. – Modified 3-body abrasion test results for alloys AF589C and AF589A showing the mass loss per period.

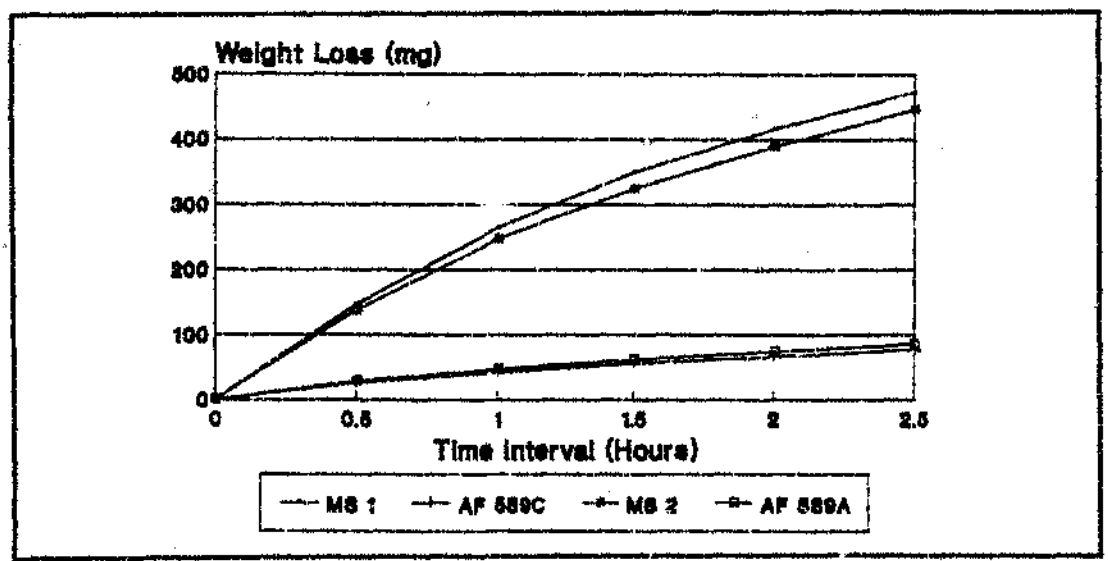

Figure 4.87. – Modified 3-body abrasion test results for alloys AF589C and AF589A showing the accumulated mass loss.

4.13. 2-Body abrasion results

The results of 2-body abrasion tests are given in **Table 4.16.** The wear rates from steel samples indicated a relatively stable weight loss. Alloys VC5, VC7 and VC8 showed similar trends. All the remaining alloys showed a marked drop in wear rate after the first period. The remaining four periods then showed similar wear rates.

The mass loss per period and the cumulative mass loss for five groups of materials are shown in **Figures 4.88** to **4.99**.

Table 4.16. – 2–body abrasion test results

Alloy	Mass loss after first 7.5 min period (mg)	Mass loss after second 7.5 min period (mg)	Mass loss after third 7.5 min period (mg)	Mass loss after fourth 7.5 min period (mg)	Mass loss after fifth 7.5 min period (mg)	Cumulative mass loss (mg)
MS1	157.2	154.6	187.8	188.5	182.1	870.20
MS2	163.9	170.9	173.1	172.8	171.6	852.30
MS3	171.9	173.3	175.7	177.9	173.9	872.70
MS4	181.1	182.3	181.1	184.0	185.3	913.80
VC5	221.3	231.7	226.2	212.7	203.9	1095.8
VC7	156.6	159.3	158.5	162.1	157.8	794.3
VC8	178.7	173.4	175.4	174.5	179.9	881.9
VF676	10.5	6.2	9.5	4.3	4.8	35.3
VF687	29.3	18.3	16.9	15.7	16.7	96.9
VF688	5.7	2.9	2.5	3.1	2.7	16.9
VF689	2.8	1.2	1.0	0.7	1.3	7.0
681A	18.7	8.0	4.1	5.2	4.8	40.8
688C	5.5	2.2	1.9	1.5	1.3	12.4
AF583C	16.0	11.6	10.7	12.3	14.1	64.7
AF584C	10.0	6.3	5.6	5.9	5.0	32.2
AF585C	6.6	3.4	2.8	1.8	2.1	16.7
AF586A	22.3	11.7	10.6	9.2	8.9	62.7
AF587C	16.7	9.8	10.1	11.4	10.4	58.4
AF588C	6.2	3.4	2.6	2.6	2.6	17.4
AF589C	5.0	3.6	3.4	3.0	2.8	17.8
AF583A	18.8	14.6	14.9	14.6	16.0	78.9
AF584A	10.0	5.5	5.8	5.3	5.4	32.0
AF585A	5.7	2.7	2.3	2.1	1.4	14.2
AF588A	4.1	2.5	2.0	1.7	1.5	11.8
AF589A	9.2	5.1	4.6	4.1	3.7	25.7
WC[60]	3.5	1.9	2.3	1.4	1.4	10.5
MC[60]	7.2	4.8	4.5	4.7	4.3	25.5
CrC[60]	21.3	18.6	18.4	18.5	18.2	95.0

(i) – Commercial Tungsten Carbide Hardfacing alloy[32].

(ii) – Commercial Mixed Carbide Hardfacing alloy[32].

(iii) – Commercial Chromium Carbide Hardfacing alloy[32].

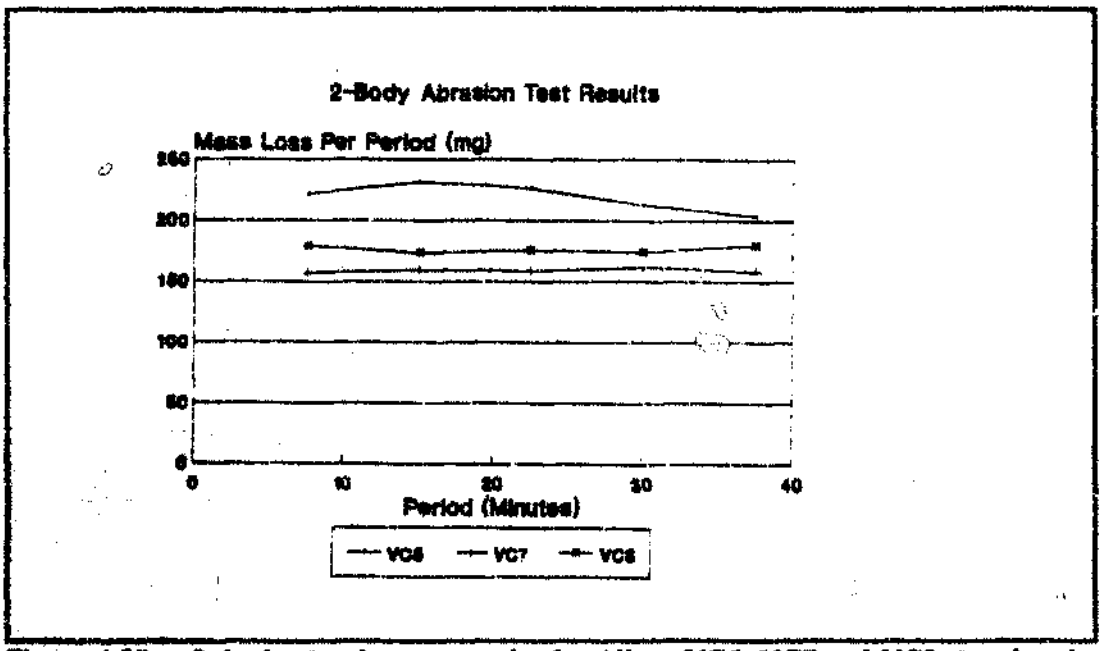

Figure 4.88. – 2–body abrasion test results for Alloys VC5, VC7 and VC8 showing the mass loss per period.

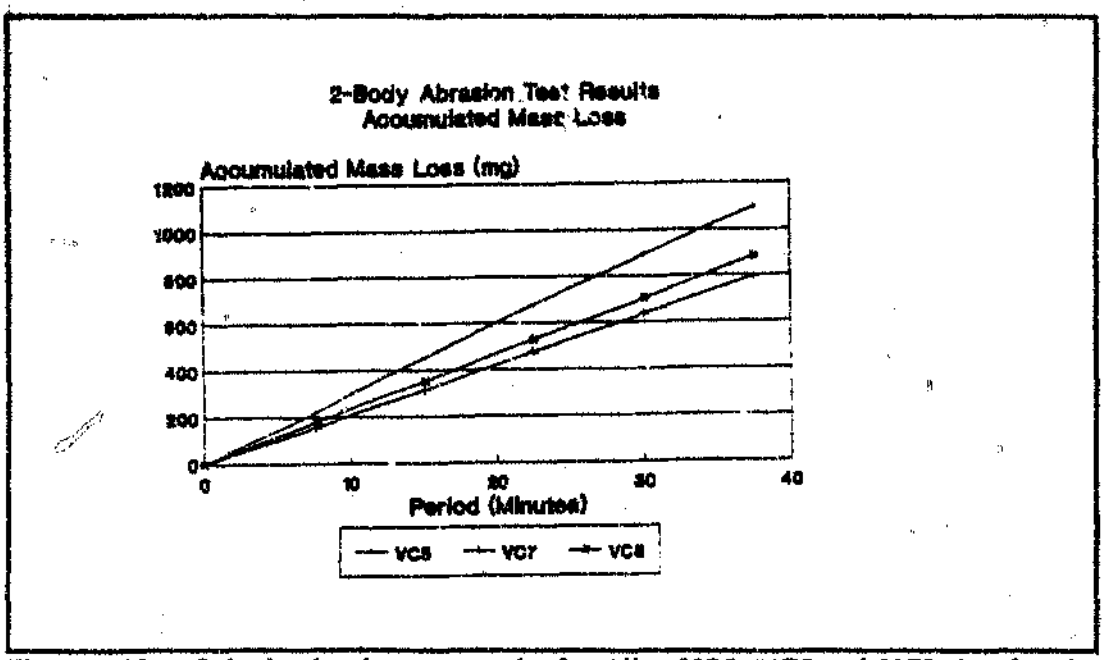

Figure 4.89. – 2–body abrasion test results for Alloy VC5, VC7 and VC8 showing the accumulated mass loss.

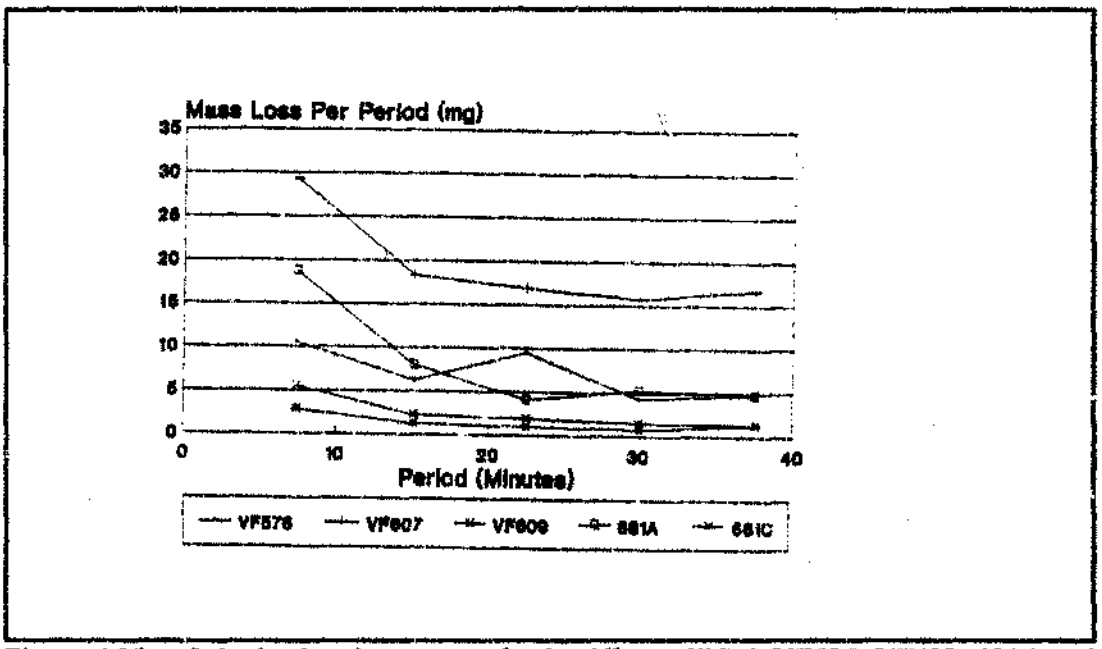

Figure 4.90. – 2–body abrasion test results for Alloys VF576, VF607, VF609, 681A and 681C showing the mass loss per period.

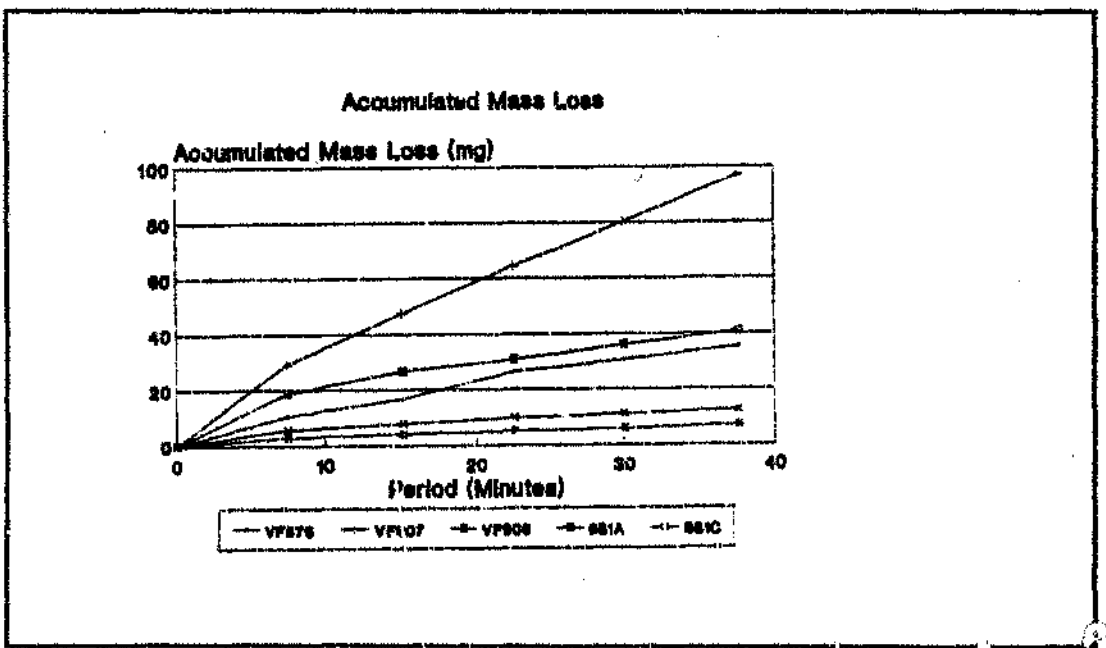

Figure 4.91. – 2–body abrasion test results for Alloys VF576, VF607, VF609, 681A and 681C showing the accumulated mass loss.

4.14. Comparative mass losses between 2 and 3–body tests

Table 4.17 shows the calculated volume and length losses from the modified 3–body and 2–body tests described in the previous sections. The measured hardness values with the standard deviations from 10 readings are also shown.

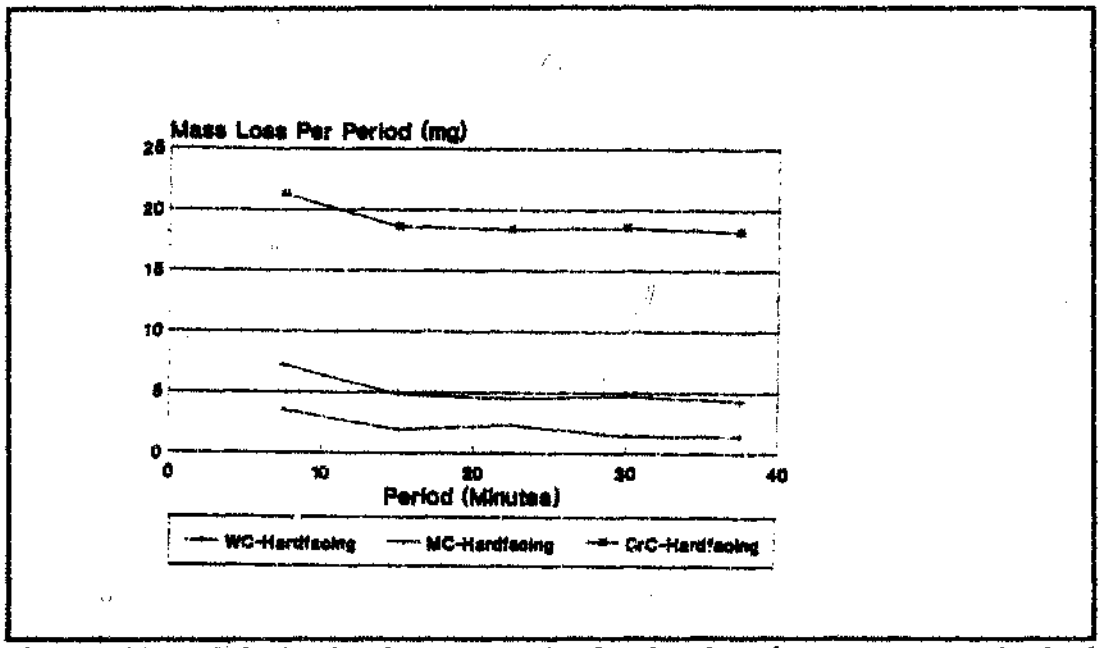

Figure 4.92. - 2-body abrasion test results for the chromium, tungsten and mixed carbide[32] hardfacing alloys showing the mass loss per period.

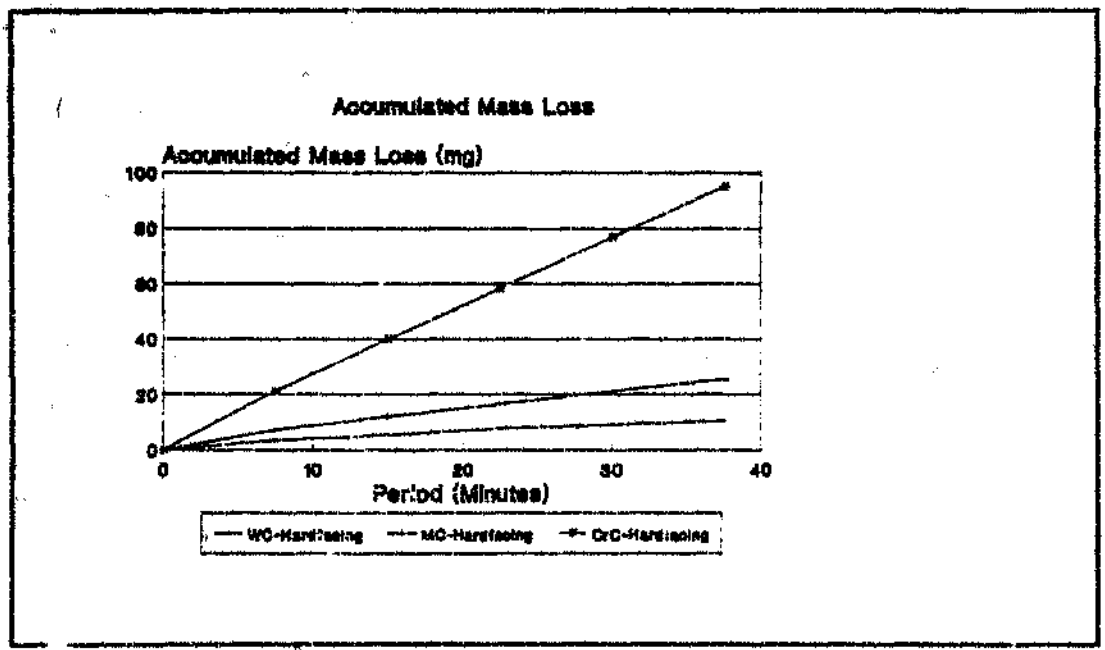

Figure 4.93. - 2-body abrasion test results for the chromium, tungsten and mixed carbide[32] hardfacing alloys showing the accumulated mass loss.

4.15. Microhardness results

101 and 81 indentations were made on Alloys VF609 and 681C respectively. The VC particle size (average of maximum and minimum dimension) was then plotted against the measured hardness. These results are shown in **Figures 4.100** and **4.101**. The results indicated that

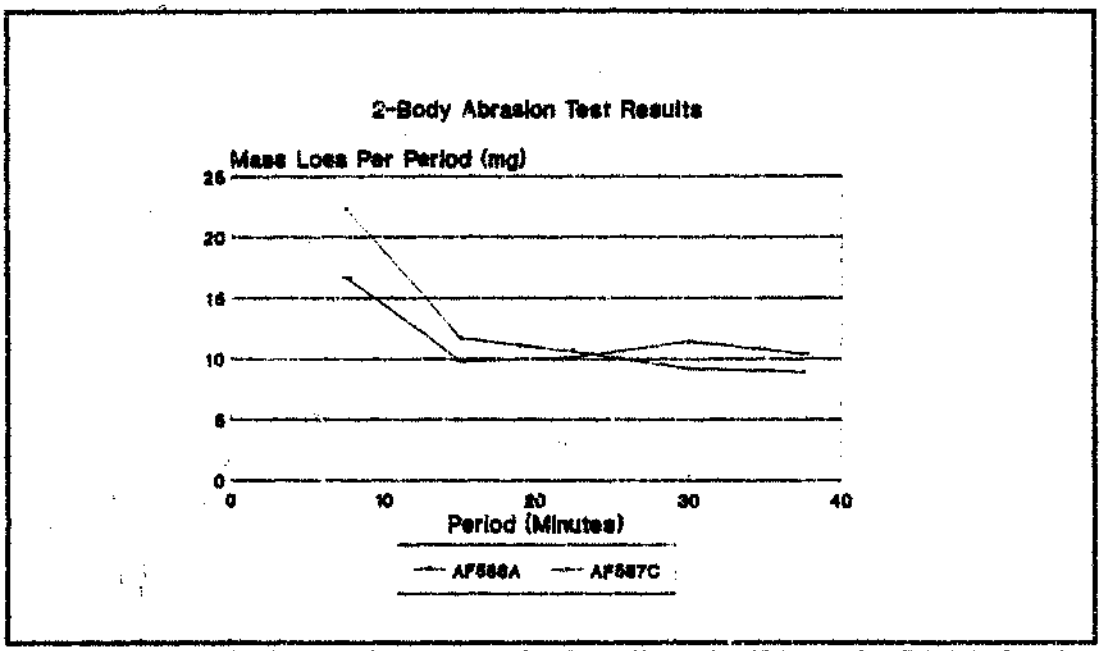

Figure 4.94. – 2-body abrasion test results for Alloys AF586A and AF587C showing the mass loss per period.

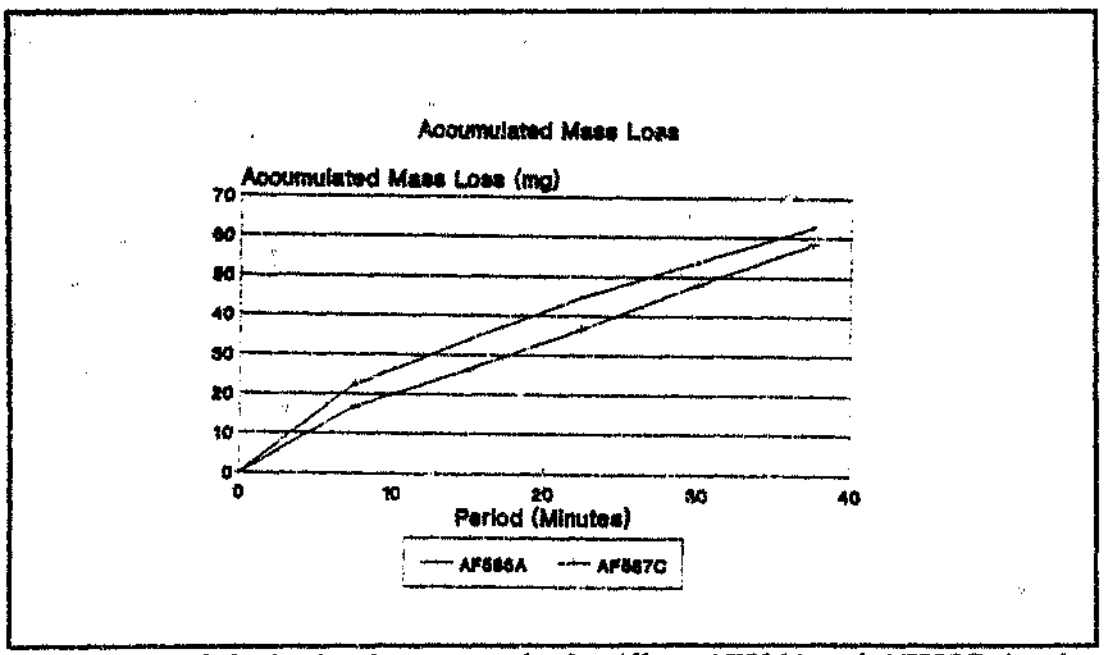

Figure 4.95. – 2-body abrasion test results for Alloys AF586A and AF587C showing the accumulated mass loss.

below about 12μm and 24μm respectively the apparent hardness of the VC particles drops in Alloys VF609 and 681C. The microhardness values measured on the matrices of these alloys are 515Hv (standard deviation 65.4Hv) and 316 Hv (standard deviation 18.9Hv) respectively.

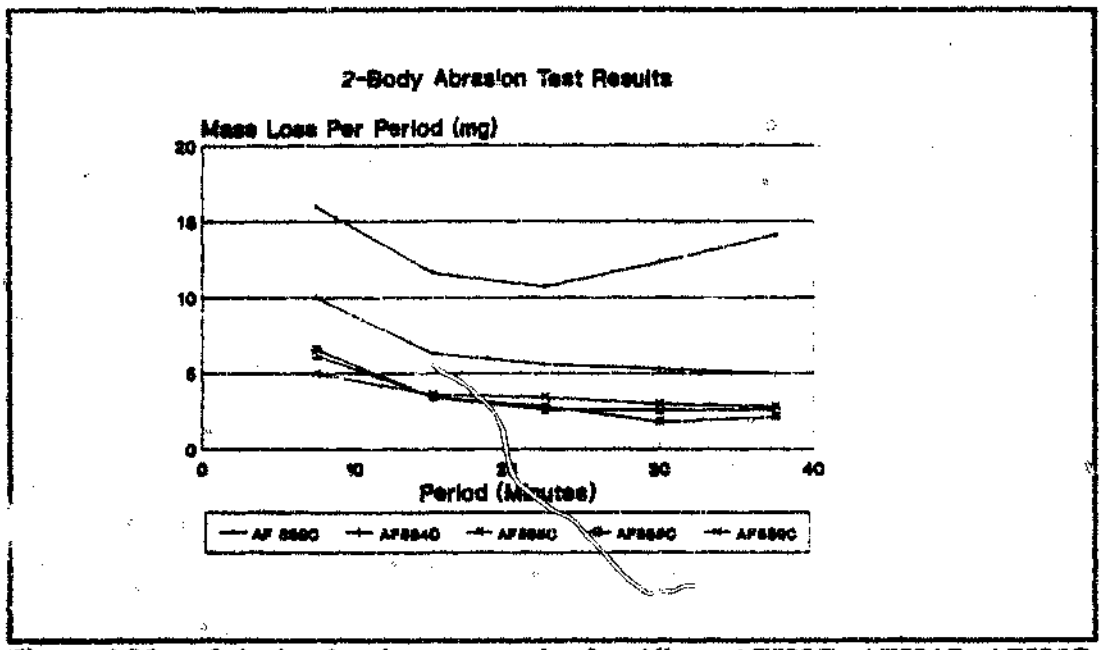

Figure 4.96. – 2–body abrasion test results for Alloys AF583C, AF584C, AF585C, AF588C and AF589C showing the mass loss per period.

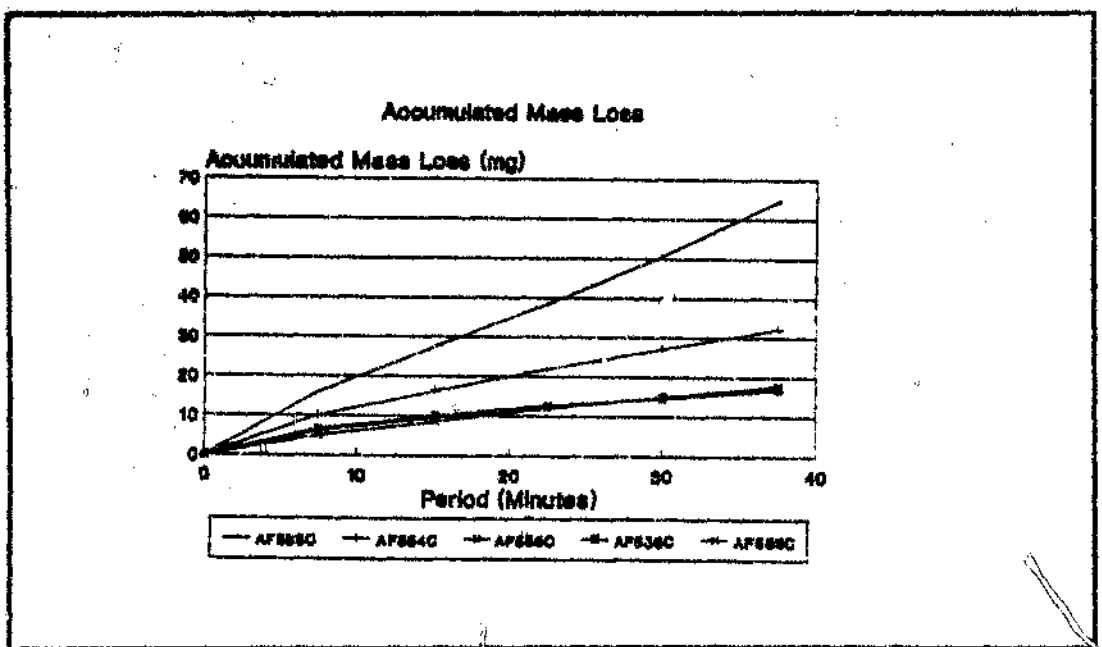

Figure 4.97. – 2–body abrasion test results for Alloys AF583C, AF584C, AF585C, AF588C and AF589C showing the accumulated mass loss.

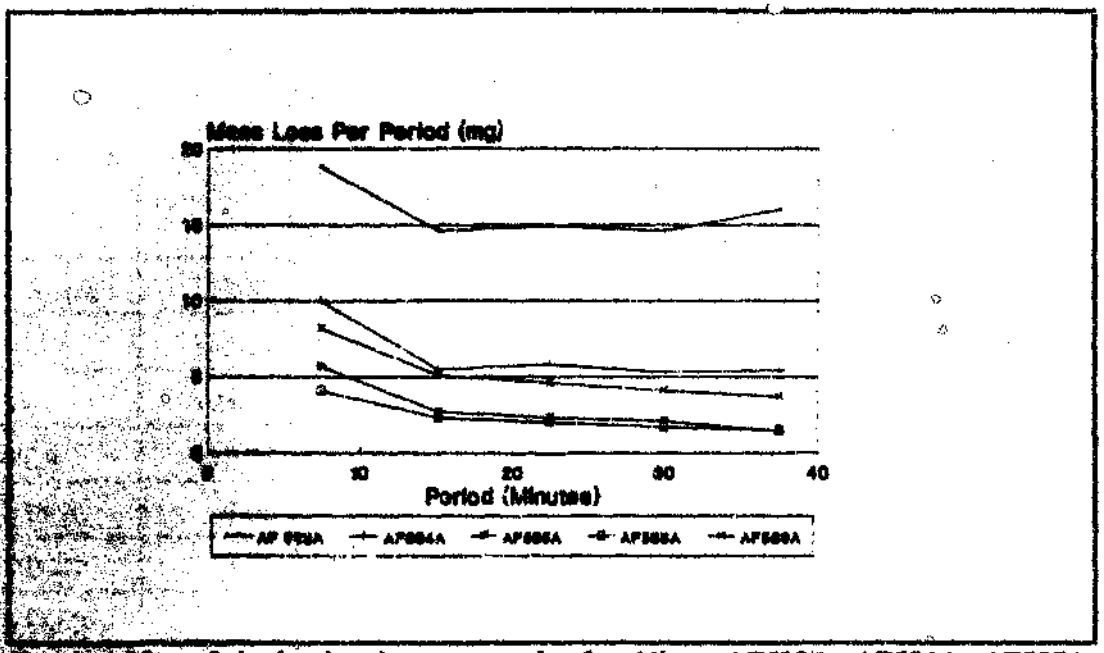

Figure 4.98. - 2-body abrasion test results for Alloys AF583A, AF584A, AF585A, AF588A and AF589A showing the mass loss per period.

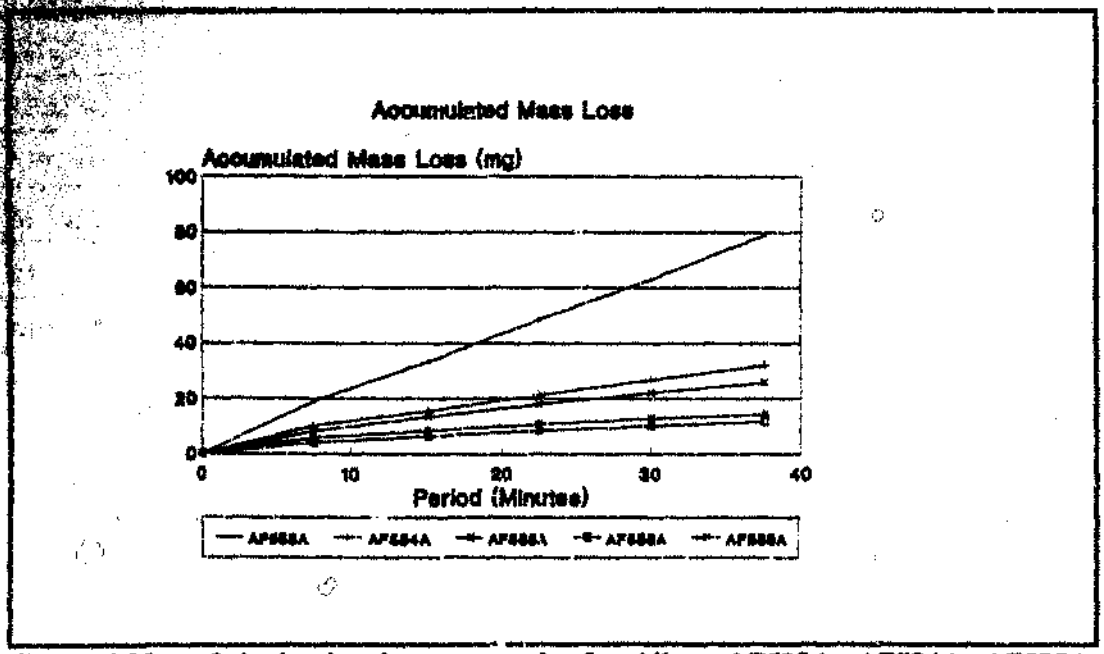

Figure 4.99. - 2-body abrasion test results for Alloys AF583A, AF584A, AF585A, AF588A and AF589A showing the accumulated mass loss.

Table 4.17. - Worn materials volume and length losses with the hardness measurements and the standard deviations of 10 readings.

Sample	2 Body Vol loss (mm^3)	2 Body Length loss (mm)	3 Body Vol loss (mm^3)	3 Body Length loss (mm)	Hardness HV_{30}	Standard deviation
MS avg(i)	112.47	1.432	57.49	0.732		
VC 5	145.14	1.848	37.72	0.480	400	12.9
VC7	103.97	1.324	17.87	0.228	164	4.2
VC8	116.35	1.481	20.72	0.264	261	19.0
VF576	5.02	0.064	47.08	0.599	726	8.7
VF607	13.92	0.177	10.50	0.134	280	7.9
VF608	2.42	0.031	18.39	0.234	516	113.6
VF609	1.16	0.015	1.37	0.017	830	125.9
681A	6.28	0.80	40.58	0.517	332	29.8
681C	1.90	0.024	6.61	0.084	332	29.3
AF583C	8.68	0.111	11.98	0.152	416	13.1
AF584C	4.52	0.058	15.82	0.201	514	34.2
AF585C	2.46	0.031	7.48	0.095	592	48.0
AF586A	9.56	0.122	14.68	0.187	893	33.9
AF587C	8.24	0.105	16.83	0.214	578	5.7
AF588C	2.46	0.031	8.01	0.102	696	19.4
AF589C	2.59	0.033	11.17	0.142	583	29.8
AF583A	10.59	0.135	12.64	0.161	531	19.1
AF584A	4.51	0.057	15.16	0.193	606	23.8
AF585A	2.07	0.026	16.30	0.208	714	21.4
AF588A	1.72	0.022	9.42	0.120	769	21.9
AF589A	3.67	0.047	12.25	0.156	689	29.1

(i) The average wear rate for mild steel.

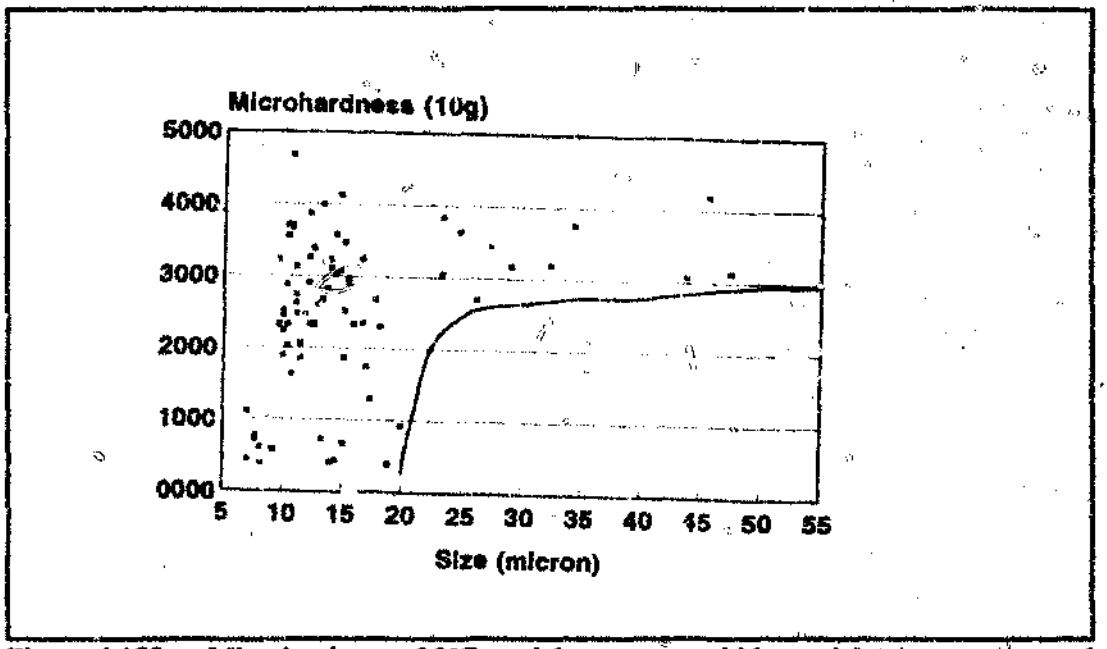

Figure 4.100. – Microhardness of VC particles versus carbide particle size as measured on Alloy VF609.

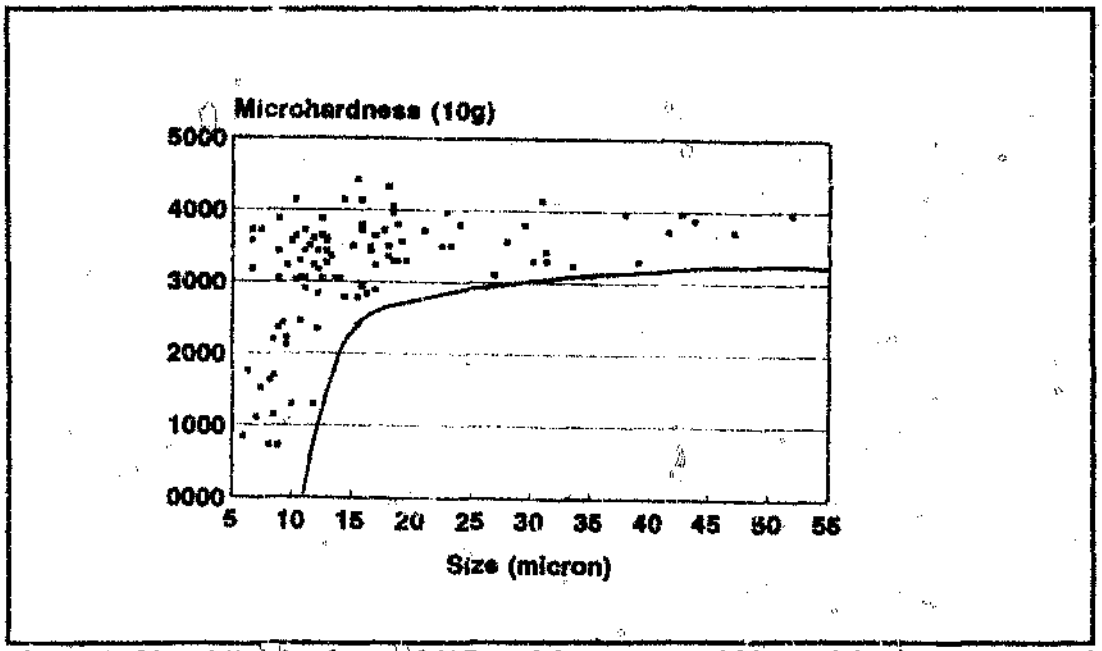

Figure 4.101. – Microhardness of VC particles versus carbide particle size as measured on Alloy 681C.

5. DISCUSSION

The experiments described in **Chapter 3** had two broad aims: to assess the properties of the materials produced (hardness, microhardness, wear and Jominy tests) and to determine the phases present in the materials by different techniques (XRD, metallography, Mössbauer spectroscopy, image analysis), to correlate properties and microstructure. In this chapter the results will be discussed and compared to decide which is the optimum group of alloys in the Fe–V–C alloy system for abrasion resistance.

5.1. Alloy manufacture

The melting difficulties experienced in the preparation of Phase 1 and 2 alloys, (see **Section 3.2** and **4.1**) resulted in heterogeneous alloys. Results obtained from these partially heterogeneous alloys were difficult to interpret. The small charges used to make these alloys resulted in fluctuations from the nominal charge (see **Table 4.1**). These fluctuations in chemistry were reduced by using larger charge masses to produce Phase 3 alloys.

Fluctuation in the chemical composition can be ascribed to several factors. In Phase 1 alloys the fine VC powder was easily lost during induction melting due to its being blown out of the crucible by expanding gases. The crucible linings were partially impregnated by the molten materials. This and the small scull remaining in the crucible from the previous melts contributed to the chemical fluctuations especially of the smaller charges used in Phase 1 and 2 alloys. This carry over from the previous melts was experienced despite careful cleaning of the crucibles before the melting of the next alloy. The largest increase in V content resulted from the incorrect supply of FeV material for Phase 2 alloys. Small losses occurred in all alloys due to the volatilisation of the charge material during melting. The contribution of volatilisation is however thought to be extremely small.

Two separate apparatus were used to obtain the chemical analyses. The C content was determined using a Leco machine while the remainder of the elements were measured using a spark discharge technique. Known calibration reference samples were impossible to obtain due to the extremely high C and V contents (ref Alloy VF609, **Table 4.1**). The total measured

chemistry of the alloys did not add up to 100% due to small measurement errors in these two techniques.

5.2. X-ray diffraction

X-ray diffraction confirmed the presence of all or some phases predicted by the Fe-V-C equilibrium phase diagram. The stoichiometry of the VC_{1-X} phase could not be found unambiguously. The measured lattice spacings matched neither $VC_{0.75}$ nor $VC_{0.88}$ exactly. The VC_{1-X} cubic structure can accommodate various amounts of C. A range of stoichiometries will change the lattice spacings only slightly.

The small changes in lattice spacing due to changes in stoichiometry are masked by other factors. One such factor is the thermal residual stress in the bulk material caused by the difference in coefficients of expansion of the different phases[36]. This stress may be almost as high as the yield point of the individual phases and therefore can influence the lattice spacings greatly. This stress is dependent on several factors including the morphology and volume percentage of the phases present. These factors are dealt with in greater detail in the literature[10,16]. The substitution of Fe by V in α also influences the lattice spacings. V atoms are ±6% larger than the Fe atoms and therefore result in a bigger lattice parameter[31].

Although the X-ray work was inconclusive in deciding the stoichiometry of the VC_{1-X} phase present, it did confirm the crystal structure of the phase present in the alloys. It also confirmed the presence of α and Fe_3C (cementite, orthorhombic crystal) phases. The presence of small quantities of other Fe_XC_Y carbides could not be excluded. These may be present in amounts below the detection limits of the present X-ray diffraction set up. Combining this information with the Mössbauer Spectroscopy and stoichiometric calculations made it possible to establish the phase compositions of the alloys.

5.3. Mössbauer Spectroscopy

The Fe–V–C alloy system pushed the potential of Mössbauer spectroscopy to its limits. The technique was used as a tool to examine the Fe containing phases in the alloy matrix and their composition. The technique gave results that are in good agreement with the stoichiometric calculations used to find the Fe_3C to α–FeV ratio and the Fe to V ratio in the α–FeV solid solution. These calculations showed that a carbide with a stoichiometry close to $VC_{0.76}$ formed. The technique was not successful in deciding the Fe to C ratio in the Fe_XC_Y phase, possibly because of incomplete Mössbauer spectroscopy data available in the literature, on the large variety of Fe_XC_Y that can form.

5.4. Stoichiometric calculations, X–ray diffraction, Mössbauer spectroscopy and density result

X–ray diffraction, Mössbauer spectroscopy and stoichiometric calculations individually were unable to fully describe all the phases in the alloys, but when combined they allowed the characterisation of the phases. By X–ray diffraction (see Section 4.4) it was not possible to decide unambiguously if VC_{1-X} corresponded to $VC_{0.88}$ or $VC_{0.76}$. With stoichiometric calculations (see Section 4.3) and Mössbauer spectroscopy (see Section 4.5) it was found that the carbide stoichiometry, $VC_{0.76}$, gave the best agreement between calculated and experimental results. The measured densities also agree more closely with the theoretical determinations based on $VC_{0.76}$ than $VC_{0.88}$. This further confirms that $VC_{0.76}$ is present.

The amount of V in the α phase determined by Mössbauer spectroscopy was in good agreement with the calculated values. The composition of the Fe_XC_Y phase could not be unambiguously extracted from the Mössbauer spectra but X–ray diffraction showed that the only Fe_XC_Y present in significant amounts was Fe_3C. Relative amounts of α and Fe_3C in the matrices of the alloys determined from the Mössbauer spectra agreed with the calculated values for most of the alloys.

5.5. Metallography

The precipitation of primary α in Phase 1 alloys resulted in only small eutectic and eutectoid VC_{1-x} particles forming. It was predicted that the small particles would contribute very little to abrasive wear resistance. The small particles are unable to prevent the penetration and movement of abrasive particles through the alloy surface. All Phase 2 and 3 alloys containing α, Fe_3C and VC_{1-x} precipitated primary VC particles.

Within Phase 1 alloys, Alloys VC2, VC5 and VC8 showed the difference in carbide size due to eutectic and eutectoid reactions (see **Figures 4.5** to **4.7**). The small carbides would only strengthen the matrix marginally. The eutectic VC was larger than the eutectoid VC but still far smaller than any primary VC particles. It was not effective in preventing the penetration and movement of abrasives through the surface of the alloy matrix.

X–ray diffraction revealed the presence of $VC_{0.76}$ but not V_2C in Alloys VC3, VC6 and VC7 (see **Figure 4.8** to **4.10**). V_2C may have formed in quantities below the detection limits of the X–ray diffraction system employed due probably to a peritectoid reaction. It is concluded that the kinetics of the peritectoid reaction are slow due to the stable VC_{1-x} phase. Accelerated cooling prevented the reaction from proceeding significantly leaving VC_{1-x} at room temperature as a metastable phase.

In Alloy VC4 (see **Figure 4.11**), VC_{1-x} was found in contrast with the predicted phases on the equilibrium phase diagram, by X–ray diffraction. This is again thought to be the unreacted VC_{1-x} left due to the slow kinetics of the peritectoid reaction when forming η. The morphology of the carbide particles was significantly different from the previous alloys suggesting the likely presence of the η phase. The amount of η formed was below the detection limits of the X–ray diffraction.

Alloys VF576 and AF584C (see **Figures 4.12** and **4.16**) lay close to the boundary of Fe_3C phase region on the 1100°C isotherm of the Fe–V–C equilibrium phase diagram. Both microstructures show Fe_3C in a morphology which is not consistent with the eutectoid reaction. It is therefore assumed that the lines of the isotherm are shifted by the higher than

equilibrium cooling rate. This type of shift was observed in Alloys AF589A and AF589C described later. The small amount of Fe_3C that formed contributed negatively to the abrasive wear resistance as seen later. The brittle nature of the Fe_3C phase and the morphology in which this phase formed was thought to be the cause of the deterioration in abrasion resistance. Alloy AF584C showed grain boundary cracks in the Fe_3C phase.

Alloys AF589A and AF589C (see **Figure 4.22** and **4.23**) behaved as if they had greater C contents due to the high cooling rates which shifted the phase equilibria into the graphite region. The resultant graphite was present in large rectangular needles and sometimes rings as seen in Alloy AF589A. Graphite due to its low hardness contributed adversely to abrasion wear resistance as shown later.

The primary VC_{1-x} phase alloys which contain the eutectic VC_{1-x} and α show the tendency for precipitation of the eutectic VC_{1-x} on the primary phase leaving a surrounding ferrite region free from small VC_{1-x} particles. An example is shown in Alloy VF607 seen in **Figure 4.24**. This resulted in the primary VC particles experiencing slight growth during the eutectic reaction.

The Alloys VF577, VF578, VF579 and AF586A (see **Figure 4.28** to **4.31**) which contained σ and η, showed poor potential as abrasive resistant materials due to the friable nature of these phases. The preparation of metallography specimens was highly problematic due to spalling of samples containing these phases during handling and polishing. The polished surface of the alloys revealed a network of cracks and craters where the friable phases had spalled. Alloys containing both η and σ phases were therefore deemed to be bad for abrasive application although their bulk hardness values were high.

It is concluded from the metallography that alloys in the regions containing either primary VC_{1-x} with eutectic VC_{1-x} and α or primary VC_{1-x} with eutectic VC_{1-x}, Fe_3C and α show the greatest promise for abrasion resistant applications. The phase predictions using the 500^oC and 1100^oC isotherms of the Fe–V–C in this region should be interpreted carefully. Approaching the boundary line of graphite or Fe_3C while in the γ region of the 1100^oC isotherm allows the formation of both these phases. Both should be avoided if possible. VC_{1-x}

particles resulting from eutectic and eutectoid reaction are too small to affect abrasion resistance. Those alloys containing η and σ are too brittle to be of any significant use in abrasion applications as they tended to crack or spall under stress.

5.6. Image analysis

The image analysis showed variation in the microstructures from one area to another. Some measure of this variation is given by the standard deviations of the measured volume percentages of VC.

The as cast alloys (slower cooled) had larger VC particles than the arc melted (faster cooled) alloys of the same compositions. This agrees with other researchers[6.25]. The one exception, namely Alloy AF585C, was most likely caused by the lower VC content (see **Table 4.1**). This agrees with other researchers[6.25].

A linear intercept method was used to simulate the manner in which the abrasive particles "see" the alloys. The purpose was to relate the abrasion resistance to the apparent VC particle size. Abrasives would normally move across the surface along almost straight lines. The technique was however not successful in measuring the dendritic arm length in Alloy VF576 (see **Table 4.10**). This technique does not allow a true reflection of the size of the dendrite arms. A measure of the length of dendrites is important as these may crack under loading and cause accelerated abrasive mass loss (see **Section 5.8**).

5.7. TEM

The TEM results showed the presence of a very fine precipitate in Alloy VF576. The effect of such fine precipitates would be to slightly increase the mechanical properties of the matrix phase. The presence of these fine precipitates confirms the conclusions made during the Mössbauer spectroscopy work discussed earlier in **Section 4.4**.

TEM results showed that the $VC_{0.76}$ particles had a lattice parameter of 0.416nm corresponding to $VC_{0.76}$ (see **Figure 4.55**). It confirms the stoichiometry of the VC_{1-X} phase

found by X-ray diffraction (see Section 4.3), Stoichiometric calculations (see Section 4.2) and Mössbauer spectroscopy (see Section 4.4).

Unfortunately other alloy samples were not examined by TEM as the cost and preparation time required were prohibitive.

5.8. SEM analysis of metallography and worn samples

The depth of view available with this technique made examination of the worn samples much easier than by optical means. Back scattered imaging allowed phases to be recognised on a worn surface. The position and effect of these could therefore be determined. Spot analyses confirmed the identification of the phases.

The phases could be identified as high in Fe or V and the ratio of these could be determined. The SEM used, did not have a windowless detector making it impossible to detect low atomic number elements such as N, O and C. Within this limitation it was possible to determine that the dendritic particles in the Phase 2 and 3 alloys consisted of V with an Fe content below 1.5% (see Figure 4.35). This is in accordance with the findings of Dmitrieva et al[29]. Combining this with the high microhardness values measured confirmed them as VC particles. The high resolution allowed the fine globular eutectic phase lying in the cementite (see Alloys VF576, AF588A and AF588C in Figures 4.12, 21 and 22) to be identified as a eutectoid, pearlite.

Additional work done on the interpretation of the abrasion test results are described in Sections 5.12 and 5.13.

5.9. Microhardness test results

From **Figure 4.100** and **4.101** one can conclude that the intrinsic hardness of the $VC_{0.76}$ phase is about 3500Hv ±500Hv using a 10g load. This hardness varies from that given in literature. Reasons for this include carbide orientation effects[28], stoichiometry changes and the low microhardness test load used. A small error in the measured size of the indentation resulted from using a 10g load. The low load and high $VC_{0.76}$ hardness resulted in small indentations that influenced the accuracy of measurement using the standard attached microscope.

When the $VC_{0.76}$ particles are small, (below about 12μm and 24μm for Alloys VF609 and 681C respectively) the apparent hardness drops. The VC particles are either pushed into the matrix or break apart under the high point loads.

The VC_{1-X} particle size at which the apparent hardness drops, appears to be dependent on the matrix hardness. This conclusion is drawn from the microhardness measurements made on the matrix. These show that Alloy VF609 had a higher matrix hardness ($515Hv_{0.010}$) and experiences the drop at 12μm as opposed to 681C ($316Hv_{0.010}$) which experiences the same drop at 24μm. The reason for the drop appears to be less support of the smaller carbide particles by a softer matrix. This effect is consistent with the wear results reported by the Japanese[22,23]. The abrasion resistance of the alloys which had undergone heat treatment to increase the matrix mechanical properties showed better abrasion resistance for the same volume % of VC.

Another possible reason for alloy VF609 being able to allow smaller size VC_{1-X} particles than 681C without losing hardness, is contiguity. The volume percentage of VC_{1-X} phases in VF609 is slightly higher than in 681C (71.9±12.5 vol% and 60.9±5.6 vol% respectively). This increase in volume fraction implies closer contact between the $VC_{0.76}$ particles and therefore results in greater support of these.

Some small VC particles in **Figure 4.100** and **4.101** resulted in hardness values that are of the same order of magnitude as the larger VC particles. This apparent anomaly was thought to be caused by sizing a VC particle from the area seen in a 2–dimensional image and not

the actual 3-dimensional particle. The particle seen may only be a small tip of a much larger VC particle lying below the surface. Thus, the hardness measurement may erroneously be attributed to a small VC particle.

5.10. Macrohardness measurements

The standard deviation in the macrohardness measurements made on Phase 2 alloys suggested that these alloys were generally heterogeneous. The hardness values of the alloys in Phase 3 showed lower standard deviations and suggested greater homogeneity. Arc melted alloys had higher hardness values than the as cast alloys. This was consistent with the faster cooling rate experienced by these alloys (see **Section 3.2**). The change in microstructure was not immediately apparent. The faster rate of cooling may have resulted in some super cooling and therefore greater nucleation. This caused more VC particles of smaller size to form, which was confirmed by the image analysis done (see **Table 4.10**).

Certain apparent correlations between the hardness and wear rates of the alloys could be found. These were negated by exceptions such as Alloys AF584C and VF576. These exceptions suggest that reliable ranking of multiphase alloys for abrasion wear resistance applications based on macrohardness results is very difficult.

5.11. Jominy tests

From the microhardness work it was seen that the matrix played an important role in the support of the VC particles. Quenched and tempered martensite has both high strength and toughness. The Jominy tests were performed to see how hardenable these materials were and whether martensite could be formed. Alloy AF587C was manufactured to examine the hardenability of an alloy that had a purely γ matrix at elevated temperatures.

Two factors contributed to the variable results (**Figure 4.57**) obtained. The samples were tested in the as cast condition. This was done as the cost of centreless grinding was considered prohibitive. Secondly, the samples were heated in an unprotected atmosphere which caused some scale to form on the outside surface of the sample. This scale varied in

thickness and changed the rate of heat loss. The experiments did prove that these alloys are only partially hardenable to a depth of ±5mm without further alloy additions under very severe quenching conditions.

Often hardfacing is reapplied to on-site components. These venues may not have heat treatment facilities. The validity of developing a heat treatable alloy for such applications was therefore questioned. Examples of such applications occur in open cast and deep level mining. Further work would most likely include alloy additions to increase the hardenability of the alloy matrices.

5.12. Abrasion test apparatus

Problems with abrasion testing were highlighted during the first series of tests conducted. For meaningful ranking of alloys to take place, two areas in the test matrix must be carefully examined. The first is dependent on the experimental set up to introduce as few variations and errors as possible. The second requires alloys that are homogeneous so that at every stage of testing the same microstructure is being exposed to the abrasive conditions.

Fluctuation in abrasion resistance results seen in the 3-body abrasion tests before the modification of the test rig (see **Section 3.13.1**) reveal the sensitivity of abrasive wear testing. Small amounts of material are removed during abrasive wear testing. Small problems introduced by a poor experimental set up are therefore magnified. An example was alloy VF608 in which both a heterogeneous material and poor test set up caused mass losses that varied randomly by two orders of magnitude from 12.7 to 0.1mg per period.

The SEM was used to find that one fault of the existing 3-body wear rig resulted in the random changing of the direction of wear (see **Figure 4.42**). It was seen later that a specimen undergoes an initial high wear rate while the sample "beds in" (see **Table 4.14**). After that the drop in the wear rate tails off to a slower rate. By changing the direction of wear randomly, the sample is unable to reach this stable condition and fluctuations in the wear rate result (see **Table 4.12**). The drop off also occurs due to breakdown of the abrasive particles during testing. These were only replaced at the beginning of every new set of samples.

A second problem was the fluctuation in angle between the surface of the sample and the drum. Varying this angle resulted in a mixture of wear mechanisms due to different loads experienced by different areas and therefore fluctuating wear rates.

The modified 3-body and 2-body abrasion test equipment was designed to reduce the experimental variations. These modifications are described in detail in **Section 3.13.1**. The 3-body, dry abrasion test described in the ASTM G65 - 84 standard, shows two ways of assessing the experimental and measurement errors. These techniques gave results of 56.1% and 25.6% respectively for the 3-body abrasion test rig. After modification of the abrasion apparatus these errors were reduced to 27.8% and 7.8% respectively. The improvements made ranking the alloys more dependable. After modification the steel calibration samples showed only a downward trend and no fluctuation as previously (see **Table 4.15**).

5.13. Abrasive wear properties of the alloys

The experimental error of 28%, although an improvement, still makes ranking the alloys, difficult. Wear mechanisms add a further complicating factor to the problem of ranking alloys. These factors combine to make it difficult to make deductions from the experimental results obtained.

No definite deductions could be made about the relative merit of varying amounts of VC in Alloys AF583A, AF583C, AF584A, AF584C, AF585A and AF585C. The wear results obtained lie within the known error band. Comparing Alloys VF607 and VF609 which have vastly different VC contents however shows a reduction in volume loss of over one order of magnitude in favour of higher VC content (Alloy VF609). The courser VC particles and the higher VC volume percentage allow VF609 to resist the effects of abrasive particles. These results are consistent with the results obtained from microhardness measurements, SEM work and literature[6].

The effect of the VC particle size on the 3-body abrasive wear resistance is seen in the series of micrographs (see **Figures 4.45 to 4.48**). Mild steel samples showed clean long wear grooves that ran down the length of the sample. The introduction of small eutectic and

eutectoid VC particles did not significantly affect the passage of abrasive particles. They were too small to stop the abrasive penetration into the matrix and did not significantly affect the wear resistance (see **Table 4.14**). A comparison can be drawn between the microhardness tests in which the small VC particles showed an apparent low hardness by being pushed into the matrix.

The smaller primary VC particles are just big enough not to be pushed into the matrix, but due to the poor support given by the matrix breakup and spall. An area of 681C shows the interrupted abrasive wear pattern from these VC particles and the resultant damage to the medium sized VC particles. Microhardness tests (see **Section 5.9**) showed that VC particles below a certain size, breakup under a given load, and thereby loose their "apparent" hardness. The effectiveness of such particles on abrasive wear resistance is therefore low.

Large VC particles show the greatest wear resistance. VC particles were seen to stand proud from the wear surface as the surrounding matrix material was removed (see **Figure 4.52**). The effect on abrasive wear is great. Abrasive particles tended to move over the surface of the VC particles. Therefore the material withstands the attacks by the abrasive particles until the large VC particles deteriorate or are removed due to lack of support from the surrounding matrix. The VC deterioration occurs by micro spalling around the edges where the abrasive particles first make contact (see **Figure 4.51**). The micro spalling has the appearance of a series of micro indentations not unlike those of small microhardness indentations.

VF576 showed wear rates during 3–body abrasion testing of almost three times that of other alloys with comparable alloy chemistry. The significant differences between VF576 and the other alloys are the extended VC dendrites present in alloy VF576. SEM analyses showed that small cracks occurred in VC dendrites surrounding hardness indentations. These cracks were thought to be the reason for the poor performance of the long dendritic VC particles. The stress placed on the VC particles by the abrasive particle caused them to fracture along their length (see **Figure 4.40**) in the same way as occurred during hardness tests. The broken pieces of dendrite were then easily removed by other abrasive particles as they moved across the alloy surface. This is seen in **Figure 4.41** which shows preferential removal of material associated with the dendritic VC particle. Based on the high wear rate of VF576 and the

evidence seen in **Figure 4.41**, it was concluded that extended VC dendrites should be avoided in abrasive wear applications.

A large discrepancy in the wear rate of Alloy AF584C from the remaining pearlite matrix (Alloys AF583C and AF585C) alloys was noted. Alloy AF584C varied from the other alloys by having acicular Fe_3C on the grain boundaries. This often had cracks running through it. It was also seen that cracks in the material, formed during the manufacture of the alloys and the test specimens, acted as sites for abrasive particles to penetrate the surface of the alloys (see **Figure 4.43**). Phase one in the two phase model of abrasive wear[12] is the penetration of the abrasive particle into the alloy surface. Cracks already present in the alloy accelerated the first phase and therefore accelerate abrasive wear.

The SEM analyses of the worn surfaces showed that the presence of cracks in an alloy before abrasion resulted in preferential removal of these areas during 3–body abrasion (**Figure 4.43**). Cracks in alloys should therefore be avoided. Acicular cementite was often cracked and graphite needles seen in Alloys AF589C and AF589A should be avoided. It should be possible to avoid acicular Fe_3C by controlling the chemical compositions of an alloy so that it does not approach the Fe_3C boundary line on the 1100°C isotherm of the Fe–V–C equilibrium phase diagram too closely. It should be possible to avoid free graphite by similarly remaining away from the graphite boundary line on the 500°C isotherm of the Fe–V–C equilibrium phase diagram.

The abrasive wear resistance of alloys with small eutectic and eutectoid VC particles (Alloys VC5, VC7 and VC8) was worse than alloys with similar V contents (Alloys AF583A and AF583C) and larger primary VC particles. A higher C and V content shifts the alloy into the phase regions where primary VC forms. These larger primary VC particles can affect the passage of the abrasives through the alloy. They stop the penetration of the abrasive particles into the alloy. The larger VC particles allow the abrasives to move over them without major damage (see **Figure 4.48**).

2–body abrasion results are different. In 2–body abrasion the load is spread over the total number of abrasive particles present. The individual abrasive particles are not independent

loaded as in 3–body conditions and therefore are not able to exert enough force to penetrate the material. The existence of cracks, small VC particles and other factors that are critical in 3–body abrasion resistance affect the life of alloys under these test conditions, little. Under these abrasion conditions the total volume of hardphase in any form and size with the total hardness are the most important properties.

It must be emphasized that the conclusions drawn in this work apply to the test conditions which have been used. Changes in wear mechanism due to abrasive size, environment and load may well require different microstructures for optimum results

5.14 Comparison with commercially available hardfacing alloys

The commercial hardfacing alloys tested are used successfully in industry and would be the most likely competitors for any newly developed alloy. The alloys increased in abrasion resistance from those based on a chromium carbide to a mixed carbide to a tungsten carbide hardphase, under 2–body abrasion conditions. This was expected as literature quotes tungsten carbide as one of the best materials for applications involving abrasion. An anomaly was discovered when the WC hardfacing showed greater mass loss that the mixed carbide hardfacing under 3–body abrasion conditions. This anomaly is ascribed to the higher density WC settling out in the weld pool, resulting in a region near the surface of the weld being depleted in WC. This is a major reason for the development of the (W,V)C based alloys, Ucar[25] and Vancar[4]. These carbides have densities much closer to that of molten Fe resulting in more homogeneous carbide distribution. The sample used in the 2–body abrasion tests was ground deeper, exposing a region with a higher WC content.

VC has a density much closer to Fe than WC and would therefore not present these problems[6,25]. The wear rate of alloys containing VC is constant throughout the thickness of the deposit. VF609 is an example of this. Section 5.13 has shown that a soft ferritic matrix may not be the best for wear resistant applications. Yet, VF609 with its ferritic matrix obtained the same and better wear rates as tungsten carbide–based materials with a martensitic matrix. The VC content of VF609 is only slightly higher than the commercial alloys used. By optimising the matrix it should be possible to reduce the carbide content to that of commercial

alloys and still maintain superior abrasive resistan! roperties.

6. CONCLUSIONS

1. The abrasion resistance of selected alloys in the Fe–V–C system was equal or better to that of commercial hardfacing alloys (WC, Cr_2C_3 and mixed carbide) under these experimental conditions.

2. The 500°C isotherm of the Fe–V–C phase diagram may be used as a guide for predicting the phases formed when producing alloys using the vacuum tungsten arc and induction melting techniques described in this dissertation.

3. Those materials containing primary spheroidal VC_{1-X}, α and Fe_3C were the most suited for abrasive applications. In these alloys carbon will form $VC_{0.76}$ preferentially. Any excess carbon will form Fe_3C while any excess vanadium will form α solid solution with iron.

4. Microhardness tests indicated that dendritic VC_{1-X} particles are very brittle and increase the wear rate. This was proved by SEM work which showed that areas containing dendritic VC particles showed accelerated material loss. This was thought to be the cause of the high wear rate in Alloy VF576. Dendrites should therefore be avoided for abrasion resistant applications.

5. The presence of cracks prior to abrasion resulted in preferential removal of cracked areas during 3–body abrasion. Cracking therefore leads to higher abrasion rates and should be suppressed.

6. Graphite is relatively soft and acted as penetration sites for abrasives. Stage one of the abrasion cycle was therefore accelerated. Graphite should therefore be particularly avoided in 3–body abrasion situations.

7. Alloys with small VC particles showed lower overall abrasion resistance than alloys with similar vanadium contents and larger VC particles under 3–body abrasion conditions. Larger VC particles were able to withstand the attack of the abrasive

particles and remain proud of the worn matrix.

8. Alloys containing η and σ phases were so friable that they could not be tested except for alloy AF586A. They may be expected to perform poorly under abrasive conditions on account of their brittleness but this should be investigated further.

9. In 2–body abrasion tests, cracks and small VC particles which critically affect the abrasion resistance under 3–body conditions are of lesser importance. The total volume percentage of VC and overall hardness are more important.

10. The use of VC as a hard phase in abrasion resistant applications gives a higher abrasion resistance than WC of the same mass because of its much lower density, higher hardness and greater uniformity of carbide distribution in the hardfacing alloy. Control data on the importance of the VC particle size, shape and volume percentage have been collected in this work.

11. Future work on these materials should involve the use of the alloys as weld deposits on test plates. An attempt should be made to increase the hardenability of the matrix while ensuring large, spheroidal VC particles and avoiding cracking.

Bibliography

1. Mineral commodity summary, US Dept. of the Interior, Bureau of Mines **(1991)** p177–178.
2. **Russell B.G**, Journal of the S A Inst. of Mining and Metallurgy, (86)7, **(1986)**, pp225–234.
3. **Brown H.J**, USA patent 4,155,789, 22 May 1979.
4. Vancar brochure, Stoody Company, USA, 1983.
5. **Brown H.J**, USA patent 4,443,255, 17 April 1984.
6. **Brown H.J**, USA patent 4,446,196, 1 May 1984.
7. **Ishihara J. and Nagai M**, Tetsu to Hagane, vol64 **(1978)** 12, 106, (In Japanese).
8. **Ishihara J. and M.Nagai M**, Tetsu to Hagane, vol65 **(1979)** 2, 86, (In Japanese).
9. **Raghavan V**, Phase diagrams of ternary iron alloys, **(1987)**, pp114–124.
10. **Eyre T.S**, Powder Metallurgy, 24, (2), 1981, 57
11. **Ko P.L**, Tribology International, 20 no 2. 1987, 66
12. **Czichos H.** Tribology – a systems approach to the science and technology of friction, lubrication and wear, Elsevier, Amsterdam, 1978
13. **Eyre T.S**, Tribology International, Oct, 1976, 203
14. **Larsen–Basse J. and Tanouye P.A**, Int. Conf. on Hard Tool Tech., 1976, Hawaii, Abr. of WC–Co Alloys by Loose hard Abrasives.
15. **Bhushan B, Davis R.E. and Kolar H.R**, Thin solid films, 123, 1985, 113
16. **Avner S.H**, Introduction to physical metallurgy, McGraw–Hill book company, New York, 1986
17. **Jian–min T, Ye–ying S, Hua–yi Z, Ching–an Z and Xian–wu K**, Tribology international, 18, 2, April, 1985, 101
18. **Bereza J. M**, Inst. Brit. Foundrymen, 78th Conf, June 1981, Edinburgh, 20
19. **Drzeniek H, Kowalski M. and Lugscheider E**, Surfacing Journal,16 (4), 1985, 121
20. **Drzeniek H. and Lugscheider E**, Int. Therm. Spray. Conf., Sep 1986, Montreal, 651
21. **Berns H. and Fischer A**, Proc. Inst. Mech. Eng. Conf, Tribology– Fric. Lub and Wear : Fifty years on, vol II 1987, 603
22. **Friend C.M**, Material Science and Technology, 5, 1989, 1
23. **Wertheim G.K. et al**, Physics Review, 12 **(1964)**, p173.
24. **Matteazzi P. et al**, Hyperfine Interactions, 68 **(1991)** p173.

25. "Ucar" vanadium–tungsten carbide product brochure, Union Carbide corporation, New York.
26. **Dmitrieva G.M, Shurin A.K. and Vasil'ev A.D,** Met. Sc. & Heat Treatment,vol 20,(3–4), Mar–Apr, (1978), pp325.
27. **Petrov G.L, et al.** Welding protection. April 1977, 24(4) pp11–14.
28. **Rowcliffe D.J. and Hollox G.E,** Journal of Material Science, 6, (1971) pp1270–1276.
29. **Kesri R. and Durand–Charre M,** Mat Sci and Tech, Vol4, August (1988), pp1–8.
30. **Chang W.C, Tsun H.H. and Qian M,** Materials Science and Technology, vol6, Sep 1990, 905
31. Physical and chemical standards handbook
32. WASA product data sheet No. WA120, Welding Alloys of South Africa, May 1986.
33. **Finches I. and Sample L.A,** Journal of Physics, F3 (1973), p647.
34. **Stearns M.B,** Physics Review, 147 (1966), p439.
35. **Cullity B.D.** Elements of X–ray diffraction, Addison–Wesley, second edition 1978.
36. **Rigney A. and Glaeser W.A.,** Editors, Source book on wear control technology, American Society of Metals, pp305–311.
37. **Saltzman C.A,** Metal progress, Feb (1986), pp25–30.
38. **Sutton A.L. and Hume Rothery W,** SER 7, vol46, no 383, Dec 1955, pp1295–1308.
39. **Slabodinskii I.N. et al,** British Industrial and Scientific Translation Service 19593, December 1980.